Computational Study of the Effects of Surface Contamination on the Gas Transfer Across the Air-Water Interface

By

YASEMIN AKAR

A Thesis Submitted in Partial Fulfilment of the

Requirements for the Degree of

Doctor of Philosophy

Department of Mechanical and Aerospace Engineering

College of Engineering, Design and Physical Sciences

Brunel University London

March 2019

I have devoted my thesis to my late father Ünal Akar, who I dearly miss. I would like to express my sincere gratitude for all that he has done for me

ACKNOWLEDGMENTS

I would like to express my sincere gratitude to my supervisor, Dr Jan G. Wissink who not only facilitated my entry in the area of computational fluid dynamics but also directed me into solving complex research problems with his great talent and experience. His support made the discovering process during my Ph.D. program valuable. My growth as an engineer has greatly benefitted from his knowledge. I could not have hoped for a better advisor and mentor. I also wish to give very special thanks to my co-advisor, Dr Tze Pei Chong. Special thanks go to Dr Herlina from the Karlsruhe Institute of Technology for her great support. Her connections to the Steinbuch Centre for Computing (SCC) in Karlsruhe were very valuable to obtain computing time on the HP XC 3000 cluster, which provided an excellent platform to perform the larger computational simulations presented in this thesis.

I would like to offer special thanks to the support teams in Brunel University who have assisted me throughout the Ph.D. programme. I also like to thank my fellow colleagues Hossein, Raad, Jaa, Thammarat, Masayuki, Futra and Fahimeh & Mansour at Brunel University for their companionship and support during this research.

Also, I would like to thank my Turkish friends Ezgi and Ayşe at Brunel University for their support and friendship. Also special thanks to my friend Kureyş who has supported me throughout my Ph.D.

I would like to give my gratitude to my loving parents, Ünal and Nigâr Akar as well as my brothers Serdar and Murat Akar. It is their encouragement and support from the very beginning of my life that made it possible to reach this stage. To my

wonderful brother Serdar Akar: Thank you for always believing in me and for being by my side, you are very special to me and I could not have done this without you.

Preface

My main scientific contributions in this work comprise:

- The development of a model that predicts the effect of surface contamination by immiscible surfactants on interfacial gas transfer based on the clean surface fraction and characteristics of the turbulence in the water phase. To achieve this I worked in close cooperation with my supervisor and Dr Herlina from KIT in Karlsruhe.

- Another major result was the recognition that the surface divergence model breaks down in the presence of significant contamination because surfactants force the surface divergence to become virtually zero.

- The investigations into the effect of slip length on interfacial gas transfer resulted in a model that allows the pollution level to be expressed by a limited slip length. This work was mainly carried out by myself with guidance from my supervisor.

- The study of the applicability of the WENO-Z scheme for the convection of the 2D surfactant. This work (comparing the correctness of the implementation of the WENO-Z scheme and comparing its accuracy with that of the classical WENO scheme), I also carried out with a high degree of independency and some guidance from my supervisor.

TABLE OF CONTENTS

Page

Page

LIST OF TABLES

LIST OF FIGURES

Figure Page

SYMBOLS

Name	Description	SI unit
a	Addition of convective and diffusive terms	(m/s^2)
c	Instantaneous gas concentration	(kg/m^3)
c'	Turbulent concentration fluctuation	(kg/m^3)
c_b	Dissolved gas concentration in bulk region	(kg/m^3)
c_s	Gas concentration at the surface	(kg/m^3)
C_{smag}	Smagorinsky coefficient	(-)
c_β	Constant of proportionality for surface divergence model	(-)
$\overline{c}$	Mean gas concentration	(kg/m^3)
$\overline{\langle c \rangle}$	Horizontally averaged mean gas concentration	(kg/m^3)
Ca	Capillary number	(-)
Ca_T	Turbulent Capillary number	(-)
D	Gas molecular diffusivity	(m^2/s)
D_T	Turbulent diffusivity	(m^2/s)
E	Error in surfactant concentration	(kg/m^3)
E_T	Total diffusivity	(m^2/s)
H_c	Henry's constant	(Pa m^3/mol)
j	Gas flux	(kg/m^2/s)
K_L	Time-averaged gas transfer velocity	(m/s)
k_L	Instantaneous, horizontally averaged gas transfer velocity	(m/s)
k_l	Instantaneous local gas transfer velocity	(m/s)

k	Turbulent kinetic energy	(m^2/s^2)
L	Characteristic length scale	(m)
L_{11}	Turbulent length scale	(m)
L_∞	Integral length scale of the flow field	(m)
L_x	Computational domain size in x direction	(m)
L_y	Computational domain size in y direction	(m)
L_z	Computational domain size in z direction	(m)
Ma	Marangoni number	(-)
N	Number of grid points	(-)
$O(N)$	The order of accuracy	(-)
p	Generalised pressure (pressure over density)	(m^2/s^2)
Pr	Prandtl number	(-)
q	Coefficient in the power relation	(-)
r	Renewal rate	(1/s)
Re	Reynolds number	(-)
Re_T	Turbulent Reynolds number	(-)
Sc	Schmidt number	(-)
Sc_s	Surfactant Schmidt number	(-)
t	Time	(s)
Tu	Turbulence level	(-)
U	Characteristic velocity scale	(m/s)
u	Velocity component in x direction	(m/s)
v	Velocity component in y direction	(m/s)
w	Velocity component in z direction	(m/s)
u'	Fluctuating velocity	(m/s)
u_∞	Turbulent velocity scale	(m/s)
$\overline{u}$	Mean velocity component in x direction	(m/s)
$\overline{v}$	Mean velocity component in y direction	(m/s)

$\overline{w}$	Mean velocity component in z direction	(m/s)
We	Weber number	(-)
We_T	Turbulent Weber number	(-)
z	Vertical coordinate (pointed upwards)	(m)
ζ	Distance from the surface (pointed downwards)	(m)
ν	Kinematic viscosity of water	(m^2/s)
μ	Dynamic viscosity	(kg/m/s)
$\alpha_{ostwald}$	Dimensionless Ostwald constant	(-)
$\overline{\alpha}$	Averaged clean surface fraction	(-)
ρ	Density	(kg/m^3)
ρ_a	The density of a specific gas in air	(kg/m^3)
ρ_w	The density of a specific gas in water	(kg/m^3)
δ	The thickness of the concentration boundary layer	(m)
δ_t	Time interval	(s)
δ_v	The viscous penetration depth	(m)
Δ_t	renewal time or eddy age	(s)
β	Surface divergence	(1/s)
Λ	Characteristic turbulent length scale of large eddy	(m)
ϵ	Turbulent energy dissipation rate	(m^2/s^3)
ε	Small quantity for weights calculation WENO scheme (usually $\tilde{1}0^{-6}$)	(kg^2/m^6)
σ	Surface tension	(N/m)
σ_0	Equilibrium value of surface tension	(N/m)
γ	Surfactant concentration	(kg/m^3)
γ_0	Equilibrium value of surfactant concentration	(kg/m^3)
$\langle\gamma\rangle$	Horizontally averaged surfactant concentration	(kg/m^3)
γ_{th}	Surfactant threshold	(-)
η	Kolmogorov length scale	(m)
λ	Slip-length	(m)
$(.^*)$	Non-dimensional quantities	(-)

ABBREVIATIONS

CFD	Computational Fluid Dynamics
DNS	Direct Numerical Simulation
ENO	Essentially Non-Oscillatory
LES	Large Eddy Simulation
KCFlo	Kinetic energy Conserving Flow solver
LIF	Laser-induced Fluorescence
MPI	Message Passing Interface
PIV	Particle Image Velocimetry
SSE	Sum of the Squared errors
TBL	Thermal boundary layer
WENO	Weighted Essentially Non-Oscillatory
WENOM	Mapped Weighted Essentially Non-Oscillatory
W5	WENO5
W5-Z	WENO-Z
1D	One dimensional
2D	Two dimensional
3D	Three dimensional

Abstract

In this thesis, the effect of various levels of contamination on the interfacial air–water mass transfer of low diffusivity gasses is studied by Direct Numerical Simulation (DNS). The interfacial gas transfer is driven by isotropic turbulence, introduced at the bottom of the computational domain, diffusing upwards. The isotropic turbulence is generated in a separate large-eddy simulation (LES) that runs concurrently with the DNS.

Similar to Shen *et al.* [1], the damping effect of the surfactant contamination on the near surface (horizontal) velocities is modelled using horizontal gradients of the surfactant concentration. Important parameters in this model are the level of contamination and the turbulent Reynolds number. A large range of surfactant levels is studied including clean and fully contaminated surface condition. In the presence of surface contamination, the gas transfer velocity (K_L) was scaled as a power of Schmidt number (Sc^{-q}). The exponent q depends on the level of surface contamination. For instance, the gas transfer velocity K_L for a clean surface scales with $Sc^{-1/2}$, while for very dirty surfaces at scales with $Sc^{-2/3}$. For relatively low levels of contamination, parts of the surface area become nearly surfactant-free. Based on this observation a model is proposed for the prediction of K_L as a power of the Schmidt number. Where both the power and the constant of proportionality are functions of the average clean surface fraction $\overline{\alpha}$.

The effect of slip-length on interfacial gas transfer of atmospheric gasses into water was also investigated performing direct numerical simulations A model was proposed that expresses Ma/Ca_T in terms of slip length. The expression obtained was found to be dependent on Sc. This dependency was observed to be especially strong for low Schmidt numbers.

To perform the computational study, the convection of scalar concentration was solved by employing the weighted essentially non-oscillatory (WENO) scheme of Liu

et al. [2] with a fourth-order central discretization for diffusion in the $3D$ DNS. For the 2D surfactant convection, the WENO-Z (W5-Z) scheme was used, which was developed by Borges *et al.* [3]. In all simulations, a fourth-order central discretization was used for diffusion and the time integration of the convection-diffusion equation was executed by employing a third-order Runge-Kutta method .

In the flow solver, the convection of the velocity field is solved using a fourth-order unconditionally kinetic energy conserving method, while the diffusion was discretised using a fourth-order accurate central method.

Chapter 1: Introduction

1.1 Background and motivation

Air-water gas exchange is of fundamental concern in various environmental systems and industrial applications in a range of engineering disciplines. In a dynamic sense, the atmosphere and oceans are essentially linked. For instance, at the air-water interface, significant amounts of heat and atmospheric gases are exchanged between the oceans (and other water bodies) and the atmosphere. In fact, the oceans form a huge buffer for green house gases and heat. As a result, oceans tend to reduce the increase in the amount of CO_2 in the atmosphere which (these days) is mainly produced by human activity. Unfortunately, this leads to an increased acidification, resulting in the destruction of coral reefs and other aquatic life. Note that about 40% of the produced CO_2 is diffused into the ocean and the acidification of oceans is a result of the resulting increase of the amount of carbonic acid [4]. The production of carbonic acid reduces the CO_2 gas pressure which increases the capacity of oceans to absorb CO_2 from the atmosphere [5].

Also, as the oceans heat up, their capacity to store gases is reduced, which could result in the expulsion of large amounts of methane gas, which is a powerful greenhouse gas [6], [7]. Air-water heat exchange is an important driver of weather [8] (Kraus and Businger). The reduction in O_2 solubility is reduced and less O_2 is carried from the water surface to the deeper regions leading to an O_2 depletion [9]. The gas exchange process is not only important in relation with global warming but also with the re-aeration of lakes and rivers.

Climate change affects the balance between gases in the atmosphere and those absorbed in water bodies. A good understanding of the air-water gas transfer mechanisms helps to improve models used for the prediction of climate change. The research presented here mainly focuses on the effects of contamination on air-water gas exchange. Contamination does not only result from human activity but also from natural sources like excretions by bacteria and other life-forms.

Most flows that are found in nature are turbulent. A turbulent flow is characterised by seemingly random motions with many different scales. The largest scales (macro scales) in a turbulent flow are basically determined by the macro scales that characterise the geometry. Dissipation of turbulent kinetic energy mainly happens at the smallest relevant scales which can be several orders of magnitude smaller than the macro scales. In between the macro and micro scales a large range of scales exist at which turbulent kinetic energy is conserved (the so-called inertial range). Energy is exchanged between these scales in two directions (from large to small and from small to large). On average, however, the transport is from large to small scales. Kolmogorov discovered that the turbulent energy spectrum in the inertial range typically has a $\kappa^{-5/3}$ scaling.

The rate of air-water gas transfer is limited by resistance on the water side [10]. When approaching the water surface turbulence is increasingly damped. As a result, at the water surface itself gas transfer is fully dominated by diffusion. If no turbulence is present in the water body the diffusion of atmospheric gases towards the water bulk becomes extremely slow. If turbulence is introduced (for instance by wind shear, bottom shear or buoyancy), this process is significantly enhanced. Basically, turbulence acts to reduce the thickness of the diffusive concentration boundary layer adjacent to the surface allowing the diffusion at the surface to become more effective.

The typical concentration boundary layer thickness for atmospheric gases such as O_2 is about $\delta \approx 10 - 1000\mu$m [11]. So the measurement of this thin concentration boundary layer profile is extremely challenging. Therefore, in the past, many researchers used conceptual models to try and explain the gas transfer mechanism

using observable parameters. The film model is the simplest and oldest model developed by Lewis *et al.* [12]. In this model it is assumed that both sides of the interface are covered with a stagnant film between which molecular diffusion takes the place. Hence, gas transfer was assumed to be fully controlled by molecular diffusion and the gas transfer velocity K_L is related to the film thickness δ (m) by

$$K_L = \frac{D}{\delta} \text{ (m/s)}, \tag{1.1}$$

where D (m^2/s) is the molecular diffusion. The film thickness model is in fact a huge oversimplification of reality [13]. An improved model that takes surface renewal events into account was produced by Higbie [14] (penetration model). He recognised that turbulence plays an important role by periodically bringing fresh packages of unsaturated fluid from the bulk region to the surface, thereby replacing the saturated fluid at the surface by unsaturated fluid. The typical time Δt between two renewal events is referred to as the surface renewal time. Higbie assumed the surface renewal time Δt to be constant. Danckwerts [15] improved Higbie's model by no longer assuming a constant surface renewal time. Instead, he used a surface renewal rate r that is exponentially distributed, thereby obtaining the model

$$K_L \approx \sqrt{Dr} \text{ (m/s)}, \tag{1.2}$$

where r should be determined experimentally (or numerically).

Many researchers tried to to find expressions for the renewal rate r. For lower turbulent Reynolds numbers, Fortescue & Pearson [16] based their approximation of r on the typical time-scale associated with the large eddies in a turbulent flow, giving $r = u_\infty/\Lambda$, where u_∞ is the root-mean-square of the velocity fluctuations and Λ is the typical length scale of the large eddies. In this case the gas transfer velocity is

$$K_L = \alpha\sqrt{Du_\infty/\Lambda} \text{ (m/s)}, \tag{1.3}$$

where α is a constant of proportionality. For higher levels of turbulence, however, Banerjee [17] and Lamont [18] discovered that the characteristic time scales of the

small turbulent motions (small eddies) determined the renewal rate, and r was determined by $r = \sqrt{\epsilon/\nu}$, where ϵ is the turbulent dissipation rate at the interface and ν (m^2/s) is the kinematic viscosity. In this case, the gas transfer velocity is determined by

$$K_L = b\sqrt{D}[\epsilon/\nu]^{1/4} \text{ (m/s)}, \tag{1.4}$$

where b is the constant of proportionality.

Alternatively those two models can also be defined using u_∞ and Λ, in which case the large-eddy model reads

$$K_L Sc^{1/2}/u_\infty \propto Re_T^{-1/2}, \tag{1.5}$$

and the small-eddy model is given by

$$K_L Sc^{1/2}/u_\infty \propto Re_T^{-1/4} \tag{1.6}$$

After studying the results of various experiments and measurements, Theofanous *et al.* [19] proposed the two regimes model, which combines the large- and small-eddy models. He recognised that the large-eddy model is valid for small turbulent Reynolds numbers Re_T, while the small-eddy model should be used for large Re_T and the critical value of Re_T separating both regimes is approximately $Re_T = 500$. An alternative model for r, proposed by McCready *et al.* [13] is the surface divergence model. In this model, the two-dimensional divergence of the velocity at the surface (surface divergence β ($1/s$)) is used as a measure of the surface renewal rate. Using this model, the gas transfer velocity is given by

$$K_L \propto \sqrt{D\beta_{rms}} \text{ (m/s)}, \tag{1.7}$$

More detailed information on the gas transfer velocity models is given in Sections 2.2 and 5.5.3.

1.2 Objectives

In order to sustain aquatic life, the transfer of atmospheric gases from the air into water bodies, such as oceans, lakes, seas, rivers is very important. The transfer

of such low soluble gases across the air-water interface is controlled by resistance at the liquid side. At the water surface, the gas flux into the water is fully determined by molecular diffusion, The actual gas transfer velocity is closely related to the gas flux. The amount of diffusion is determined by the thickness of the concentration boundary layer underneath the surface. The thinner this concentration boundary layer is, the more diffusion of atmospheric gases will take place. Deeper down into the bulk, turbulent convection takes care of the transport of gases further down into the bulk, while the contribution of diffusion becomes negligible. In nature, the turbulence, that plays a very important role in promoting interfacial gas transfer can be introduced into the water by three distinct mechanisms. The first mechanism is surface-shear-induced turbulence (e.g. wind shear on open waters), the second bottom-shear-induced turbulence (e.g. in rivers) and the third buoyant-convective induced turbulence (e.g. in lakes due to surface cooling) [20]. Figure 1.1 shows a schematic illustration of the aforementioned turbulence sources. Note that in nature

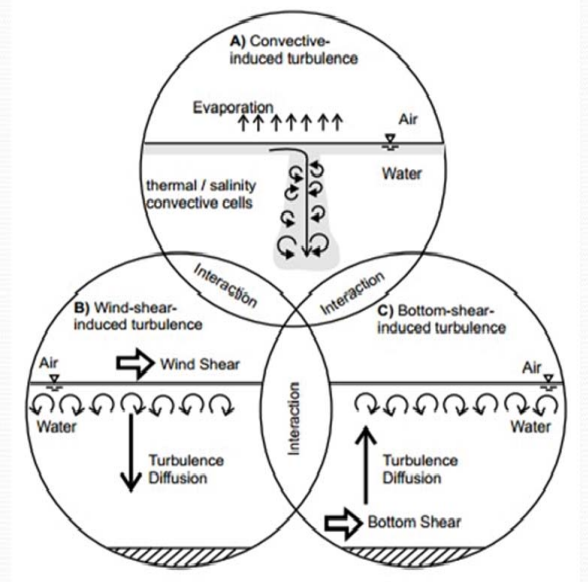

Fig. 1.1. Schematic illustration of the turbulence generating mechanisms and promoting gas transfer [20]

the turbulence generated by wind or bottom shear is typically anisotropic.

Many researchers focused on the gas transfer mechanism promoted by wind-shear-induced turbulence. Such turbulence is introduced directly at the water surface. This mechanism is very important as long as the wind speed is sufficiently high to produce sufficient shear. At low wind speeds (one or both of) the other mechanisms described above may become more important. In rivers and other water streams bottom shear-induced turbulence may be the most important turbulence source for the promotion of interfacial gas transfer. In sheltered lakes, on the other hand, buoyancy-driven gas transfer is often the dominant mechanism.

A major problem in nature is that water surfaces are not always clean. There are many ways in which the water surface can become polluted. An example is oil-spill or leakage of other chemical substances. This is especially problematic if these substances do not mix with water and remain floating at the surface. In the present work the focus is mainly on the gas transfer related to the reaeration of water in the presence of surface contaminations by surfactants. The gas transfer is assumed to be promoted by bottom-shear-induced turbulence. The following assumptions are made:

1. The surfactant is lighter than water.

2. Surfactant and water are immiscible.

3. The surface tension of water reduces linearly with increasing surfactant concentration

An example of a surfactant with the correct properties is oleyl alcohol.

The above assumptions are also mentioned in Section 5.1

Pollution by surfactants affects gas transfer across the air–water interface. Surface divergence typically leads to non-uniform surfactant concentrations, resulting in a local reduction of the surface stress of the water. Such a non uniform surface stress distribution induces Marangoni forces that effectively try to force the surface divergence to zero.

As mentioned in Section 1.1 The surface divergence model [13] relates the horizontally averaged gas transfer velocity to the horizontal velocity field at the surface. The

divergence of this horizontal velocity $\beta = \frac{\partial u}{\partial x}\Big|_i + \frac{\partial v}{\partial y}\Big|_i = -\frac{\partial w}{\partial z}\Big|_i$ can be used to estimate the surface renewal rate. It is known that this model $K_L \approx \sqrt{D\beta_{rms}}$ works well for low levels of contamination but what happens at higher levels of contamination ?

Even low levels of surface contamination can significantly affect interfacial gas transfer [1]. Though the physical mechanism has been partially identified in the past, a predictive model of surfactant contamination effects was missing. Using DNS (Direct Numerical Simulations) a parametric study was performed to assess the effects of contamination on gas transfer. Numerical data were analysed to develop and verify new models that can predict gas transfer in the presence of contamination. To investigate the above mentioned effects on the air-water gas transfer velocity, it was needed to perform a series of simulations covering a broad range of pollution levels of the water surface.

The research objectives are:

- Performing DNS calculations to understand the effect of surfactants on the interfacial gas transfer.
- Find a model for the gas transfer velocity given a known level of surface pollution with a immiscible surfactant such as Oleyl oil.
- To investigate the applicability of the surface divergence model in the presence of pollution by surfactants.
- Performing DNS calculations using various limited surface slip lengths to investigate the influence of slip length on interfacial gas transfer.
- To use both surfactant simulation results and slip-length simulation results to produce a model that connects the surface slip-length to the surfactant contamination level.

1.3 Methodology

In the present study, Direct Numerical Simulations (DNS) were employed to study the effect of contamination on interfacial gas transfer driven by isotropic turbulence that was introduced at the bottom of the computational domain. The bottom turbulence was generated in a separate large-eddy simulation(LES) of isotropic turbulence in a periodic box that ran in parallel with the main DNS.

The dimensionless Navier-Stokes equations are discretized on a non-uniform, staggered mesh, as explained in Section 3.2, and a second-order accurate Adams-Bashforth was used for the time integration. The convection of scalar concentration was solved by employing a weighted essentially non-oscillatory (WENO) scheme. This scheme was originally designed for shock capturing and was chosen because the aforementioned property makes it very suited to resolve accurately the steep concentration gradients that typically occur due to the very low diffusivity of atmospheric gases in water. The WENO scheme was developed by Liu *et al.* [2] as an improvement on the existing essentially non-oscillatory (ENO) schemes. As part of this research, the numerical code was extended in order to model $2D$ scalar transport of the surfactant at the air-water interface. The convection-diffusion equation for the surfactant was solved using a 2D version of the 3D scalar solver as implemented in the DNS. This 2D solver combines the WENO-Z scheme for surfactant convection with a fourth-order central discretization for diffusion, while the time integration of the convection-diffusion equation was carried out by employing a third-order Runge-Kutta method.

For the 2D surfactant convection, the WENO-Z (W5-Z) scheme, developed by Borges *et al.* [3], replaced the original WENO (W5) scheme of [2] (as used for solving the scalar convection in the main 3D DNS calculations). Compared to the original W5 scheme the W5-Z scheme was found to only need half the grid points in one direction in order to achieve the same resolution. This improvement in accuracy was achieved by an improved smoothness indicator in the determination of the weights.

In the flow solver, the convection of the velocity field is solved using a fourth-order unconditionally kinetic energy conserving method, while the diffusion was discretised using a fourth-order accurate central method. A detailed explanation of the computational method is presented in Chapter 3.

1.4 Outline

The introduction of the background and the motivation for the present research into the effects of contamination on the air-water gas transfer is presented in Chapter 1. This Chapter also presents the objectives and a brief overview of the methodology, which are more extensively presented in further chapters. Chapter 2 focuses on the review of relevant literature related to the air-water gas transfer mechanism. It presents existing conceptual models including their theoretical background as well as previously obtained results related to the effect of surfactant contamination on the near-surface properties of a turbulent flow. In Chapter 3 the methodology followed in the modelling of surface contamination by surfactants and the numerical techniques used in the the flow solver are detailed. Chapter 4 presents a comparison of the classical W5 scheme and the W5-Z scheme that was carried out by performing one- and two-dimensional test simulations and includes an order-of-accuracy determination and a comparison of the schemes on relatively coarse meshes. Chapter 5 presents the results obtained in the numerical simulations studying the effects of surfactant pollution on interfacial gas transfer. Here a model is presented that can be used to predict the actual gas transfer velocity based on the clean (uncontaminated) surface fraction and information on the turbulence in the water. In Chapter 6, it is investigated whether it is possible to model surfactant contamination by using a limited slip boundary condition at the surface. For relatively low Schmidt numbers (Sc) a model is presented that relates slip length to pollution level. Chapter 7, finally, presents the conclusions of the present work and also an outlook on further research.

Chapter 2: Literature review

Many environmentally important atmospheric gasses such as oxygen O_2, carbon dioxide CO_2, nitrous oxide NO, ozone O_3 and methane CH_4 have a very low diffusivity in water, which results in a high Schmidt number, Sc, which is defined by

$$Sc = \frac{\nu}{D}, \tag{2.1}$$

where D is the molecular diffusivity of the gas in water and ν is kinematic viscosity of the water. The transfer of atmospheric gases across the air-water interface is mainly restricted by the low diffusivity of these gases in water, which is significantly smaller than the diffusivity in the air phase, see e.g. Matthess [21].

Gas	Mass in dry air (%)	ρ_w in water (saturated) (g/m^3)	ρ_a in dry air at sea level (g/m^3)
O_2	23.2	9.1	278.4
CO_2	0.046	0.799	0.552
Ne	0.0012	0.000112	0.0144
He	0.00007	0.000001	0.00084
Ar	1.28	0.77	15.36
N_2	75.47	14.94	905.64

Table 2.1
Density (in air and water) of various atmospheric gases at 20^{o}C

Gas concentration boundary layers are formed at both sides of the air-water interface. The density of specific gases in air, (ρ_a), and in water, (ρ_w), usually differ significantly (see Table 2.1). The concentration on both sides is related by the dimensionless Ostwald coefficient of solubility α_o.

$$\rho_w = \alpha_o \times \rho_a,$$

Where α_o usually is significantly smaller than one, see Jaehne & Haubecker [22] and Liss [23].

Above we have seen that typically the concentration in air, the concentration of atmospheric gasses in the water phase under saturated conditions decreases. In other words, the density of atmospheric gasses reduces in the water phase [24]. For example, the density of air is $\rho_a = 1200\text{g/m}^3$ and air contains 23.2% by weight of O_2. Dissolved O_2 has a density of 9.1g/m^3 (fully saturated) in the water phase, given a specific density of $\rho_{O_2,a} = 278.4\text{g/m}^3$ for O_2 in the air at sea level. An overview of the density of several atmospheric gasses in water and air phases at 20^oC is shown in Table 2.1 A schematic of the resulting concentration boundary layers (for oxygen) on both of the air-water interface is shown in Figure 2.1 Schmidt numbers of atmospheric

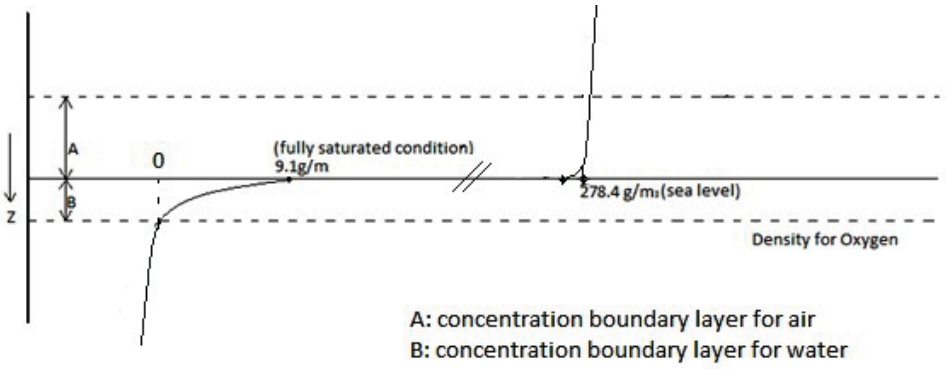

Fig. 2.1. Schematic of the gas concentration boundary layers on both sides of air-water interface

gases in water are typically quite high. Which corresponds to a very low diffusivity of these gases in water. Suppose diffusion were the only mechanism for re-aeration

of a body of oxygen-depleted water of $d = 1$m depth. The corresponding diffusion time is given by $t_{diff} = d^2/(2D)$, which corresponds to the time it would take for the water to be aerated. Given that the Schmidt number for O_2 is $Sc = 500$, while the kinematic viscosity of water is $10^{-6}\mathrm{m}^2/\mathrm{s}$, the diffusivity of O_2 in water would become $D = 0.2 \times 10^{-8}$ m^2/s. So that at $d = 1$m

$$t_{diff} \approx \frac{1^2}{0.4 \times 10^{-8}} = 2.5 \times 10^8 \,\mathrm{s}, \tag{2.2}$$

which corresponds to almost 8 years.

2.1 Fundamental Equations

The gas transfer rate is related to the gas flux at the water surface which is fully controlled by molecular diffusion. Slightly further below in the water, turbulent mass flux (while transporting dissolved gases towards the bulk region of the water) acts to reduce the thickness of the diffusive concentration boundary layer. This interplay between diffusion and turbulent mass flux, resulting in a gas concentration boundary layer of limited thickness, plays an essential role in the air-water gas transfer mechanism.

In practice, the thickness of the concentration boundary layer is very small. It is restricted to about $\delta = 10 - 1000\mu m$ [11]. This limited concentration boundary layer thickness at the interface indicates that below the water surface molecular diffusive processes are quickly replaced completely by turbulent convection processes. The gas transfer process is characterized by the gas flux ($\vec{j}$) and the molecular diffusion is defined by Fick's law. The gas flux is proportional to the gas concentration gradient and the coefficient of molecular diffusion D (m^2/s) so that

$$\vec{j} = -D\nabla c, \tag{2.3}$$

where c is the transferred gas concentration. In the present study, the (downward) gas flux takes place across a horizontal homogeneous, perfectly flat plane and the gas transfer is given by

$$j = -D\frac{\partial c}{\partial z}\bigg|_i,$$

where the subscript i denotes the interface (surface) and z corresponds to the vertical direction.

Note that the positive z-direction is upwards and the positive j direction is downward. Deeper down in the body of water the turbulent mass flux will takes over, so that the above equation for the averaged gas flux becomes

$$\overline{j} = -D\frac{\partial \overline{c}}{\partial z} + \overline{c'w'}, \tag{2.4}$$

where $\overline{c}$ is the mean concentration and the $\overline{c'w'}$ represents turbulent mass transfer, in which c' and w' are the concentration and z-velocity fluctuations and $\overline{(.)}$ denotes averaging. The first term at the right-hand-side of Eq. (2.4) identifies molecular diffusion transport.

Gas transfer flux is mostly expressed in terms of the so-called gas transfer velocity K_L, which is the quantity that one usually needs to determine in both experiments and numerical simulations. The gas transfer velocity is defined by rescaling the gas flux j and is determined by

$$K_L = \frac{j}{\Delta c} = \frac{j}{c_s - c_b}, \tag{2.5}$$

where c_b is defined dissolved gas concentration in bulk region of the water and c_s is the gas concentration at the surface, which can be obtained from Henry's law. The transfer of low solubility gases is largely controlled by resistance at the liquid side. The actual mass transfer velocity (K_L) is related to the gas transfer coefficients for the liquid (water) phase k_l and the gas (air) phase k_g, respectively. The relation is defined by

$$\frac{1}{K_L} = \frac{1}{k_l} + \frac{1}{H_c k_g} \tag{2.6}$$

with H_c denoting Henry's constant, which plays a vital role to determine the resistance of the water side of the interface. So if the ratio of $k_l/H_c k_g$ is large, the gas (air) side

resistance takes control of the transfer mechanism, whereas the liquid side resistance governs the transfer process when the ratio has a small value.

The value of Henry's constant is inversely related to the gasses that are of environmental interest such as O_2, N_2, CO_2, CO. Those gasses have very low solubility and, consequently, they have a very high Henry's constant. From this, it can be concluded that the transfer of atmospheric gasses across the air-water interface is mainly governed by the dynamics at the liquid side of the flow [25].

As mentioned earlier, for very low-diffusivity atmospheric gasses, the transfer process is controlled by a very thin aqueous concentration boundary layer with a typical thickness of $\delta \sim 10 - 1000\mu m$. This thickness is directly affected by the mass diffusivity D, and the time scale and intensity of turbulence level.

2.2 Gas Transfer Model

The importance of gas transfer across the air-water interface is explained in the previous pages. In order to obtain a better understanding of the actual gas transfer velocity K_L, it is necessary to elucidate the composition (terms) of the total mass flux. Because of the difficulites encountered performing measurements inside the ultra-thin concentration boundarylayer, in the past many researchers Oconnor & Dobbins [26], Churchill *et al.* [27], Thackston & Krenkel [28], Plate & Friedrich [29], Gulliver & Halverson [30], Moog & Jirka [31], Turney *et al.* [32], focussed their efforts to establish statistical relations between the actual gas transfer velocity and (a few) observable flow parameters. To achieve this, researchers developed and improved theoretical models for the gas transfer velocity K_L that take some of the most important physics into account. Indeed, the gas transfer velocity K_L is associated with certain flow parameters, but to understand the actual gas transfer mechanism, the mere quantification of K_L is not sufficient.

Models for the gas transfer velocity can be divided into three groups which will be discussed below:

1. Theoretical or Conceptual Models;

2. Eddy Diffusivity Models;

3. Hydrodynamic Models.

2.2.1 Theoretical Models

"Conceptual models are simple solution of the vertically one-dimensional diffusion equation without any explicit advective flow field. The effect of turbulence is incorporated through initial condition and boundary condition. Which are characterized by time and spatial scales" Brumley & Jirka [33]

2.2.1.1 Film theory

This is the simplest and oldest model that describes the gas transfer process. It was introduced by Lewis *et al.* [12] and assumes that each side of the air-water interface is covered with a stagnant film, where the molecular diffusion takes place. Transport was determined by the thickness of the stagnant film and the bulk region of the water was assumed to be fully mixed [12]. They actually tried to find a reliable relation between resistances of the liquid phase and the gas phase for a variety of atmospheric gasses with different solubilities in water.

The film theory predicts a relation between K_L and the thickness δ of the film, thus

$$K_L = \frac{D}{\delta} \text{ (m/s)}, \tag{2.7}$$

where D (m^2/s) is the molecular diffusivity and δ (m) is the thickness of the stagnant film.

2.2.1.2 Penetration theory

An improved model that takes surface renewal events into account, was developed by Higbie [14] (penetration model). He recognised that turbulence plays an important role by periodically bringing fresh packages of unsaturated fluid from the bulk region to the surface, therefore replacing the saturated fluid at the surface by unsaturated fluid. The typical time Δt between two renewal events is referred to as the surface renewal time. Higbie assumed the surface renewal time Δt to be constant. The penetration model is given by

$$K_L \approx \sqrt{\frac{D}{\pi \Delta t}} \text{ (m/s)} \tag{2.8}$$

2.2.1.3 Surface renewal theory

Danckwerts [15] improved Higbie's model by no longer assuming a constant surface renewal time. Instead, he used a surface renewal rate r that is exponentially distributed, therefore obtaining the model

$$K_L \approx \sqrt{Dr} \text{ (m/s)}, \tag{2.9}$$

where the renewal rate r has to be determined by performing experiments. The prediction of gas transfer rate across the interface between the gas phase and the liquid phase is improved through both these theories. Following that the relation between K_L and D was built by using penetration and surface renewal theories and modelled by

$$K_L \approx D^n \text{ (m/s)}, \tag{2.10}$$

where n is power of the diffusivity, with can assume any value between $n = 1/2$ and $n = 2/3$, depending on surface hydrodynamics conditions, see e.g, Jähne *et al.* [34]. According to the experiment and studies of Jähne *et al.* [35] and Upstill *et al.* [36], the surface renewal theory was found to be a significant improvement compared to the film theory.

2.2.1.4 Random eddy theory

A problem related to the surface renewal theory is that the eddies do not renew the interfacial layer completely. This is proven by laboratory experiments. The thermal boundary layer (TBL) is not renewed by a fraction of the renewal events Jessup *et al.* [37]. The random eddy model proposed by Harriott [38] addressed this issue. He stated that eddies that approach the surface at random times play a significant role in promoting the gas transfer process by improving the gas flux. Due to the random life span of eddies, they only reach up to a certain random distance from the interface. Closer to the interface, molecular diffusion fully dominates, resulting in a finite variable thickness of the concentration boundary layer. This finding gives an opportunity to propose a relation between the random eddy life time and its random minimum distance to the surface (depth).

2.2.1.5 Surface divergence theory

McCready *et al.* [13] proposed the surface diverge model. It relates the horizontally averaged gas transfer velocity K_L to the horizontal velocity field observed at the surface. The divergence of this horizontal velocity field at the surface is given by

$$\beta = \left(\frac{\partial u}{\partial x} + \frac{\partial v}{\partial y}\right)\bigg|_i = -\left.\frac{\partial w}{\partial z}\right|_i, \tag{2.11}$$

where β is the surface divergence, which can be used as a measure of the surface renewal rate r. When using $r = \beta_{rms}$ $(1/s)$, the surface renewal model becomes

$$K_L \propto \sqrt{D\beta_{rms}} \tag{2.12}$$

2.2.2 Eddy Diffusivity Models

Possibly with the exception of Harriott's random eddy model, the models discussed above did not take into account many of the turbulent characteristics of the background turbulence that usually drives interfacial gas transfer. Eddy diffusivity

models, on the other hand, employ multiple scales that vary with depth. The eddy diffusivity models are generally defined by

$$E_T = D + D_T, \tag{2.13}$$

where E_T is the total diffusivity, D is the molecular diffusivity, and D_T is the turbulent (or eddy) diffusivity. Based on this, the z-component of the mass flux is given by

$$J_E = -(D + D_T)\frac{\partial c}{\partial z} \tag{2.14}$$

The turbulent diffusivity D_T is determined as a function of depth using a power dependency given by $D_T = \omega z^n$, where $n > 0$ and ω $(1/\mathrm{s/m}^{n-2})$ is a constant. Hence the gas transfer velocity becomes $K_L \sim D^m$ where $0 < m < 1$ depends on the magnitude of n. So that for a free-slip surface

$$D_T = \omega z^2 \text{ and } K_L \sim Sc^{-1/2}, \tag{2.15}$$

while for a smooth solid (no-slip) surface

$$D_T = \omega z^3 \text{ and } K_L \sim Sc^{-2/3}. \tag{2.16}$$

2.2.3 Hydrodynamic Models

A lot of effort has been made to verify and further improve the gas transfer models and a number of researchers tested and developed various theories in order to elucidate the renewal rate term r for a range of measurable turbulent scales.

2.2.3.1 Large eddy model

A further improvement to the surface renewal model was suggested by proposing the large-eddy model. This approach was introduced by Fortescue & Pearson [16]. They assumed that the largest eddies take control of surface renewal events responsible for the interfacial gas transfer mechanism. They suggested that r is related to the typical time-scale associated with the large eddies in a turbulent flow. Hence, they

proposed the relation $r = u_\infty/\Lambda$, where u_∞ is the root-mean-square of the velocity fluctuations and Λ is the typical length scale of the large eddies. As a result, the gas transfer velocity is given by

$$K_L = \alpha\sqrt{\frac{Du_\infty}{\Lambda}}\ (\mathrm{m/s}), \tag{2.17}$$

where α is a constant proportionality.

2.2.3.2 Small-eddy model

Moreover, Banerjee [17] and Lamont [18] suggested, as an alternative to the large-eddy model, the so-called small-eddy model. They suggested that it was the time-scale related to the small-eddies that was most important and, hence, dominates the gas transfer process. In this model, the renewal rate (r) is estimated using the Kolmogorov time-scale $\sqrt{\frac{\epsilon}{\nu}}$, where ϵ is the turbulent energy dissipation rate at the interface, ν is the kinematic viscosity, so that

$$K_L = b\sqrt{D}(\frac{\epsilon}{\nu})^{\frac{1}{4}}\ (\mathrm{m/s}), \tag{2.18}$$

where b is a constant of proportionality. After substituting the renewal rate into the transfer velocity, K_L can be written as [39]

$$K_L \sim {S_c}^{-1/2} u_\infty {Re_T}^{-1/2}\ (\mathrm{m/s}) \tag{2.19}$$

for the large-eddy model and

$$K_L \sim {S_c}^{-1/2} u_\infty {Re_T}^{-1/4}\ (\mathrm{m/s}) \tag{2.20}$$

for the small-eddy model. Where S_c is Schmidt number defined in Eq. (2.1) and Re_T is the turbulent Reynolds number defined by

$$Re_T = \frac{u_\infty \Lambda}{\nu} \tag{2.21}$$

Note that the dissipation rate of the small-eddy ε scale is estimated on the large-eddy scale as $\varepsilon = {u_\infty}^3/\Lambda$.

Based on results from various experiments, Theofanous *et al.* [19] proposed the two regimes model. This model is associated with both eddies models. Which of the two models is valid was found to depend on the actual intensity of the turbulence, which is proportional to Re_T. Therefore, the large-eddy model is valid for low turbulence intensity with $Re_T < Re_{T,crit}$ and the small-eddy model is valid for high turbulence intensity with $Re_T > Re_{T,crit}$, with $Re_{T,crit} \approx 500$. This dual regime proposal is supported by many experimental results, see e.g, Theofanous [40], Chu *et al.* [41], and Asher & Pankow [42].

2.3 Gas transfer into a turbulent water body

Gas transfer mechanism across the air-water interface plays an important role into the re-aeration of oceans. The gas transport process is controlled by interaction of molecular diffusion and turbulent convection near the water surface. Diffusion processes are mainly only important in a very thin aqueous boundary layer close to the surface, while further down turbulent gas transfer processes became (fully) dominant. High gas concentration fluid is transferred by turbulent motions across the concentration boundary layer into regions with low concentration, resulting in steep concentration gradients. Furthermore, the turbulent gas transfer significantly affects the diffusive concentration boundary layer thickness. Upwelling motions locally suppress (reduce the thickness of) the concentration boundary layer while downwelling motions tend to thicken the boundary layer. These constant instantaneous changes in local boundary layer thickness have the time-averaged effect of reducing the overall thickness of the concentration boundary layer resulting in a steeper concentration gradient at the surface. This steeper concentration gradient $(\partial c/\partial z)|_i$, in turn, results in an increased diffusive gas transfer velocity.

As mentioned earlier, as there are no velocity fluctuations at the surface itself, the local contribution of the vertical turbulent gas transfer (flux) to the total gas flux will be zero at the surface. In other words, the vertical gas transfer is fully

dominated by molecular diffusion. Deeper down into the water body the importance of the diffusive gas transfer term quickly reduces and the turbulent gas transfer takes over the vertical transport of gases further down into the bulk. Increased levels of turbulence in the water will result in thinner diffusive concentration boundary layers leading to a larger diffusive mass transfer, and hence larger gas transfer velocities. In natural water bodies turbulence is ubiquitous, and most flows will be turbulent rather than laminar. Over the years turbulent flows have been quite widely studied and a significant amount of theoretical knowledge has been developed, see e.g., Tennekes *et al.* [43], Pope [44] and Pozrikidis [45].

Above, it was mentioned that the turbulence intensity is an important factor that influences the thickness mass boundary layer δ. Another parameter that directly affects the thickness of the concentration boundary layer is the Schmidt number Sc. Herlina & Wissink [11] made a direct comparison between simulation results obtained at different Sc number and found that the concentration (diffusive) boundary layer becomes thinner with increasing Schmidt number. In fact, in the absence of shear stress (free slip surface) the thickness of concentration boundary layer δ_{DBL} was found to scale with Sc as

$$\delta_{DBL} \propto S_c^{(-1/2)}. \tag{2.22}$$

Many researchers investigated the gas exchange mechanism in the presence of turbulent flow, see e.g., [46], [47], [48], [20], [10], and [49]. In the environment, turbulent(vertical) mass flux can be generated by various distinct sources, namely buoyant convection, bottom shear and wind shear. These sources will be discussed in more detail below.

2.3.1 Buoyant convective turbulence

The oxygen transfer that occurs due to gravitational instability is especially important under low wind-speed conditions. The water surface cools down at night and a layer of relatively heavy cold water forms on top of the lighter, warmer bulk.

Because of this unstable stratification cold, atmospheric gas-saturated water from the surface will eventually begin to sink and is replaced by warmer, unsaturated water from the bulk. Buoyant convective instability-induced turbulent mass transfer was investigated, for instance, by Deardorff *et al.* [50] using laboratory experiments. Also, Katsaros *et al.* [51] carried out experiments in the laboratory with tanks placed in a controlled environment to be able to investigate convective instability.

Turbulence was measured in an oceanic convective mixed layer during a cold-air outbreak by Shay & Gregg [52] in the upper ocean. They established a relationship between the turbulent dissipation rate and the surface buoyancy flux. Subsequently, Shay & Gregg [53] studied a buoyant convective instability near the Bahamas that was generated by daytime heating and evaporative cooling at night. The plumes generated by the convective instability were observed to penetrate up to 100m deep. The relation between buoyancy induced turbulence and sea surface temperature was studied by Graham & Barnett [54]. They found that for large scale deep penetrative (buoyant) convection to take place in the Indian and Pacific oceans, it is needed that the water surface temperature exceeds 27.5^oC. Further increases in sea surface temperature, however, did not produce any additional effect. Sea surface temperature was associated between convection and surface wind divergence, this study [54] was conducted and according to their results, sea surface temperature is not necessary to be over 27.5^oC for very effective convection although wind divergence is quite related with deep convection. Similar studies were performed in a lake environment by Imberger [55]. Other researchers studying buoyancy convective instability driven turbulent convection in lakes were Brubaker [56], Sander *et al.* [57] and Jonas *et al.* [58]. The turbulent transport model of Zeman & Lumley [59] was also concerned with buoyancy instability effects on the vertical flux through the mixed layer. However, none of the above works really addresses the convective transfer of atmospheric gases by the buoyant convective instability. Macintyre *et al.* [60] expanded the scope of the research into penetrative (buoyant) convection by including investigation into the gas transfer coefficients due to wind shear and penetrative convection through

the mixed layer. Subsequently, Eugster *et al.* [61] investigated CO_2 gas exchange across the atmosphere and the surface of lakes via a buoyant convective instability by using the eddy covariance method and the surface renewal model to calculate the gas transfer velocity. Their data showed the importance of periods of heat loss and convective mixing to the gas transfer process. Lee [62] studied the transport of O_2 from teh atmosphere into the water driven by a convection instability. The oxygen mixing in the water body was visualised by using a fluorescence oxygen visualization technique. Schladow *et al.* [63] examined the gas transfer process driven by natural convection in reservoirs and lakes. A cool surface layer was created in the laboratory experiments to create a gravitational instability and the oxygen transfer fluorescence imaging technique was used measure the evolution of the O_2 concentration in the water. Their results confirm that the buoyancy-driven vertical flux of cold water is an important source for the vertical transfer of O_2 towards the bulk of the water.

At low wind speeds, the gas transfer will be dominated by buoyancy and driven by temperature differences between the (cool) surface and the (relatively warm) bulk. To investigate the effectiveness of this process in more detail, Direct numerical simulations (DNS) were performed by Wissink & Herlina [64] who calculated heat and gas transfer into the water body driven by a buoyant-convective instability. They used a Prandtl number of ($Pr = 6$) and performed simulations for a range of Sc numbers ($Sc = 20$ to 500). Plumes of cold, saturated fluid were found to penetrate deep into the water bulk causing an effective mixing of unsaturated warm water with the saturated cold water. Another study related to the determination of the surface age given a buoyant convective instability was reported by Ali *et al.* [65]. DNS calculation results were used in conjunction with Danckwerts *et al.* [15] model to determine the heat transfer velocity. The surface age was determined using a Lagrangian particle tracking method.

2.3.2 Wind shear induced turbulence

Wind shear-induced turbulence an important mechanism for the promotion of air-water gas transfer. For sufficiently strong winds, the turbulence produced by wind shear causes quick mixing and enhances the heat and gas transfer. Wind shear is produced at the water surface. When the wind speed is above 3 m/s, considerable wave growth is generated which may result in wave breaking. Jähne *et al.* [66] studied the gas exchange in a circular wind/water tunnel. The gas transfer velocity was found to linearly increase with increasing wind speed up to about $8m/s$. Jähne *et al.* [34] also performed experiments in circular and linear wind/wave tunnels where they carried out gas transfer measurements. The results indicate that the gas transfer across the wavy surface of the water was best represented by the mean square of the slope of the waves. Merlivat & Memery [67] found that the gas transfer velocity linearly changes with friction velocity u_τ when the u_τ increases from $3m/s$ to $9m/s$. Jähne & Haußecker [68] found similar results, which confirmed that the gas transfer velocity is also a function of the surface friction velocity and not just only wind speed.

The effect of various wind speeds (< 10 m/s) on the gas transfer velocity in the presence of surface films was studied by Frew *et al.* [69]. Again, it was found that the gas transfer velocity is stronger correlated with the mean square slope of the waves than with the speed of wind. Lee & Saylor [70] conducted experiments in a wind tunnel to study the O_2 transfer across a contaminated surface under mixed convection conditions. The effect of wind shear induced turbulence on the formation of a concentration boundary layer at the water surface was studied by Wolff & Hanratty [71], Woodrow & Duke [72], Munsterer *et al.* [73], Munsterer [74], Munsterer & Jähne [75] and Peirson [76]. They attempted to predict the thickness of the (extremely thin) concentration boundary layer and reported significant difficulties to obtain results of reasonable quality. Measurements of the instantaneous concentration profiles on the water side were reported by Wolff & Hanratty [71] and Peirson [76]. They used the PIV technique to estimate the concentrated boundary layer thickness within the aque-

ous surface viscous sub-layer. Munsterer & Jähne [75] used laser-induced fluorescence (LIF) to approximate the concentration boundary layer thickness. Oconner [77] established a relation between the gas transfer velocity and the wind velocity for smooth surface conditions with low wind speeds and for rough surface conditions with high wind speeds. Kitaigorodskii [78] used the analogy with turbulence over rigid-wall surface to estimate the gas transfer velocity (K_L). Chu & Jirka [79] experimentally studied interfacial gas transfer (oxygen) in the presence of wind shear in wind/water tunnel. Gas transfer rates were investigated for various wind speeds in the presence of bottom-shear (water stream). It was found that the air shear velocity is an effective parameter to describe the gas transfer mechanism in the absence of bottom shear. The relation between K_L and wind speed was also investigated by Crusius & Wanninkhof [80] who performed measurements at various wind speeds.

Kunugi*et al.* [81] performed a Direct Numerical Simulation for turbulent flow with wind shear to study carbon-dioxide gas transfer at the interface. The results obtained from the simulation were compared to experimental data. It was found that the exchange coefficient of carbon-dioxide gas at the free surface, as found in their study, was in good agreement with existing experimental data. Direct Numerical Simulation was also performed by Kurose *et al.* [82] for two phase turbulent flows with wind-induced shear without breaking waves. The arbitrary Lagrangian-Eulerian method was used to capture the wind-driven waviness at the interface. It was found that the surface divergence was a suitable parameter for the estimation of the heat transfer coefficients on both the gas and liquid sides.

Finally, a direct numerical simulation of turbulent heat transfer across a deformable, sheared gas-liquid interface was carried out by Lakehal *et al.* [83], where the flow velocity was defined in the opposite direction of the air velocity.

2.3.3 Bottom shear induced turbulence

Shear generated at the bottom is the source of turbulence in flowing streams. If wind speeds are quite weak in a stream environment, bottom-shear-induced turbulence become dominant and drives the gas transfer mechanism. Many researchers attempted to build relations between gas transfer velocity and various flow properties. These relations are usually experimental or based on computational analyses, see e.g., Churchill *et al.* [27], Thackston & Krenkel [28] and Gulliver & Halverson [30]. The aforementioned researchers used entirely empirical methods to obtain gas transfer models, while s semi-empirical method was emplyed by O'Conner & Dobbins [26]. The re-aeration coefficient was fitted to the vertical gas transfer coefficient and the square of the average depth by Thackston & Krenkel [28]. A vortex model for gas transfer in open channels was derived from the gas transfer model by Gulliver & Halverson [30].

Plate & Friedrick [29] studied the re-aeration of open channel flow and evaluated various turbulent cases. The first case evaluated concerned bottom-shear induced turbulence, the second case concerned wind-shear induced turbulence while in the last case these two sources of turbulence were combined. They were able to relate the gas transfer velocity (K_L) to root mean square of the horizontal component of the velocity near the surface. Further experiments were conducted by Jïrka & Ho [84], Moog & Jïrka [85], Moog & Jïrka [86] and Moog & Jïrka [31]. Their experiments were performed in an open channel and the effect of surface roughness on interfacial gas transfer was studied. They found that gas transfer rates agreed with macro roughness and showed the validity of the small eddy model.

Atmane & George [87] also performed research in bottom-shear-induced turbulence flow. They tried to quantify turbulent mass flux using the eddy-correlation method. Mckenna & McGillis [46] performed measurements of gas transfer in a tank with grid-stirred turbulence. Their experiments were carried out with various levels of contamination at the interface. They proposed that the turbulence in the bulk, is

not as effective as expected due to presence of surface films. The relation between surface divergence and gas transfer velocity was determined for the case of interfacial contamination. It appeared that the surface divergence is an important parameter for interfacial gas transfer, see also Brumley [88]. Tamburrino & Gulliver [89] also studied the relation between mass transfer in an open channel flow and free surface turbulence. Studies at various Re numbers were performed in the range $8,500 - 45,000$, while in the Mckenna & McGillis [46] study they ranged from $Re_T = 282$ to 974. Based on their experiments, combined with the study of Gulliver & Halverson [30] who used the same facility, and with the study of Lau [90] (performed in a different facility), they derived the relation $K^+\sqrt{Sc} = 0.24\sqrt{S^+{}_{\beta max}}$ where K^+ is the liquid-film coefficient and $S^+{}_{\beta max}$ is the maximum value of the surface divergence β spectrum. These are dimensionless values which are normalised by the kinematic viscosity and shear velocity.

Suga and Kubo [91] used an extended version of the analytical wall-function (AWF) which was designed for Reynolds-averaged Navier Stokes simulations (RANS) to prescribe surface mass transfer rates and turbulent concentration fields across undeformable air-water interfaces at Sc numbers ranging from $1 \leq Sc \leq 1000$

The results of near-surface hydrodynamic measurements in a grid stirred tank were reported by Brumley & Jirka [92]. A rotating split-film velocimeter was used to produce a detailed mapping of vertical and horizontal turbulence structures. From their measurements and by employing Hunt & Graham [93] theory, they were able to identify different near-surface hydrodynamic layers. A schematic of these hydrodynamic layers is shown in Figure 2.2.

It was suggested that kinematic effects related to the presence of the surface are expected to extend up to one integral length scale from the surface, therefore identifying the so-called surface influenced layer. The viscous sub-layer is the thin layer next to the surface where viscous effects dominate (and the flow is basically always laminar). The thickness of this layer is of the order of $L_\infty {Re_T}^{-1/2}$ [94], where L_∞ is the integral length scale and Re_T is the turbulent Reynolds number.

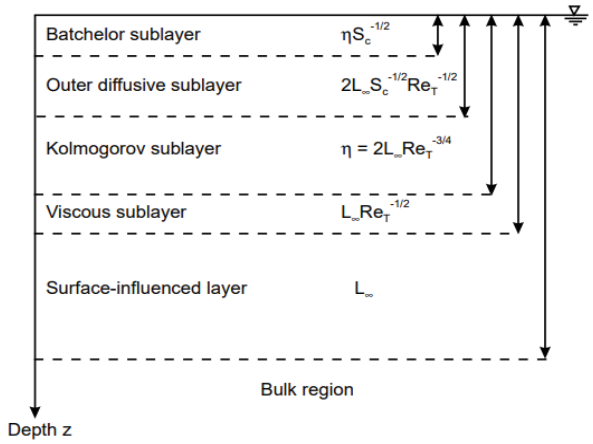

Fig. 2.2. Schematic illustration showing estimation of hydrodynamic layers (Brumley&Jirka) [88]

The thickness of the Kolmogorov sub-layer, which is on the order of $\eta = 2L_\infty {Re_T}^{-3/4}$, identifies the scale of the smallest eddies in isotropic turbulence. The outer diffusivity layer, with a thickness scaling with the size of the largest eddies, is estimated to be of the order of $2L_\infty {Re_T}^{-1/2} Sc^{-1/2}$. The thickness of the Batchelor sub-layer, finally, is again related to the smallest eddies and is of the order of $2L_\infty {Re_T}^{-3/4} Sc^{-1/2}$.

2.4 Surface Film Effects

2.4.1 Surface tension

Surface tension is one of the most important properties of the fluid surface. The existence of such a large inward attraction between fluid molecules is related to cohesive forces between water molecules which causes a surface tension at the air-water interface. Compared to many other fluids, the surface tension of water is especially large, e.g., for water at 20^oC a value of 72.8^{-3} N/m is obtained. These strong forces work to e.g. counteract any deformation applied to water surfaces. Surface tension is also responsible for the spherical shape of water droplets and bubbles (because for

spherical shapes surface tension is identical at every surface location). Surface tension is usually denoted by the symbol σ and its dimension is force per unit length, i.e.

$$\sigma = F_s/L, \tag{2.23}$$

where F_s is the stretching force (in Newton) and L is defined unit length (in metre). Surface tension depends on the physical properties of the fluid and is function of temperature and pressure, see e.g., Sabersky *et al.* [95]. Several experimental methods for the determination of surface tension were assessed by Lapham *et al.* [96]. The situ tensiometry technique, for instance, determines surface tension from the retraction of a thin-walled tube from the liquid interface. Repeatable results were obtained measuring the surface tensions of an alcohol-in-water solution, tap water and a surfactant water solution.

2.4.2 Surfactants

It is known that the presence of surfactants have considerable effect on gas transfer across the air-water interface [97]. The gas transfer velocity K_L is affected by the cleanliness of the surface, and turbulent velocity fluctuations are more or less strongly damped depending on the level of surfactant pollution. When the surface is covered by surfactants, greater tangential stress occur due to local variations in surface elasticity due to the dependency of surface tension on the surfactant concentration. As will be explained later, surfactant-induced local variations in the surface tension result in the damping of near-surface turbulence. The laboratory experiments of Broecker [98] showed that the gas transfer velocity reduced in the presence of surfactants.

When a surface is covered with active agents, the surface free energy will reduce. On the other hand, surface tension is decreased with increasing levels of surface active agents or surfactants. Experimental determination of the influence of surfactant concentration on surface tension for soluble and insoluable surfactants was attempted by Rideal & Robb [99]. Furthermore, several experimental studies were carried out on the effect of surfactants on gas transfer processes, see e.g., in Asher & Pankow

[42], Mckenna & McGillis [47], Saylor *et al.* [100], Tsai & Liu [101] and Tsai & Yue [102]. Surfactants are either soluble or insoluble. The insoluble surfactants may form something like a barrier film at the water surface. The thickness of these surface films, however, is severely affected by the effect of waves and winds condition and other sources of turbulence. Soluble surfactants tend to dominate the gas transfer process even in breaking wave conditions that occur in the presence of very strong winds, see e.g., Goldman *et al.* [103], Bock *et al.* [104]. An insoluble surfactant that is relevant to the present study is Oleyl alcohol. This is an unsaturated fatty alcohol and the molecular formula is $C_{18}H_{36}O$ with a condensed structural formula given by

$$CH_3(CH_2)_7 - CH = CH - (CH_2)_8OH. \tag{2.24}$$

Surfactants can affect a wide variety of free surface processes. One of these effects concerns capillary waves which can be reduced by a range of surfactants [105]. Horizontal gradients in the surfactant concentration at the interface tend to generate surface tension gradients that damp turbulent motion. This was confirmed by Tsai [106] who studied the effect of contamination on turbulent and laminar flow and also by Lee & Saylor [70] who also found that the presence of surfactants resulted in a noticeable reduction of the effect of subsurface turbulence. Zhang *et al.* [107] investigated the effect of insoluble surfactants in the presence of zero mean surface stress by performing a numerical simulation for interfacial gas transfer driven by buoyant convection induced turbulence. A Direct Numerical Simulation was also performed for an open channel by Handler *et al.* [108]. Their works were related to the influence of surfactants on heat transfer. The intensity of the turbulence was reduced significantly with increasing surfactant elasticity and Handler *et al.* [108] found that the turbulent velocity fluctuations were significantly reduced. Also, a significant reduction was found of the average temperature at the free surface.

Recently, Khakpour *et al.* [97] and Hasegawa & Kasagi [48] compared the effect of clean and surfactant-contaminated surfaces on interfacial gas transfer using a numerical simulation for the transfer mechanism driven by surface-shear-induced turbulence. It was found that the presence of surfactants made the surface behave

like a solid wall. Khakpour *et al.* [97] also found that the transport of the surfactants at the surface did not depend on the actual surfactant Schmidt number. Shen*et al.* [1] investigated the effect of surfactants on free surface turbulent flow in the presence of mean surface shear by performing various DNS with Reynolds numbers $Re = 700$, 1000, and 1400, a Marangoni number of $Ma = 0.1$ and a Weber number of $We = 10$. They observed a noticeable reduction in the surface divergence even for very small levels of contamination. Herlina & Wissink [10] performed a series of DNS of interfacial gas transfer driven by isotropic turbulence diffusing from below. The severely contaminated surface was modelled by no-slip boundary conditions and contrasted to clean surface results [11], where K_L was found to scale with $Sc^{-1/2}$. The simulations were performed for a range of Schmidt numbers from $Sc = 2$ up to $Sc = 500$ and turbulence Reynolds numbers up to $Re_T = 865$. From the results, it was found that K_L scales with $Sc^{-2/3}$. For the smaller $Re_T < 500$ a modified large-eddy model ($K_L Sc^{2/3}/u_\infty \sim Re_T^{-1/2}$) was found to be valid, while for $Re_T > 500$ a modified small-eddy model ($K_L Sc^{2/3}/u_\infty \sim Re_T^{-1/4}$) was found to apply. This confirms that Theofanous' assumption [19] of a dual regime depending on the turbulent Reynolds number is also valid for a heavily contaminated surface.

2.4.3 Marangoni effect and surface elasticity

Marangoni effects are driven by surface tension gradients. In general, surface tension (σ) depends on the distribution of the surfactant contamination at the surface. Consequently, the Marangoni effect is generated by gradients of the surfactant concentration at the interface. Surfactant concentration gradients result in gradients of the surface tension. Surfactants thus indirectly produce forces at the interface. Their effects were detected by Marangoni (1871) and are commonly referred as Marangoni effect or forces. For example, when turbulence diffuses towards the surface from the bottom, the (initially uniform) surfactant concentration at the surface becomes non-uniform and upwelling motions will push surfactants to the sides where they ac-

cumulate. As a result, certain areas will become virtually surfactant-free while others will be quite heavily contaminated. This uneven surfactant distribution at the surface results in the generation of Marangoni forces that tend to damp the turbulent motion that initially caused this uneven surfactant distribution. This process typically leads to a significant reduction in the surface divergence.

Local variations in surfactant concentration generates variations in surface tension (which reduces with increasing surfactant concentration). As a result, the generated Marangoni forces will affect the near-surface (turbulent) flow. The interaction of surfactants and turbulent flows was investigated by Bernal *et al.* [109], Anthony *et al.* [110], Tsai & Yue [102], Willert & Gharib [111], Flack *et al.* [112] and Khakpour *et al.* [97].

At a fixed temperature, the surface tension (σ) is constant in the absence of surfactants. The surfactant concentration (γ) is related to the surface tension (σ) by

$$\sigma^* - 1 = Ma(1 - \gamma^*). \tag{2.25}$$

This linear approximation is given in [97] and [1]. The Marangoni number Ma is defined by $Ma = -\frac{\partial \sigma^*}{\partial \gamma^*}|_{\gamma^*=1}$ where

$$\left.\begin{aligned} \sigma^* &= \tfrac{\sigma}{\sigma_0} \\ \gamma^* &= \tfrac{\gamma}{\gamma_0} \end{aligned}\right\}, \tag{2.26}$$

and where the subscript zero refers to the equilibrium values of σ and γ. The surfactant concentration is normalised by dividing it by its equilibrium concentration in Eq. (2.26). This linearized approximation is only valid for small variations of $\gamma^* = \frac{\gamma}{\gamma_0} \approx 1$. The surface tension is a function of the surfactant contamination level such that $\frac{\partial \sigma^*}{\partial \gamma^*} < 0$. More information on the modelling of the Marangoni effects can be found in Chapter 3.

Chapter 3: METHODOLOGY

It is generally accepted that both laminar and turbulent incompressible flow of a Newtonian fluid is described by the Navier-Stokes equations, which consist of the continuity equation

$$\frac{\partial u_i}{\partial x_i} = \frac{\partial u_1}{\partial x_1} + \frac{\partial u_2}{\partial x_2} + \frac{\partial u_3}{\partial x_3} = 0, \tag{3.1}$$

and the scalar momentum equations

$$\frac{\partial u_i}{\partial t} + \frac{\partial (u_i u_j)}{\partial x_j} = -\frac{\partial P}{\partial x_i} + \nu \frac{\partial^2 u_i}{\partial x_j \partial x_j} \qquad i = (1, 2, 3), \tag{3.2}$$

where $(u_1, u_2, u_3) = (u, v, w)$ are the velocity components in the $(x_1, x_2, x_3) = (x, y, z)$ directions, t is time, $P = p/rho$ is the generalised pressure (the static pressure divided by the constant density) and ν is the kinematic viscosity. Summation, as illustrated in (3.1), is indicated by repeated indices. In the coordinate system employed here, x and y are in the horizontal directions, while z corresponds to the vertical direction. For convenience, the Navier-Stokes equations were non-dimensionalised using a characteristic length scale L and a characteristic velocity scale U, with ${x_i}^* = x_i/L$, ${u_i}^* = u_i/U$, $t^* = tU/L$, and $p^* = P/U^2$ and $(.^*)$ identifying non-dimensional quantities. The subsequent substitution of these rescaled variables in the momentum equations (3.2) gives

$$\frac{U^2}{L}\frac{\partial {u_i}^*}{\partial t^*} + \frac{U^2}{L}\frac{\partial ({u_i}^* {u_j}^*)}{\partial {x_j}^*} = -\frac{U^2}{L}\frac{\partial p^*}{\partial {x_i}^*} + \nu \frac{U}{L^2}\frac{\partial^2 {u_i}^*}{\partial {x_j}^* \partial {x_j}^*} \qquad i = (1, 2, 3), \tag{3.3}$$

By dividing both sides of (3.3) by $\frac{U^2}{L}$ we finally obtain the dimensionless Navier-Stokes equations

$$\frac{\partial {u_i}^*}{\partial t^*} + \frac{\partial ({u_i}^* {u_j}^*)}{\partial {x_j}^*} = -\frac{\partial p^*}{\partial {x_i}^*} + \frac{1}{Re}\frac{\partial^2 {u_i}^*}{\partial {x_j}^* \partial {x_j}^*} \qquad i = (1, 2, 3), \tag{3.4}$$

where

$$Re = \frac{UL}{\nu} \tag{3.5}$$

is the Reynolds number, which is a dimensionless quantity corresponding to the ratio of the inertial forces to the viscous forces. Generally, the larger the Reynolds number is the more important the inertial forces are and the more likely it is that the flow is turbulent.

The transport of a dissolved scalar concentration c in a fluid flow is described by the convection-diffusion equation

$$\frac{\partial c}{\partial t} + \nabla (c\vec{u}) = D\nabla^2 c \tag{3.6}$$

where

$$\nabla = \begin{pmatrix} \frac{\partial}{\partial x_1} \\ \frac{\partial}{\partial x_2} \\ \frac{\partial}{\partial x_3} \end{pmatrix}, \vec{u} = \begin{pmatrix} u_1 \\ u_2 \\ u_3 \end{pmatrix},$$

and D is the scalar diffusivity. Using Einstein's notation, with summation over repeated indices, (3.6) can be rewritten as

$$\frac{\partial c}{\partial t} + \frac{\partial c u_j}{\partial x_j} = D\frac{\partial^2 c}{\partial x_j \partial x_j} \qquad j = (1, 2, 3). \tag{3.7}$$

The scalar concentration c was subsequently non-dimensionalised by

$$c^* = \frac{c - c_{b,0}}{c_s - c_{b,0}}, \tag{3.8}$$

where c^* is the non-dimensional scalar concentration, c_s is saturation concentration at the surface and $c_{b,0}$ is the initial concentration in the bulk. Using L and U to non-dimensionalise t, x_j and u_j we obtain

$$\frac{\partial c^*}{\partial t^*} + \frac{\partial c^* u_j^*}{\partial x_j^*} = \frac{D}{UL}\frac{\partial^2 c^*}{\partial x_j^* \partial x_j^*} \qquad j = (1, 2, 3). \tag{3.9}$$

Note that $\frac{D}{UL} = \frac{D}{\nu}\frac{\nu}{UL} = \frac{1}{Sc\,Re}$, where $Sc = \frac{\nu}{D}$ is the Schmidt number, so that finally the non-dimensional scalar transport equation

$$\frac{\partial c^*}{\partial t^*} + \frac{\partial c^* u_j^*}{\partial x_j^*} = \frac{1}{ReSc}\frac{\partial^2 c^*}{\partial x_j^* \partial x_j^*} \qquad j = (1, 2, 3) \tag{3.10}$$

is obtained. In the remainder, the star notation will be dropped and non-dimensionality will be implicitly assumed. Convenient characteristic length and velocity scales applicable in the present simulations would be $U = 0.06\,\mathrm{m/s}$ and $L = 0.01\,\mathrm{m}$.

3.1 Modelling of surface contamination

The surface boundary condition for the velocity to be employed is affected by the level of contaminations and hence depends on the condition of the surface. For a clean surface, for instance, the free-slip boundary condition given by

$$\begin{cases} \frac{\partial u}{\partial z}\big|_{surface} = 0, \\ \frac{\partial v}{\partial z}\big|_{surface} = 0, \\ w|_{surface} = 0, \end{cases} \tag{3.11}$$

would be valid, while for a heavily contaminated surface the no-slip boundary condition with $u|_{surface} = v|_{surface} = w|_{surface} = 0$ would be a good approximation because it has the same scaling $K_L \propto Sc^{-2/3}$ of the transfer velocity K_L with the Schmidt number Sc. However, if the water surface is contaminated with surfactants the boundary condition will vary locally and instantaneously depending on the level of contamination. This dynamic boundary condition for the velocity was first modelled by Sheen (2004) [1]. According to this model, the stress balance is expressed by the dynamic boundary condition

$$\begin{cases} \frac{1}{Re}\,\frac{\partial u}{\partial z}\big|_{surface} = \frac{1}{We}\frac{\partial \sigma}{\partial x}, \\ \frac{1}{Re}\,\frac{\partial v}{\partial z}\big|_{surface} = \frac{1}{We}\frac{\partial \sigma}{\partial y}, \\ w|_{surface} = 0, \end{cases} \tag{3.12}$$

where We (the ratio of the inertial and surface tension forces) is the so-called Weber number, which is defined by $We = \frac{\rho U^2 L^2}{\sigma_0}$, where σ_0 is the characteristic surface tension. By assuming a linear relationship between the normalised surface tension, σ, and the normalised surfactant concentration, γ, we obtain $\sigma - 1 = Ma(1 - \gamma)$, with $Ma = \frac{\partial \sigma}{\partial \gamma}$ which is explained in detail in Section 2.4.3 The evolution of the

surfactant concentration (γ) at the water surface is given by the two-dimensional convection-diffusion equation

$$\frac{\partial \gamma}{\partial t} + \frac{\partial \gamma u_j}{\partial x_j} = \frac{1}{ReSc}\frac{\partial^2 \gamma}{\partial x_j \partial x_j} \qquad j = (1,2), \tag{3.13}$$

where γ is the dimensionless surfactant concentration, obtained by dividing the surfactant concentration by its equilibrium value γ_0, while x_j, u_j and t are made non-dimensional using L, U and L/U. In the simulations, the water surface was assumed to remain flat at all times (rigid lid assumption) and the total surfactant concentration

$$\langle \gamma \rangle = \int_{surface} \gamma dA$$

was assumed to be constant. Similarly to γ, also the surface tension was made dimensionless by dividing it by its equilibrium value σ_0. Based on the Sheen's model, the effect of surface contamination on the near surface velocity fluctuation is modeled by relating the normal gradient of the horizontal velocities at the surface to the horizontal gradients of the surfactant concentration. By taking the derivative of (2.25) and substituting this into (3.12), we obtain

$$\begin{cases} \frac{\partial \sigma}{\partial x} = -Ma\frac{\partial \gamma}{\partial x}, \\ \frac{\partial \sigma}{\partial y} = -Ma\frac{\partial \gamma}{\partial y}, \end{cases} \tag{3.14}$$

which when substituted in (3.14) gives the relations

$$\begin{cases} \frac{1}{Re}\left.\frac{\partial u}{\partial z}\right|_{surface} = -\frac{Ma}{We}\frac{\partial \gamma}{\partial x}, \\ \frac{1}{Re}\left.\frac{\partial v}{\partial z}\right|_{surface} = -\frac{Ma}{We}\frac{\partial \gamma}{\partial y}, \end{cases} \tag{3.15}$$

between the horizontal gradients of the surfactant concentration and the normal gradients of the horizontal velocity components at the surface. Note that if the ratio $Ma/We > 1$, the water surface is regarded to be highly contaminated [97]. Summarising, the model for the surface boundary conditions of the horizontal velocity reads

$$\left.\frac{\partial u_i}{\partial z}\right|_{surface} = -\frac{ReMa}{We}\frac{\partial \gamma}{\partial x_i}, \qquad i = (1,2). \tag{3.16}$$

In this equation, the nondimensional number ($ReMa/We$) determines the effect of the contamination level on the near surface velocity field.

3.1.1 Rescaling of (Re Ma/We)

As mentioned in the previous section, the Reynolds number represents the ratio of the intertial forces to the viscous forces, while the Weber number is the ratio of intertial forces to the surface tension forces. Hence, the ratio Re/We corresponds to the ratio of the surface tension forces to the viscous forces, thus corresponding to the inverse of the capillary number Ca. In the original context of open channel flow, the definition of the Weber number We uses the mean shear strength. In the present simulations, however, such a mean shear is absent and it would make sense to replace $ReMa/We$ in (3.16) by its equivalent Ma/Ca. Because the relevant characteristic scales are turbulent, it is better to use an alternative definition based on the turbulent length and velocity scales L_∞ and u_∞, respectively. As a result, a turbulent Weber number $We_T = \frac{2\rho {u_\infty}^2 L_\infty}{\sigma_0}$ is obtained. Similarly, the Reynolds number is replaced by a turbulent Reynolds number $Re_T = \frac{2\rho u_\infty L_\infty}{\mu}$, where μ is the dynamic viscosity, so that the ratio of turbulent Reynolds and Weber numbers becomes

$$\frac{Re_T}{We_T} = \frac{\sigma}{\mu u_\infty} = \frac{1}{Ca_T}, \tag{3.17}$$

where

$$Ca_T = \frac{\mu u_\infty}{\sigma} \tag{3.18}$$

is the turbulent capillary number.

3.2 Flow Solver

An in-house flow solver used in the present simulations has been extensively tested in the past, where it was used to study e.g. the growth and limiting behaviour of waves in Poisseuille flows [113], the effect of isotropic turbulence on interfacial mass transfer for various turbulent Reynolds numbers in [11]. The double diffusive instability driven occurring when an unstable salinity gradient is stabilised by a temperature gradient [114]. In the present simulations of isotropic turbulence induced air-water mass and heat transfer it is used to study the effect of insoluble surfactants and a finite-slip

boundary conditions on both the near surface flow field and the interfacial mass and heat transfer. The flow solver uses high-order discretisations of the incompressible Navier Stokes equations and the scalar convection-diffusion equation. The purpose of these discretisations is to replace the original differential equations by a (usually large) number of relatively simple equations that can be solved numerically. It is known that discretisations of the Navier-Stokes equation on a collocated mesh can cause a decoupling of the pressure and velocity fields. To avoid such a decoupling, for the present simulations the discretisation is performed using a Cartesian staggered mesh consisting of rectangular grid cells. The scalars (like pressure p, temperature T and concentration C) are defined in the middle of the cells, while the velocity is defined at the centre of the cell faces.

Below, first the discretisations used in the flow solver will be discussed in depth, followed by the discretisation used for the scalar transport equations and a detailed description of the way in which boundary conditions are implemented.

Note that the Kinetic energy Conserving Flow solver KCFlo code was parallelised for usage on large scale massively parallel computers. For this purpose the computational domain was divided into several blocks of equal size. Computations related to each block were carried out on separate, especially allocated processing cores. Communication between blocks (cores) was performed by using the standard Message Passing Interface (MPI) library.

3.2.1 Time integration

The discretisation method employed uses separate discretisations in space and time. Because the flow solver is incompressible, pressure waves travel at infinite speed. To deal with this, both the continuity equation (3.1) and the pressure term in (3.4) will need to be treated implicitly to ensure that the flow field remains divergence-free. The technique described here is based on the Marker and Cell method of Harlow and Welch [115]

First only the discretisation in time is considered and the continuity equation (3.1) is rewritten as

$$\left(\frac{\partial u_i}{\partial x_i}\right)^{(n+1)} = 0, \tag{3.19}$$

where the superscript $(n+1)$ denotes the number of time-steps δt that the simulation has progressed, i.e., $u(n \times \delta t) = u(t^{(n)}) = u^{(n)}$.

Next, the momentum equations are rewritten as

$$\left(\frac{\partial u_i}{\partial t}\right)^{(n+1/2)} = -\left(\frac{\partial p}{\partial x_i}\right)^{(n+1/2)} + \frac{3}{2}a_i^{(n)} - \frac{1}{2}a_i^{(n-1)} \qquad i = (1,2,3), \tag{3.20}$$

where $\frac{3}{2}a_i^{(n)} - \frac{1}{2}a_i^{(n-1)}$ is a second-order-accurate extrapolation of $a_i^{(n+1/2)}$ and the convective-diffusive contributions $a_1^{(n)} = a^{(n)}, a_2^{(n)} = b^{(n)}, a_3^{(n)} = c^{(n)}$ are defined by

$$a_i^{(n)} = -\left[\frac{\partial(u_i u_j)}{\partial x_j}\right]^{(n)} + \frac{1}{Re}\left(\frac{\partial^2 u_i}{\partial x_j \partial x_j}\right)^{(n)} \qquad i = (1,2,3). \tag{3.21}$$

By discretising (3.20) in time using the second-order-accurate central method

$$\left(\frac{\partial u_i}{\partial t}\right)^{(n+1/2)} = \frac{u_i^{(n+1)} - u_i^{(n)}}{\delta t}$$

centred about $t^{(n+1/2)}$, we subsequently obtain

$$u_i^{(n+1)} = u_i^{(n)} - \delta t\left(\frac{\partial p}{\partial x_i}\right)^{(n+1/2)} + \frac{\delta t}{2}\left[3a_i^{(n)} - a_i^{(n-1)}\right] \qquad i = (1,2,3), \tag{3.22}$$

where the contributions of the convective and diffusive terms to the new velocity field are treated according to the second-order accurate Adams-Bashforth method.

Finally, (3.22) is substituted in (3.19)

$$\left(\frac{\partial u_i}{\partial x_i}\right)^{(n)} - \delta t\left(\frac{\partial^2 p}{\partial x_i \partial x_i}\right)^{(n+1/2)} + \frac{\delta t}{2}\left[\frac{\partial\left(3a_i^{(n)} - a_i^{(n-1)}\right)}{\partial x_i}\right] = 0 \tag{3.23}$$

resulting in the so-called Poisson equation for the pressure

$$\left(\frac{\partial^2 p}{\partial x_i \partial x_i}\right)^{(n+1/2)} = \frac{1}{\delta t}\left(\frac{\partial u_i}{\partial x_i}\right)^{(n)} + \frac{1}{2}\left[\frac{\partial\left(3a_i^{(n)} - a_i^{(n-1)}\right)}{\partial x_i}\right] = 0. \tag{3.24}$$

All discretisations $\frac{\partial}{\partial x_i}$ in (3.24) are second-order accurate central. This Poisson equation is solved using the iterative conjugate gradient method with diagonal preconditioning. Once the pressure field $p^{(n+1/2)}$ is obtained, the new divergence-free velocity field $u_i^{(n+1)}$ is calculated from (3.22). For further discussions see Roche [116]

Note that the pressure and velocity fields are strongly coupled in this discretisation. As opposed to the a collocated mesh, where the discretisation of the second derivative of the pressure (for example on a uniform mesh with mesh size h in each direction), reads $\nabla^2 p_{i,j,k} = \frac{p_{i-2,j,k}-2p_{i,j,k}+p_{i+2,j,k}}{h^2} + \frac{p_{i,j-2,k}-2p_{i,j,k}+p_{i,j+2,k}}{h^2} + \frac{p_{i,j,k-2}-2p_{i,j,k}+p_{i,j,k+2}}{h^2}$, while for a staggered mesh it reads $\nabla^2 p_{i,j,k} = \frac{p_{i-1,j,k}-2p_{i,j,k}+p_{i+1,j,k}}{h^2} + \frac{p_{i,j-1,k}-2p_{i,j,k}+p_{i,j+1,k}}{h^2} + \frac{p_{i,j,k-1}-2p_{i,j,k}+p_{i,j,k+1}}{h^2}$. The latter expression provides a strong coupling between the pressures in all neighbouring grid cells and, hence, avoids the decoupling of pressure and velocity.

3.2.2 Discretisation of convective and diffusive terms

As mentioned in the previous section, the discretisations in time and space are carried out separately. The convective and diffusive terms in (3.22) are contained in $a_i^{(n)}$, which is defined in (3.21). For the convective terms $\left[\frac{\partial(u_i u_j)}{\partial x_j}\right]^{(n)}$, a fourth-order accurate kinetic energy conserving discretisation [114], [117], defined by e.g.

$$\left(\frac{\partial u^2}{\partial x}\right)_i = \frac{-u_{i+2}\left(\frac{u_i+u_{i+2}}{2}\right) + 8u_{i+1}\left(\frac{u_i+u_{i+1}}{2}\right) - 8u_{i-1}\left(\frac{u_i+u_{i-1}}{2}\right) + u_{i-2}\left(\frac{u_i+u_{i-2}}{2}\right)}{-x_{i+2} + 8x_{i+1} - 8x_{i-1} + x_{i-2}}, \tag{3.25}$$

is employed, where the subscript i denotes the x-location (x_i) of the coordinate at which the derivative is evaluated.

The second derivatives in the diffusive terms $\frac{1}{Re}\left(\frac{\partial^2 u_i}{\partial x_j \partial x_j}\right)^{(n)}$ are discretised using a fourth-order-accurate central discretisation

$$\left(\frac{\partial^2 u}{\partial x^2}\right)_i = \frac{u_{i+2} - 16u_{i+1} + 30u_i - 16u_{i-1} + u_{i-2}}{12(\delta x)^2}, \tag{3.26}$$

where δx is the size of grid cell in the uniform x-direction and the subscript i again indicates the x-location (x_i) where the respective variables are evaluated.

3.2.3 Discretisation of the scalar convection-diffusion equation

Extra care is needed when choosing methods for the discretisation of the scalar convection-diffusion equation (3.10). In the past, various methods were employed to resolve low-diffusivity scalar transport problems, for instance, Hasegawa and Kasagi [118] used a pseudo-spectral method to analyse interfacial mass transfer driven by wind-shear driven turbulence using a Schimidt number of Sc=100. Schwertfirm and Manhart [119], on the other hand, used second-order central differences for both fluid and scalar but employed a finer mesh for the discretisation of the scalar to calculate its mass transfer at a Schmidt number of $Sc = 49$.

While the scalar diffusion was calculated using the same fourth-order accurate central discretisation (3.26) as used in the flow solver, the very steep scalar gradients that occur instantaneously for very low scalar diffusivities make it necessary to employ a special numerical scheme for the convection that is capable of properly capturing such gradients without adding too much artificial scalar diffusion. Hence, it was decided to adapt a fifth-order accurate Weighted Essentially Non-Oscillatory (WENO) scheme known for its capability capturing shocks and steep gradients that may occur in various flow simulations. This WENO scheme was developed by Liu *et al.* [2] and adapted for the discretisation of scalar convection on a staggered mesh in [120]. The WENO scheme assembles mass fluxes by taking convex combinations of lower order polynomial interpolations in which the weights are determined by the local smoothness of the scalar distribution. In the neighbourhood of steep gradients, the local order of accuracy of the approximation is reduced in order to capture the gradient as well as possible. In the areas where the scalar distribution is smooth, the WENO scheme will reach its highest order of accuracy. By varying the way in which the weights are calculated, many variants of WENO schemes have been developed, for example [121], [2], [122], [123]. Compared to the original WENO scheme of [2], in the newer schemes, the calculation of the weights is optimised in order to increase the local accuracy in the presence of steep gradients. An increase in local accuracy in

areas where the scalar distribution is smooth was achieved by increasing the size of stencil [122]. Henrick *et al.* [123] showed that when using weights generated by the classical smoothness indicator of [121], the maximum order of accuracy of the WENO scheme could not be recovered. To overcome this problem the Mapped Weighted Essentially Non-Oscillatory WENOM method was developed, which was able to produce accurate results close to discontinuities (steep gradients or shocks). Borges *et al.* [3] developed the fifth-order accurate WENO-Z (W5-Z) scheme as an improvement to the WENO-5 (W5) scheme of Jiang [121] by creating a new smoothness indicator.

In [120] it was shown that for scalar transport calculations on relatively coarse staggered meshes the original fifth-order-accurate WENO scheme of [2], compared to the variant introduced in [121], gave slightly better results. As a result, the original W5 scheme [2] was adopted for the calculation of scalar transport equation (3.10) in the in-house flow solver. The workings of the scheme is illustrated below for the one-dimensional scalar surfactant convection problem described by

$$\frac{\partial \gamma}{\partial t} = -\frac{\partial \gamma u}{\partial x}, \tag{3.27}$$

where the surfactant concentration is located in the middle of the cell and the velocity is defined at the borders of each cell (see Figure 3.1). Like the velocity, also the mass

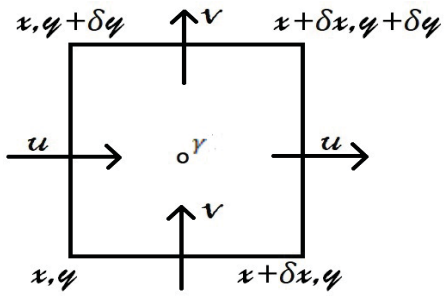

Fig. 3.1. Grid cell

flux (γu) of the surfactant is calculated at borders between cells and the increase in the surfactant concentration inside the grid cell over a time interval δt is given by

$$[\gamma|_{t+\delta t} - \gamma|_t]\,\delta x = [(\gamma u)|_x - (\gamma u)|_{x+\delta x}]\,\delta t. \tag{3.28}$$

The surfactant concentration $R_i(x)$ at the border x of two adjacent grid cells is calculated by

$$R_i(x) = \frac{a_0}{a_0 + a_1 + a_2} P_{i-1}(x) + \frac{a_1}{a_0 + a_1 + a_2} P_i(x) + \frac{a_2}{a_0 + a_1 + a_2} P_{i+1}(x), \quad (3.29)$$

where $\frac{a_k}{a_0+a_1+a_2}$ for $k = 0, 1, 2$ are the normalised weights defined further below and $P_i(x)$ is a third-order-accurate polynomial interpolation of the surfactant concentration γ defined by

$$\begin{aligned} P_i(x) = \; & \tfrac{(x-x_i)(x-x_{i+1})}{(x_{i-1}-x_i)(x_{i-1}-x_i)}\gamma_{i-1} + \tfrac{(x-x_{i-1})(x-x_{i+1})}{(x_i-x_{i-1})(x_i-x_{i+1})}\gamma_i + \tfrac{(x-x_{i-1})(x-x_i)}{(x_{i+1}-x_{i-1})(x_{i+1}-x_i)}\gamma_{i+1} \\ & - \tfrac{(x_i-x_{i-1})\gamma_{i+1} - (x_{i+1}-x_{i-1})\gamma_i + (x_{i+1}-x_i)\gamma_{i-1}}{12(x_{i+1}-x_{i-1})} \end{aligned} \quad (3.30)$$

Depending on the direction of the flow, the scalar concentration is defined using either R_i^+ or R_i^-, which are related to R_i by

$$\begin{cases} R_i^+ = R_i(x_{i+\frac{1}{2}}), \\ R_i^- = R_i(x_{i-\frac{1}{2}}). \end{cases} \quad (3.31)$$

The normalised flux $(\gamma u)_{i-\frac{1}{2}}$ at $x_{i-\frac{1}{2}}$ is subsequently defined by

$$(\gamma u)_{i-\frac{1}{2}} = \begin{cases} u_{i-\frac{1}{2}} R_{i-1}^+ & \text{if } u_{i-\frac{1}{2}} \geq 0, \\ u_{i-\frac{1}{2}} R_i^- & \text{if } u_{i-\frac{1}{2}} < 0, \end{cases} \quad (3.32)$$

while the normalised flux $(\gamma u)_{i+\frac{1}{2}}$ at $x_{i+\frac{1}{2}}$ is determined by

$$(\gamma u)_{i+\frac{1}{2}} = \begin{cases} u_{i+\frac{1}{2}} R_i^+ & \text{if } u_{i+\frac{1}{2}} \geq 0, \\ u_{i+\frac{1}{2}} R_{i+1}^- & \text{if } u_{i+\frac{1}{2}} < 0. \end{cases} \quad (3.33)$$

Both (3.32) and (3.33) are then used to calculate the scalar convection

$$L_i(\gamma) = -\frac{(\gamma u)_{i+\frac{1}{2}} - (\gamma u)_{i-\frac{1}{2}}}{x_{i+\frac{1}{2}} - x_{i-\frac{1}{2}}}. \quad (3.34)$$

As mentioned above, the fifth-order WENO scheme variants basically use a combination of three quadratic polynomial interpolations, see Eq. (3.30). The weights a_k

$(k = 0, 1, 2)$ depend on the smoothness of the local interpolating polynomial and are defined by

$$a_k = \begin{cases} d_k & \text{for C5} \\ d_k \left(\frac{1}{(\varepsilon + IS_k)^3} \right) & \text{for W5} \\ d_k \left(1 + \frac{\tau}{(\varepsilon + \beta_k)} \right) & \text{for W5-Z} \end{cases} \qquad k = 0, 1, 2, \tag{3.35}$$

where $d_0 = \frac{1}{10}$, $d_1 = \frac{6}{10}$ and $d_2 = \frac{3}{10}$ for R^+ and $d_0 = \frac{3}{10}$, $d_1 = \frac{6}{10}$ and $d_2 = \frac{1}{10}$ for R^-, $\varepsilon > 0$ is a small number ($\varepsilon \sim 10^{-6}$), $\tau = \mid \beta_0 - \beta_2 \mid$ and IS_k, β_k $(k = 0, 1, 2)$ are smoothness indicators for W5 and W5-Z, respectively, defined by

$$\begin{cases} IS_0 = \frac{1}{2}((\gamma_{i-1} - \gamma_{i-2})^2 + (\gamma_i - \gamma_{i-1})^2 + (\gamma_i - 2\gamma_{i-1} + \gamma_{i-2})^2, \\ IS_1 = \frac{1}{2}((\gamma_i - \gamma_{i-1})^2 + (\gamma_{i+1} - \gamma_i)^2) + (\gamma_{i+1} - 2\gamma_i + \gamma_{i-1})^2, \\ IS_2 = \frac{1}{2}((\gamma_{i+1} - \gamma_i)^2 + (\gamma_{i+2} - \gamma_{i+1})^2) + (\gamma_{i+2} - 2\gamma_{i+1} + \gamma_i)^2. \end{cases} \tag{3.36}$$

and

$$\begin{cases} \beta_0 = \frac{13}{12}(\gamma_{i-2} - 2\gamma_{i-1} + \gamma_i)^2 + \frac{1}{4}(\gamma_{i-2} - 4\gamma_{i-1} + 3\gamma_i)^2, \\ \beta_1 = \frac{13}{12}(\gamma_{i-1} - 2\gamma i + \gamma_{i+1})^2 + \frac{1}{4}(\gamma_{i-1} - \gamma_{i+1})^2, \\ \beta_2 = \frac{13}{12}(\gamma_i - 2\gamma_{i+1} + \gamma_{i+2})^2 + \frac{1}{4}(3\gamma_i - 4\gamma_{i+1} + \gamma_{i+2})^2. \end{cases} \tag{3.37}$$

Apart from the fifth-order WENO schemes W5 and W5-Z, in Eq. (3.35) also the weights for the fifth order upwind central scheme C5 were added. The latter scheme is obtained when the weights $a_0 = d_0, a_1 = d_1, a_2 = d_2$ are made independent of the smoothness of the scalar distribution.

The time integration of the convection-diffusion equation is finally carried out by employing the Total Variation Diminishing (TVD) third-order Runge-Kutta method of [124]. At the start the scalar concentration $\gamma^{(n)}$ at time $t = t^{(n)}$ is copied to γ_0, then the following sequence of steps is carried out

$$\gamma_1 = \gamma_0 + \delta t L_0(i) \tag{3.38}$$

$$\gamma_2 = \frac{3}{4}\gamma_0 + \frac{1}{4}\gamma_1 + \frac{1}{4}\delta t L_1(i) \tag{3.39}$$

until finally in the third step the scalar concentration

$$\gamma^{(n+1)} = \frac{1}{3}\gamma_0 + \frac{2}{3}\gamma_2 + \frac{2}{3}\delta t L_2(i) \tag{3.40}$$

at $t = t^{(n+1)}$ is obtained.

3.3 An Overview of Computational Approaches

3.3.1 Direct Numerical Simulation (DNS)

"Direct Numerical Simulation" (DNS) is the most accurate computational tool to simulate flow problems. DNS involves solving the Navier–Stokes equations by resolving all scales of flow motion explicitly, including the smallest relevant scales (the so-called Kolomogorov scales) so there is no need to use a model that accounts of unresolved turbulent motions [125], [126], [127], [128]. As turbulence is a proper solution to the Navier-Stokes equations, DNS can in principle be used to simulate any kind of turbulent flow. It allows for a detailed study of instantaneous flow patterns, mechanisms for the transition to turbulence, the effects of turbulence in heat and mass transfer problems etc. DNS results are fully defined by the boundary and initial conditions that are applied. In the present work, we use periodic boundary conditions in the horizontal directions in an attempt to represent the much larger extent of the physical domain in a relatively small computational domain. The turbulence generated in the LES is initially seeded by a random 2D field and then allowed to develop for about 300 time-units until a fully developed (statistically steady) turbulent flow field is obtained and the actual initial conditions used are no longer relevant.

In a DNS, the nonlinear Navier-Stokes equations (i.e. the convective terms are nonlinear) are discretised and replaced by a set of linear algebraic equations that can be solved computationally. Usually, to save computational effort, higher-order discretisations are employed that need fewer nodes to achieve a good accuracy. For each of the three spatial directions, the increase in computational effort with in-

creasing macroscale Reynolds number Re scales with $Re^{3/4}$, where Re is defined in (3.5). For all three spatial dimensions together this results in a computational effort scaling with $Re^{9/4}$. For explicit time-integration methods, like the third-order Runge-Kutta method used for the integration of the scalars and the second-order Adams-Bashforth method used for the integration of the Navier-Stokes equations, the size of the timestep scales with the size of the smallest spatial step in either the x, y or z direction. Hence, in three dimensions the total computational effort using such an explicit time-integration method scales with Re^3. When using implicit time-integration, the Kolmogorov timescale is the limiting factor and the total computational cost for a 3D calculation would be reduced to $Re^{11/4}$. Because of the huge computational effort, for many engineering problems DNS is far too expensive. To calculate the flow using DNS, usually large, massively parallel super computers are required and even then there is a severe restriction regarding the magnitude of the Reynolds number and/or the complexity of the computational domain.

3.3.2 Large Eddy Simulation (LES)

A Large-Eddy Simulations (LES) is a numerical approach that is less computationally demanding than a DNS. Only the larger scale of motion are resolved, while the smaller ones (the subfilter or subgrid scales) are modelled, usually with a simple eddy viscosity model. The cut off length-scale is somewhere in the inertial range. This is the range in a turbulent energy spectrum where the kinetic energy is approximately conserved. Usually, in LES the computational mesh is used as an implicit filter. The subgrid scales are assumed to be isotropic which would make them relatively easy to model. The main purpose of the model is to remove excess kinetic energy from the flow, which would normally be dissipated at the smallest scales (which are not resolved in LES calculations). Some LES models allow for backscatter of kinetic energy from subgrid scales to larger scales. In the present simulations, however, only isotropic turbulence is simulated with LES which is something that can be done quite

accurately by using the purely dissipative traditional Smagorinsky model described below, using a Smagorinsky constant of $C_{Smag} = 0.22$. The isotropic turbulence itself is generated in a cubic box with periodic boundary conditions. The spatial discretisation as well as the time-intergration are performed using the same methods as in the DNS. The only difference is the addition of a dissipative term (LES model) to the Navier-Stokes equations. The turbulent kinetic energy of the isotropic turbulence in the periodic box is defined by

$$k = \frac{1}{2}\left(\langle u'u'\rangle_3 + \langle v'v'\rangle_3 + \langle w'w'\rangle_3\right) = \frac{3}{2}\langle u'u'\rangle_3, \tag{3.41}$$

while the turbulence level is defined by

$$Tu = \sqrt{\frac{1}{3}(\langle u'u'\rangle_3 + \langle v'v'\rangle_3 + \langle w'w'\rangle_3)} = \sqrt{\frac{2}{3}k}, \tag{3.42}$$

where $\langle\cdot\rangle_3$ represents averaging in the three homogeneous directions.

When allowed to freely develop without the addition of energy, (isotropic) turbulence tends to decay because of the transfer of kinetic energy (effectively) from larger to smaller and smaller scales until it reaches the dissipative scales where it is transformed into heat [44]. To avoid the isotropic turbulence to decay and/or become anisotropic, every time step the fluctuations are rescaled such that k is conserved and $\langle u'u'\rangle_3 = \langle v'v'\rangle_3 = \langle w'w'\rangle_3$.

The reason for using LES to calculate the isotropic turbulence that is used as an instantaneous boundary condition at the bottom of the computational domain is to save computing time. It is expected (and later verified) that the missing small scales in the isotropic turbulence, once introduced in the DNS domain, are quickly re-established. Note that the numerical scheme employed to discretise the convective terms in the Navier-Stokes equations is unconditionally kinetic energy conserving and, hence, there is no numerical dissipation. Also, the spatial and temporal resolution used om the DNS was very fine in order to avoid having to use large refinement factors to resolve the high Schmidt number scalars.

Note that generally in LES, it is usually assumed that small scales of motion are independent of the computational geometry and can usually be ignored (i.e. replaced

by a simple dissipative model). However, there are situations where the the geometry does affect small scales. This is the case in boundary layer flows, where small scales motions become important and need to be modelled. A more detailed description of various modelling options is outside the scope of this thesis. More detailed information on modelling can be found in e.g. Sagaut [129].

3.3.3 The Smagorinsky model

The Smagorinsky model, proposed by Smagorinsky in (1963) [130], is the traditional subgrid scale model and still widely used. It is basically a simple eddy-viscosity model that calculates the eddy viscosity ν_T based on the resolved scales. To calculate the eddy viscosity, a length scale and a velocity scale are needed. Usually the grid size Δ is used as the length scale while the velocity scale is given by $\Delta\|S\|$, where

$$S_{ij} = \frac{1}{2}\left(\frac{\partial u_i}{\partial x_j} + \frac{\partial u_j}{\partial x_i}\right), \tag{3.43}$$

is the (filtered) strain rate tensor, where u_i for $i = 1, 2, 3$ are the resolved velocities, and

$$\|S\| = \sqrt{2\langle S_{ij}S_{ij}\rangle_3} \tag{3.44}$$

is the magnitude of the rate-of-strain tensor S_{ij}. The Smagorinsky constant is used to pre-multiply the length-scale Δ so that the eddy viscosity is given by

$$\nu_T = (C_s\Delta)^2\|S\|. \tag{3.45}$$

The total viscosity in the Navier-Stokes equations is then determined by the sum of the kinematic viscosity and the eddy viscosity.

Note that the standard Smagorinsky model works very well for isotropic turbulence simulations with periodic boundary conditions. In the presence of real boundaries, however, it generated too much eddy-viscosity because of the presence of laminar shear. To resolve this, the value of C_S needs to be reduced from 0.22 to around 0.065, which can be done, for instance, by applying "van Driest damping" [131].

3.3.3.1 Isotropic turbulence

In experiments, isotropic turbulent flow is typically generated by imposing artificial oscillating forces, for instance induced by an oscillating grid in a volume of fluid. By maintaining the amplitude and frequency of the oscillation, the turbulence becomes statistically steady. This means that the level of fluctuations (or turbulent kinetic energy) becomes close to constant in time. In experiments it is very difficult to achieve such turbulence as it requires a zero mean flow and zero mean shear at all locations. Note that this does not imply that there is no instantaneous shear.

Studies involving isotropic turbulent flows were performed by various researchers, such as e.g. [132], [10], [133]

3.3.4 Summary of the Computational Work

The flow solver KCFlo is an in-house developed code which combines an incompressible Navier-Stokes solver (with a fourth-order accurate kinetic energy conserving discretisation of the convective terms) with a special solver for the scalar convection-diffusion equation that employs a fifth-order accurate WENO scheme for scalar convection and a fourth-order accurate central discretisation for scalar diffusion. KCFlo allows the usage of a dual mesh, where the scalar is solved on a finer mesh than the flow. When needed to generate a turbulent boundary condition at the bottom of the domain, KCFlo runs a separate large-eddy simulation of isotropic turbulence in a periodic box in parallel with the main DNS.

It is known that an extremely fine grid resolution is needed to capture the dynamics of the turbulent mass transfer at high Schmidt numbers [134]. The grid spacing used in the upper part of the computational domain in all simulations is such that it fulfils the so-called "Grötzbach criterion" [134]. This criterion is fulfilled as the vertical grid resolution near the interface Δz has at least 7 points within the Batchelor sublayer of size L_B (also referred to as the Batchelor scale) and the geometric mean of the grid cells ($\overline{\Delta} = (\Delta x \times \Delta y \times \Delta z)^{1/3}$) $\leq \pi L_B$ in the upper part of the computational

domain, a detailed grid refinement study, including the most challenging case with a free-slip boundary condition at the surface as used here in Chapters 5 and 6, was presented in [11].

Recently, KCFlo was extended by a 2D solver for surfactant transport at the air-water interface. The convection-diffusion equation for the surfactant is solved every time step on separate computing cores using an adapted 2D version of the scalar solver that is implemented in the DNS, in which the WENO-Z scheme replaces the classical WENO-5 discretisation, which (as shown earlier in this chapter) provides the same accuracy as the WENO-5 scheme using only half the number of grid points in each direction. In summary, the following solvers were combined in KCFlo to perform the surfactant simulations:

1. 2D solver for the surfactant transport equation at the surface (using a fifth-order-accurate WENO-Z scheme).

2. 3D DNS flow solver.

3. Up to five 3D DNS transport equations for the scalar transport (using the fifth-order-accurate WENO-5 scheme).

4. 3D LES flow solver to generate isotropic turbulence using the Smagorinsky model.

Simulation	*Domain*	*Mesh*	Δ_t
$2D$ DNS (surfactant)	$5L \times 5L$	128×128	$300L/U$
$3D$ DNS (dissolved scalar)	$5L \times 5L \times 3L$	up to $256 \times 256 \times 424$	$300L/U$
$3D$ DNS	$5L \times 5L \times 3L$	$128 \times 128 \times 212$	$300L/U$
LES	$5L \times 5L \times 5L$	$64 \times 64 \times 64$	$300L/U$

Table 3.1
Overview of the computations

An overview of the simulations is provided in Table **??** and the implementation of the top boundary condition is explained in Section 3.4. Figure 3.2 shows a cross section at $y/L = 2.5$ through the 3D DNS mesh as used in some visualisations shown in Chapters 5 and 6. It can be seen that a uniform mesh is employed in the x direction

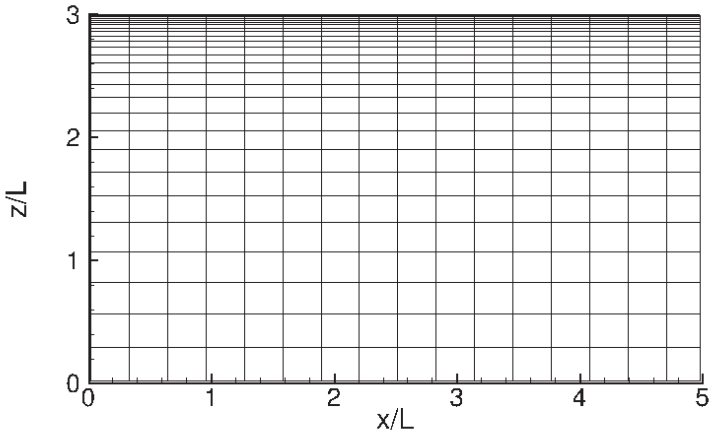

Fig. 3.2. Cross section of computational domain at $y = 2.5$, showing every 8^{th} grid line

(as well as in the y-direction), while the mesh in the z-direction is stretched such that the very thin concentration boundary layer at the surface becomes sufficiently well resolved.

3.4 Implementation of Top Boundary Condition

There are three concurrently running solvers used in each simulation, which are the 3D DNS (flow solver including up to five scalar transport equations for the dissolved gas using the W5 scheme for the convection), the 3D LES (flow solver) and a 2D DNS to simulate the surfactant transport at the surface using the W5-Z scheme for the scalar convection.

As mentioned earlier, the flow field in the LES calculations was initialised by using a random velocity field. After allowing this field to develop for 300 time-units, the DNS was started. Every time step, a turbulent flow field from a horizontal cross section of the LES was introduced as boundary condition at the bottom of 3D DNS. After the turbulent flow in the DNS became fully developed, the actual surfactant calculations were started. THE DNS solver and the surfactant solver were coupled by transferring every time step the latest horizontal velocity field from the top of DNS to the surfactant solver, where it was used to calculate the scalar convection of the surfactant. The newly calculated surfactants concentration was subsequently copied back to the DNS where it was used to set the correct top boundary condition for the horizontal velocities u and v in order to proceed the DNS calculation for another time-step.

Khakpour *e*t al. [97] showed that the actual Schmidt number Sc of the surfactant has negligible effect on the evolution of the surfactant distribution. Because of this the surfactants can be calculated on the same mesh as the fluid and a mesh refinement because of a possible low diffusivity of the surfactant is not required. We were able to confirm the above independence of the surfactant distribution on Sc (as mentioned previously by [97]) and decided to use $Sc_s = 2$ in all our simulations. The surfactant itself was initialised using its equilibrium value of $\gamma = 1$ at the entire surface. As mentioned earlier in Chapter 3.1, the model used to implement the surface boundary conditions for the horizontal velocities relates the horizontal gradients of the surfactant concentration with the normal gradients of the horizontal velocities. see also Figure 3.1.

To determine the velocity field at the surface $\left(u^{(n)}_{i+\frac{1}{2},j,mxz+\frac{1}{2}}, v^{(n)}_{i,j+\frac{1}{2},mxz+\frac{1}{2}}\right)$, the horizontal velocity field located at the grid plane immediately below the surface $\left(u^{(n)}_{i+\frac{1}{2},j,mxz}, v^{(n)}_{i,j+\frac{1}{2},mxz}\right)$ and the surfactant concentration gradients $\gamma^{(n)}$ were used. To

explain this, we first write the model in discretised form, using the superscript (n) to denote the n-th time-step,

$$\begin{aligned}
\frac{u^{(n)}_{i+\frac{1}{2},j,mxz+\frac{1}{2}} - u^{(n)}_{i+\frac{1}{2},j,mxz}}{z_{mxz+\frac{1}{2}} - z_{mxz}} &= -\frac{Ma}{Ca}\frac{\gamma^{(n)}_{i+1,j} - \gamma^{(n)}_{i,j}}{\Delta x}, \\
\frac{v^{(n)}_{i,j+\frac{1}{2},mxz+\frac{1}{2}} - v^{(n)}_{i,j+\frac{1}{2},mxz}}{z_{mxz+\frac{1}{2}} - z_{mxz}} &= -\frac{Ma}{Ca}\frac{\gamma^{(n)}_{i,j+1} - \gamma^{(n)}_{i,j}}{\Delta y},
\end{aligned} \tag{3.46}$$

where the subscripts i, j, k denote the location (x_i, y_j, z_k) of the respective velocity components.

The velocity field at the surface, $\left(u^{(n+1)}_{i+\frac{1}{2},j,mxz+\frac{1}{2}}, v^{(n+1)}_{i,j+\frac{1}{2},mxz+\frac{1}{2}}\right)$, used in the WENO-Z calculation to obtain the surfactant distribution at the new time step $t^{(n+1)}$, is estimated by

$$\begin{aligned}
u^{(n+1)}_{i+\frac{1}{2},j,mxz+\frac{1}{2}} &\approx u^{(n)}_{i+\frac{1}{2},j,mxz} - \frac{Ma}{Ca}\frac{\gamma^{(n)}_{i+1,j} - \gamma^{(n)}_{i,j}}{x_{i+1} - x_i}\left(z_{i,j,mxz+\frac{1}{2}} - z_{mxz}\right), \\
v^{(n+1)}_{i,j+\frac{1}{2},mxz+\frac{1}{2}} &\approx v^{(n)}_{i,j+\frac{1}{2},mxz} - \frac{Ma}{Ca}\frac{\gamma^{(n)}_{i,j+1} - \gamma^{(n)}_{i,j}}{y_{i+1} - y_i}\left(z_{i,j,mxz+\frac{1}{2}} - z_{mxz}\right),
\end{aligned} \tag{3.47}$$

and subsequently used in the convection-diffusion equation of the surfactant to evaluate the surfactant concentration for the new time step $t^{(n+1)}$ in the convection-diffusion Eq. (3.13) for the surfactant calculation, the time integration of the convection-diffusion equation was performed using a third-order Runge-Kutta method as given in Section 3.2.3.

The surfactant distribution obtained at the latest time step, is transferred to the $3D\ DNS$ to determine the surface boundary conditions for the horizontal velocities, which are implemented by changing the velocity in the ghost cells outside of the computational domain. By using ghost cells there is no need to change the numerical stencils near the boundaries.

Figure 3.3 shows a flow chart to explain the sequence of the calculations that are carried out in the simulation. The right-hand-side of Figure 3.3 shows the calculations related to the surfactant and the left-hand-side shows the calculations performed in the 3D DNS flow which is updated based on the new boundary condition.

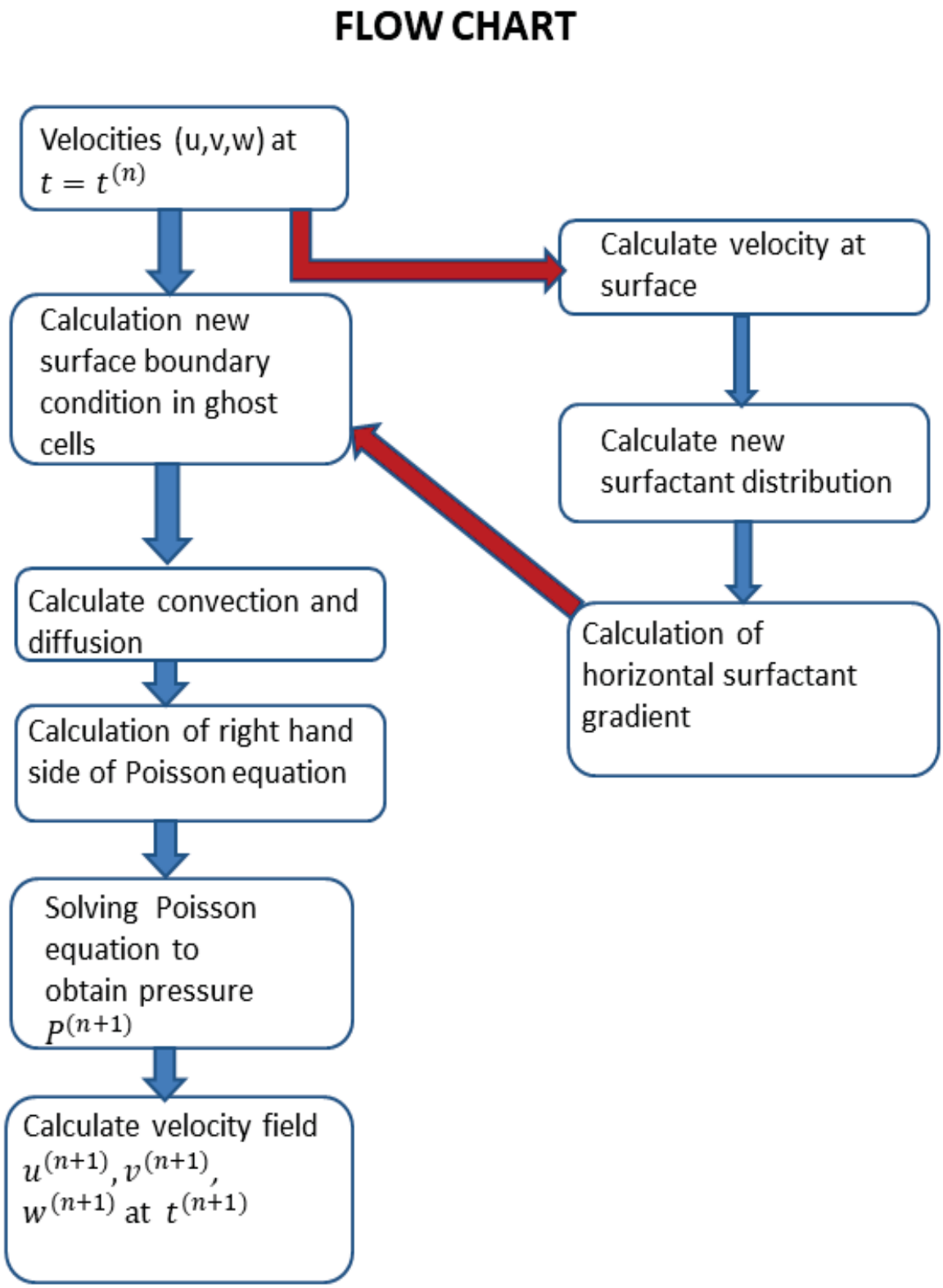

Fig. 3.3. Schematic illustration of flow wok process

Chapter 4: Comparison of WENO schemes

4.1 Introduction

In both laboratory and nature water surfaces are often contaminated by various substances which adversely affects interfacial mass transfer. Hence, identifying the correct boundary conditions at the air-water interface is a crucial step in order to obtain accurate simulation results. An important source of contamination are surfactants which locally reduce the surface tension therefore inducing Marangoni forces. To properly model the effects of surfactant contamination it is needed to accurately calculate changes in the surfactant concentration at the free surface. This can be done by solving the two-dimensional (2D) convection-diffusion Eq. (3.13). Convection is responsible for the transport of the surfactant by fluid flow, while diffusion models the spreading of the surfactant owing to molecular motion. The main aim here was to determine which of the two WENO schemes (W5 or W5-Z) will produce the most accurate results on a relatively coarse uniform mesh.

4.2 Verification of the order of accuracy

To facilitate the comparison of the results obtained on the staggered mesh, as explained below the number of grid points in each refinement step is increased by a factor of 3. Consequently, for the grid-refinement study a sequence of grid points 10,

30, 90 and 270 was used. Using this strategy the locations where γ is defined on the coarsest mesh will overlap with locations on the refined meshes.

At the beginning of the comparison, one of the main focuses will be on the order of accuracy that can be achieved. As mentioned earlier, if the distribution of the scalar γ is sufficiently smooth a fifth-order of accuracy should be obtained. One of the parameters used in the calculation of the weights for the WENO schemes in (3.35) is ε. Theoretically, after one time-unit for each simulation the calculated scalar distribution should perfectly overlap with its initial distribution (at time zero). This property makes it easy to calculate the error in the next part and also to study the spatial order of accuracy for both the W5 and W5-Z. Note that the time-step has to be chosen sufficiently small (se below) so that the numerical error is dominated by the spatial discretisation. The transport of the surfactant is represented by the convection-diffusion Eq. (3.13). In the in-house flow solver the fifth-order accurate Weighted Essentially Non-Oscillatory WENO scheme (W5) of Liu et al. [2] is employed to discretise scalar convection. In order to assess the accuracy of the implementation, the diffusion term in (3.13) is ignored so that

$$\frac{\partial \gamma}{\partial t} = -\frac{\partial \gamma u_j}{\partial x_j} \tag{4.1}$$

was obtained. For a detailed overview of the discretisations used here see Chapter 3. To begin with the implementation of W5-Z scheme for the discretisation of (4.1) was verified by setting the surfactant concentration γ equal to one, combined with velocities (i) $u = 1$ and (ii) $u = -1$. The results confirmed that in both cases the distribution of the surfactant concentration remained the same for all time. In all tests the time step (δ_t) was chosen to be sufficiently small ($\delta_t \sim 0.0002$) to make sure that the time-integration error was at least an order of magnitude smaller than the smallest spatial error. A separate time step study was not performed as in all simulations reported the time-step was chosen small enough for the spatial error to fully dominate.

4.2.1 One dimensional test problem

A 1D test problem was selected in order to assess the accuracy of the WENO discretisations, W5 and W5-Z in space using a wave moving with constant velocity either to the right ($u = 1$) or to the left ($u = -1$). By varying the number of grid points, the order of accuracy of the W5 and W5-Z implementations was assessed.

In the test problem, the initial surfactant concentration on the periodic interval $0 \leq x \leq 1$ was defined by

$$\gamma_0 = (1 + \sin(2\pi x))/2, \tag{4.2}$$

while the velocity was held constant ($u = 1$ and $u = -1$). A uniform staggered mesh was employed comprising 10, 30, 90, and 270 grid points.

4.2.2 Results

Four different grids were considered in the $1D$ test cases used to compare the order of accuracy of the W5 and W5-Z implementations. Four different values for the parameter ε in (3.35) were used ($\varepsilon = 10^{-2}, \varepsilon = 10^{-4}, \varepsilon = 10^{-6}, 10^{-8}, 10^{-12}, \varepsilon = 10^{-16}$, $\varepsilon = 1.0$ and $\varepsilon = 100$). The absolute error, calculated at the location $x_0 = 0.25$, is given by

$$E = \mid \gamma_T(x_0) - \gamma_0(x_0) \mid, \tag{4.3}$$

where T corresponds to one flow-through-time (1 time-unit), while the initial condition, γ_0, is defined in (4.2).

Tables 4.1 and 4.2 show the effect of the parameter ε, used in (4.3) to obtain the weights for the WENO5 and WENO-Z schemes, on the error obtained when approximating the convection of the function defined in (4.2). It can be seen that for for small ε in both cases (W5 and W5-Z) the error $E(N)$ is virtually independent of ε. In the W5-Z case, also for larger values of ε the error hardly changes. In contrast, the error in the W5 approximation changes significantly. For $N \geq 30$ at first the error E grows, then reaches a maximum near $\varepsilon = 10^{-6}$ and subsequently decreases

	$E(N)$			
ε	N=10	N=30	N=90	N=270
10^{-16}	8.07×10^{-3}	2.87×10^{-4}	6.47×10^{-6}	1.29×10^{-7}
10^{-12}	8.07×10^{-3}	2.87×10^{-4}	6.47×10^{-6}	1.29×10^{-7}
10^{-8}	8.07×10^{-3}	2.87×10^{-4}	6.47×10^{-6}	1.35×10^{-7}
10^{-6}	8.07×10^{-3}	2.88×10^{-4}	6.81×10^{-6}	3.28×10^{-7}
10^{-4}	8.07×10^{-3}	3.03×10^{-4}	1.12×10^{-5}	1.21×10^{-8}
10^{-2}	8.23×10^{-3}	2.92×10^{-4}	3.29×10^{-7}	9.78×10^{-10}
1.0	5.18×10^{-3}	2.54×10^{-5}	8.97×10^{-8}	8.66×10^{-10}
100.0	4.63×10^{-3}	2.09×10^{-5}	8.73×10^{-8}	8.65×10^{-10}

Table 4.1
Errors in W5 obtained using various values of ε

and appears to become independent of ε for $\varepsilon \to \infty$. Generally, errors in the W5-Z

	$E(N)$			
ε	N=10	N=30	N=90	N=270
10^{-16}	5.02×10^{-3}	2.06×10^{-5}	8.74×10^{-8}	8.65×10^{-10}
10^{-12}	5.02×10^{-3}	2.06×10^{-5}	8.74×10^{-8}	8.65×10^{-10}
10^{-8}	5.02×10^{-3}	2.06×10^{-5}	8.74×10^{-8}	8.65×10^{-10}
10^{-6}	5.02×10^{-3}	2.06×10^{-5}	8.74×10^{-8}	8.65×10^{-10}
10^{-4}	5.03×10^{-3}	2.08×10^{-5}	8.72×10^{-8}	8.65×10^{-10}
10^{-2}	5.07×10^{-3}	2.09×10^{-5}	8.72×10^{-8}	8.65×10^{-10}
1.0	4.63×10^{-3}	2.09×10^{-5}	8.72×10^{-8}	8.65×10^{-10}
100.0	4.62×10^{-3}	2.08×10^{-5}	8.72×10^{-8}	8.65×10^{-10}

Table 4.2
Errors in W5-Z obtained using various values of ε

approximation appear to be smaller than in the W5 approximation.

	N=10	N=30	N=90	N=270
$E(N)$	5.02×10^{-3}	2.06×10^{-5}	8.74×10^{-8}	8.65×10^{-10}

Table 4.3
Errors in C5

The upwind central scheme does not depend of ε. The errors obtained when approximating the convection of (4.2) are shown in Table 4.3. It can be seen that for all N the magnitude of the errors are compatible with the errors produced in the W5-Z scheme approximations.

The order of accuracy $O(N)$ of the implementation obtained using (N) grid points is estimated by considering the reduction in error achieved when refining the mesh by a factor of three. The ratio of errors achieved on the coarser and finer mesh is given by $E(N/3)/E(N)$. For a n^{th}-order scheme, in the limit for very large N, this ratio would become 3^n, so that

$$E(N/3)/E(N) = 3^n. \tag{4.4}$$

The order of accuracy can then be calculated by taking the logarithm left and right, so after some algebra we obtain

$$\mathrm{O}(N) = \frac{\ln\left(E(N/3)/E(N)\right)}{\ln 3}. \tag{4.5}$$

To establish the order of accuracy obtained using either W5, W5-Z or the upwind central scheme C5, in Tables 4.4 and 4.5, the orders of accuracy are displayed that were obtained for very low and relatively large values of ε, respectively. Note that Tables 4.1 and 4.2 show that ε-independent errors were obtained at $\varepsilon = 10^{-12}$ and at $\varepsilon = 100$ for both W5 and W5-Z. Note that according to Eq. (3.35) ε needs to be larger than zero. It can be seen that the achieved order of accuracy of the W5 scheme is not as high as that of the W5-Z and C5 schemes. The latter two are quite close to the theoretical value of 5, with the exception of the finest mesh, which shows a drop in the accuracy that is likely due to macine accuracy (truncation errors).

	$O(N)$		
N	W5	W5-Z	C5
10	–	–	–
30	3.04	5.00	4.92
90	3.45	4.97	4.99
270	3.56	4.20	4.20

Table 4.4
Order of accuracy as a function of the number of grid points N, obtained using $\varepsilon = 10^{-12}$ in the calculation of the weights in W5 and W5-Z, while estimating the convection of (4.2) using $u = 1$.

For very large ε, the order of accuracy of both the W5 and W5-Z schemes becomes identical to that of the C5 scheme. This is directly related with the definition of the weights for the WENO scheme, which for $\varepsilon \to \infty$ become the same as the weights used in the C5 scheme. Note that as a result also the approximation errors will become similar to those of the C5 scheme. Above it was noted that the maximum

	$O(N)$	
N	W5	W5-Z
10	–	–
30	4.92	4.92
90	4.99	4.99
270	4.20	4.20

Table 4.5
Order of accuracy as a function of the number of grid points N, obtained using $\varepsilon = 100$ in the calculation of the weights in W5 and W5-Z, while estimating the convection of (4.2) using $u = 1$.

errors achieved for larger N in the W5 and W5-Z schemes were obtained for $\varepsilon \approx 10^{-6}$. Contrasting the $\varepsilon = 10^{-6}$ results shown in Table 4.6 to the results shown in Tables

	$O(N)$	
N	W5	W5-Z
10	–	–
30	3.03	5.00
90	3.41	4.97
270	2.76	4.20

Table 4.6
Order of accuracy as a function of the number of grid points N, obtained using $\varepsilon = 10^{-6}$ in the calculation of the weights in W5 and W5-Z, while estimating the convection of (4.2) using $u = 1$.

4.4 and 4.5 shows how much this effects the order of accuracy achieved. As also mentioned earlier, the order of accuracy of the W5-Z scheme is hardly effected by ε. However, the order of accuracy of the W5 scheme is somewhat effected, especially at $N = 270$, where it reduces from 3.56 (obtained at $\varepsilon = 10^{-12}$) to 2.76.
Note that the errors E obtained in the approximations of the convection of (4.2) were found to be the same for $u = -1$ as for $u = -1$.

In general we can draw the conclusion that for convection of the smooth 1D test function, the W5-Z scheme tends to produce more accurate results than the W5 scheme. The accuracy of the former is similar to the accuracy of the C5 scheme. Especially for larger N, when extremely small errors are required, it is best to use the W5-Z scheme. This, however, does not mean that the W5-Z scheme is also preferable if maximum errors are of 1% can be tolerated. Later we will present a second 1D test case that deals with the accuracy achieved when resolving a very steep gradient.

4.3 Approximation of steep gradients

After having verified the order of accuracy of the WENO schemes and the C5 schemes in the previous section, here we will focus on the accuracy approximating a

steep gradient using a relatively coarse mesh. The aim is to find out which of the two WENO methods, W5 and W5-Z, needs the fewest grid points to resolve the gradients with an error E less than 1%. To test this, a one-dimensional periodic function, γ, was defined containing two equally steep gradients:

$$\gamma(x,0) = \begin{cases} 0 & \text{if} \quad 0 \leq x < 11/24 \\ 1+\sin(12\pi x) & \text{if} \quad 11/24 \leq x < 13/24 \\ 2 & \text{if} \quad 13/24 \leq x < 17/24 \\ 1+\sin(12\pi x) & \text{if} \quad 17/24 \leq x < 19/24 \\ 0 & \text{if} \quad 19/24 \leq x \leq 24/24 \end{cases} \tag{4.6}$$

As can be seen in Figure 4.1, the periodic test function has a minimum of $\gamma = 0$ and a maximum of $\gamma = 2$. At $t = 0$, the two gradients with $\frac{d\gamma}{dx} = \pm 12\pi$ can be found near $x = 1/2$ and $x = 3/4$.

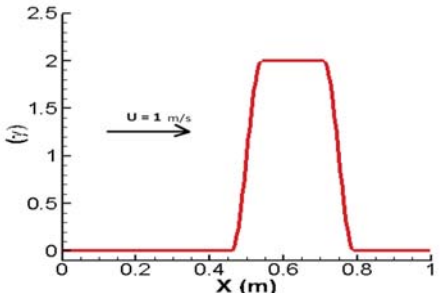

Fig. 4.1. Schematic of the periodic test function with steep gradients

In the test, the scalar γ is convected to the right with a constant velocity of $u = 1m/s$ over one flow-through time (equalling one second). As previously, the $1D$ convection Eq. (4.1) was discretised using both the WENO and the WENO-Z schemes for scalar convection with a three-stage Runge-Kutta method for time integration. For both the W5 and W5-Z schemes the accuracy of approximation of the convective test problem is assessed for a range of grid points $N = 40, 80, 160$ and 320. Note that the aim of this study was to identify a suitable WENO scheme to

explicitly resolve steep gradients on relatively coarse meshes. The results obtained on the coarsest meshes could possibly be improved by using a Riemann solver.

4.3.1 Results

Figure 4.2a shows the results obtained for the $W5$ method. It can be seen that the exact solution (which is obtained after one flow-through time and should be the same as the scalar distribution at $t = 0$) was not matched on any of the meshes even though, with increasing N the approximation was found to drastically improve. For the W5-Z scheme, shown in Figure 4.2b, the approximation using $N = 320$ grid points was found to be in very good agreement with the exact results. Compared to the W5 scheme, the W5-Z scheme generally only needs about 50% of the grid points in order to obtain results of similar quality as the W5 scheme. Both methods show an overestimation when the mesh is too coarse ($N = 40$). In both schemes, some

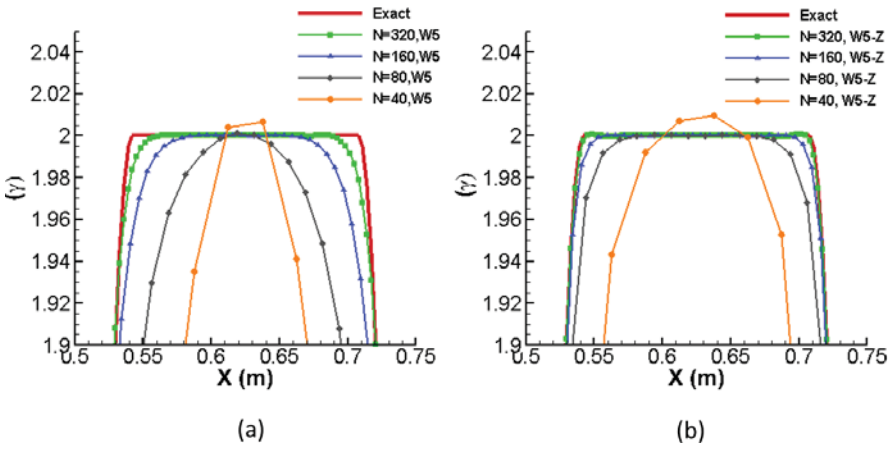

Fig. 4.2. Detailed view of the approximations of (4.1) obtained on various meshes after 1 s. of simulation (corresponding to one flow-through time) using (*a*) WENO and (*b*) WENO-Z

numerical diffusion is introduced to deal with steep gradients without too much (or any) under or overestimation. From the results presented so far, we can see that

compared to the W5 scheme, the numerical diffusion added by the W5-Z scheme is significantly less.

4.3.1.1 Optimization of the parameter ε

In Section 4.2.2, we validated the effect of changes in ε, used in (3.35) to determine the weights, on the order of accuracy of the WENO schemes. It was found that for W5-Z the choice of ε did not make much difference. For the $W5$ scheme, on the other hand, the resulting order of accuracy was found to be significantly effected by the value of ε. Usually, in combination with the W5 scheme $\varepsilon = 10^{-6}$ is selected [120], [3]. To determine the optimum value of ε when estimating a steep gradient on a coarse mesh, for both W5 and W5-Z the test problem was run using $\varepsilon = 10^{-2}, 10^{-3}, 10^{-4}$ and 10^{-6}. The steep gradients of (4.1) were approximated for the four values of ε using $N = 80$ grid points.

The results of this ε test for W5, W5-Z are shown in Figure 4.3a and b, respectively. It can be seen that both WENO schemes generate overshoots for the larger values of ε. In W5, this overshoot virtually disappears for $\varepsilon \leq 10^{-4}$. In contrast, for the W5-Z scheme a value of $\varepsilon \leq 10^{-6}$ was found to be needed. Despite this, the accuracy on the $N = 80$ point mesh of the W5-Z scheme, that was reached using $\varepsilon = 10^{-6}$, was still found to be significantly better then the accuracy of the W5 scheme reached with $\varepsilon = 10^{-4}$. Note that previously it was observed that for large values of (ε), both the W5 and the W5-Z schemes approach the fifth-order accurate upwind central scheme C5 that is independent of ε. Here is is seen that near steep gradients, for the larger values of ε over- and underestimation occurs which would also be found when using the C5 method.

For each method, W5 and W5-Z, we aim to asses how many points would need to be placed within the steep shear layer for an accurate approximation. Above it was shown that for both the W5 and the W5-Z schemes the approximation significantly improves with increasing number of grid points N. To avoid any under/overestimation

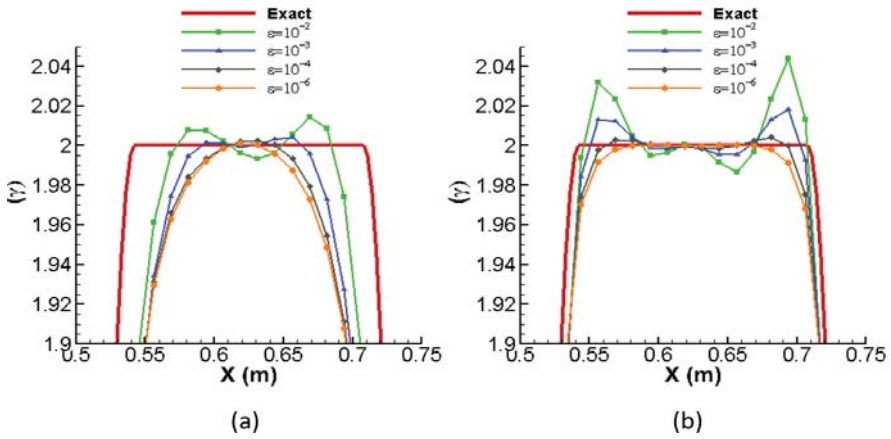

Fig. 4.3. Approximation of test function for various ε using (a) W5 and (b) W5-Z

ε was chosen to be 10^{-6}. At first, for both methods, the local solution near the steep gradient was assessed using $N = 40$ and 80 grid points. The results, shown in

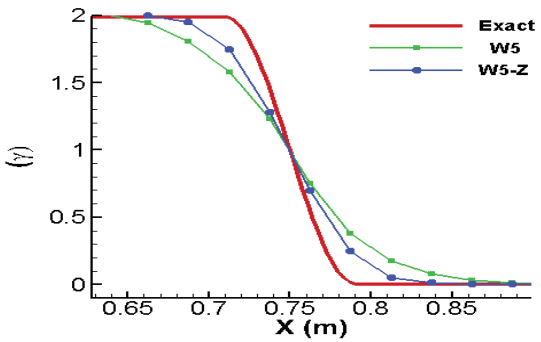

Fig. 4.4. Resolution of the gradient with $WENO$ and $WENO - Z$ using $N = 40$ grid points

Figure 4.4, indicate that with $N = 40$ grid points the approximation using the W5 method is worse than the W5-Z approximation which can be seen to somewhat better resolve the gradient. The W5-Z scheme smears out the gradient over about 8 grid points, while the W5 scheme uses about 11 grid points. The approximation of the gradient using $N = 80$ points is shown in Figure 4.5. For the W5-Z method the approximation in almost all points coincides with the exact solution, only in four of

the points a slight error can be seen. For the W5 method, on the other hand, at least in 11 of the grid points a deviation from the exact solution can be observed. From the Figures 4.4 and 4.5 it can be concluded that both methods converge to the exact solution for increasing N and that the results obtained using the W5-Z scheme are more accurate to the results obtained using the W5 scheme without using a Riemann solver.

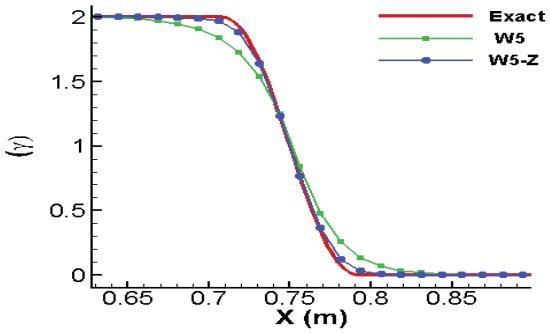

Fig. 4.5. Resolution of the gradient with $WENO$ and $WENO-Z$ using $N = 80$ grid points

4.4 Two dimensional test

As the surfactant calculations are carried out in two dimensions, the final test of the implementation comprises a 2D problem defined on a $1m \times 1m$ interval. Periodic boundary conditions were used in both x and y. In this simulation, the initial scalar concentration γ was defined by

$$\gamma(x, y, 0) = (2 + \sin(2\pi x) + \cos(2\pi y))/4, \tag{4.7}$$

while the velocity components were again chosen to be constant with values of ($u = 1\,\mathrm{m/s},\ v \pm 1\,\mathrm{m/s}$) and ($v = 1\,\mathrm{m/s},\ u \pm 1\,\mathrm{m/s}$), resulting in four different velocity directions. Note that Eq. (4.7) was selected to provide a non-constant, simple periodic initial condition so that for $u = v = \pm 1\,\mathrm{m/s}$ $\gamma(x, y, 1) = \gamma(x, y, 0)$ is obtained, which

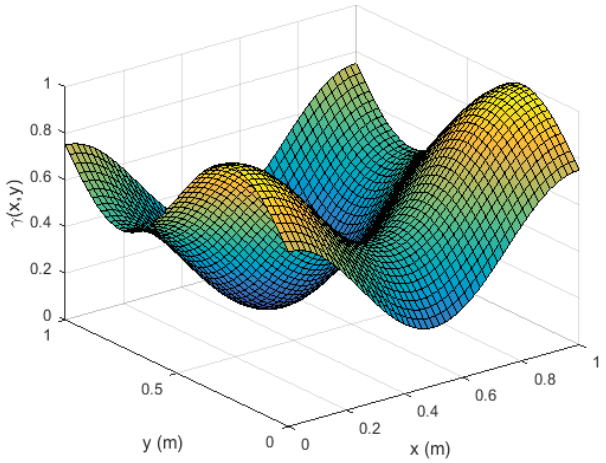

Fig. 4.6. surface plot of γ

makes it convenient to compare results and determine errors. Figure 4.6 shows a surface plot of the scalar distribution $\gamma(x, y, 0)$ at $t = 0\,\mathrm{s}$.

As in the $1D$ test for the determination of the order of accuracy in Section 4.2.1, seven different values for the parameter ε in (3.35) were used ($\varepsilon = 100$, 1.0, 10^{-2}, 10^{-4}, 10^{-6}, 10^{-8}, 10^{-12} and 10^{-16}) used in $1D$ test. Also, (4.5) is used to calculate the order of accuracy $O(N)$ of the $2D$ approximation obtained on 10×10, 30×30, 90×90 and 270×270 meshes. The error is obtained by comparing the approximation obtained after one flow-through time (1 second) to the initial scalar distribution at $t = 0\mathrm{s}$ at the location $(x, y) = (0.25, 0.05)$.

4.4.1 Results of the $2D$ test

The investigation of correctness of both the $2D$ WENO implementations for W5 and W5-Z is investigated by calculating the achieved order of accuracy on an $N \times N$ mesh. For completeness, also the results obtained using the fifth-order central upwind scheme are added. As observed earlier in the $1D$ test, also in Table 4.7, a fifth-order accuracy is indeed obtained for both the W5-Z and C5 schemes irrespective of the

		Order		
N	ε	W5	W5-Z	C5
10	10^{-12}	–	–	–
10	10^{-6}	–	–	–
10	100	–	–	–
30	10^{-12}	1.72	5.02	4.94
30	10^{-6}	1.73	5.02	4.94
30	100	4.94	4.95	4.94
90	10^{-12}	2.90	5.02	4.99
90	10^{-6}	2.98	5.01	4.99
90	100	4.99	4.99	4.99
270	10^{-12}	6.66	4.21	4.20
270	10^{-6}	5.02	4.20	4.20
270	100	4.20	4.21	4.20

Table 4.7
Order of accuracy $O(N)$ obtained in the approximation of the convection of (4.7) with W5, W5-Z and C5 using $u = 1$ $v = 1$. Simulations are performed using $\varepsilon = 10^{-12}$, $\varepsilon = 10^{-6}$ and $\varepsilon = 100$ in the calculation of the weights for W5, and W5-Z.

value of ε. For the W5 scheme results, however, on coarser meshed the order of accuracy is relatively low for $\varepsilon \leq 10^{-6}$ and $N \leq 90$. For the finest mesh with $N = 270$ the order of accuracy achieved in W5 exceeds or is close to the theoretical value of five. The same is true for all grids if $\varepsilon = 100$. This is because (as mentioned earlier) got large values of ε all WENO schemes begin to resemble the C5 scheme.

Note that the accuracy of the results obtained using the three discretisations of the scalar convection with convection velocities $u = -1\,\mathrm{m/s}$, $v = -1, 0, 1\,(\mathrm{m/s})$ and $u = 1\,\mathrm{m/s}$, $v = -1, 0\,(\mathrm{m/s})$ were consistent with the results presented for

$u = v = 1\,\mathrm{m/s}$ in Table 4.7 and were therefore omitted.

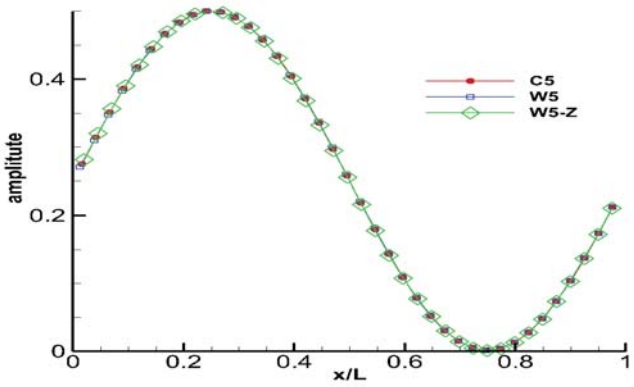

Fig. 4.7. Cross section at $y =$ of the 2D periodic scalar distribution defined in (4.7), after it was convected to the right during 1 second at a velocity $u = 1\,\mathrm{m/s}$ and $v = 0\,\mathrm{m/s}$. Results achieved using the W5, W5-Z and C5 methods employing 40 grid points are compared.

Figure 4.7 shows approximations of W5, W5-Z and C5, obtained at $t = 1\,\mathrm{s}$ of a cross-section at $y = 0.5$ of the 2D scalar distribution defined at $t = 0\,\mathrm{s}$ in Eq. (4.7). The scalar is convected to the right with a velocity $u = 1\,\mathrm{m/s}$ and $v = 0\,\mathrm{m/s}$. It can be seen that all three methods used for the discretisation of the convection term give a very good approximation of the scalar distribution obtained after one second.

From the tests carried out in this chapter we can conclude that the WENO schemes were discretised correctly. Also, it was shown that, without using a Riemann solver, the W5-Z scheme gives more accurate results than the traditional fifth-order-accurate WENO scheme of Liu *et al.* [2].

Chapter 5: Influence of surfactants on low diffusion mass transfer

Direct Numerical Simulations (DNS) were used to study the influence of surface contamination on the interfacial mass transfer of low Schmidt number gases. The gas transfer was promoted by isotropic turbulence, generated in a separate large-eddy simulation, that was introduced as the bottom boundary condition in the DNS. A variety of contamination levels were considered ranging from clean to severely contaminated. Before starting the study of the effects of surfactants on interfacial gas transfer, the flow in the DNS was allowed to become fully developed for $300L/U$ time-units. At $t = 0L/U$, the surfactant concentration was initialised to $\gamma/\gamma_0 = 0$. After the initial $300L/U$ time-units, the dissolved gas concentrations were subsequently reinitialised using the exact solution for pure scalar diffusion

$$c(x, y, \zeta) = \mathrm{erfc}\left(\zeta \sqrt{\frac{Sc\,Re}{4\,t_0}}\right), \tag{5.1}$$

obtained after $t_0 = 7\,L/U$ time-units (and the time was reset to $t = t_0 L/U$ time-units). In the presence of surface contamination, the mass transfer velocity (K_L) was found to scale as a power of the Schmidt number, i.e Sc^{-q} where q smoothly transitions from $q = 1/2$ for clean surfaces to $q = 2/3$ for very dirty interfaces. A power law $K_L \propto Sc^{-q}$ is proposed in which both the exponent q and the constant of the proportionality become functions of the clean surface fraction.

5.1 Introduction

The presence of surfactants show a huge effect on mass transfer across the air water interface. Some general information about surfactants was given already in Chapter 2. Direct Numerical Simulations were applied to study the influence of surface contamination on mass transfer at low gas diffusivity across a flat surface. A local reductions in surface tension occur when the local contamination level is increased. This reduction in surface tension induces Marangoni forces that act to reduce the uneven distribution of surface tension therefore damping near-surface turbulence and forcing the 2D flow at the surface to become more divergence-free. The reduction in surface-tension with increasing surfactant concentration is assumed to be linear, resulting in the model detailed in Section 3.1 that relates horizontal gradients of the surfactant concentration to vertical gradients of the horizontal velocity through a model parameter Ma/Ca that depends on the actual contamination and turbulence level. For the research into mass transfer across a surfactant-contaminated air-water interface some assumptions were made about the surfactant. As mentioned in Chapter 1, the surfactants are assumed to be lighter than water and that they do not mix with water so that the total surfactant concentration at the surface will be conserved. As mentioned in Chapter 2, oleyl alcohol ($C_{18}H_{36}O$) is considered as an example of a surfactant with the desired properties.

The effect on interfacial gas transfer of a wide range of surfactant contamination levels was investigated and compared to so-called clean conditions, corresponding to a free-slip surface-boundary-condition and severely contaminated (dirty) conditions which are approximately represented by no-slip boundary conditions. Asher & Pankow [42] and McKenna & McGillis [47] compared clean and contaminated surface boundary conditions and found a reduction in gas transfer velocity up to 80%. Herlina & Wissink [10] used DNS to study the limiting case of tehe severe contamination condition, modelled using no-slip boundary conditions at the surface, at Schmidt numbers up to $Sc = 500$, which is representative for oxygen in water. The

effect of surface contamination on surface-shear-driven gas transfer was investigated at Schmidt numbers of $Sc = 1$ and $Sc = 100$ in the hybrid DNS and LES study by Hasegawa *et al.* [135]. They found a reduction in the gas transfer velocity K_L of about 65% compared to clean condition for the higher Sc number.

5.2 Surfactant diffusivity

As previously shown by e.g. Kharpour *et al.* [97], the presence of surfactant contamination has a significant effect on gas transfer across the air-water interface caused by a local decrease in surface tension as explained above.

Khakpour *et al.* [97] simulated surfactants for a range of Schmidt numbers from 0.5 to 8. They found that the surfactant Schmidt number Sc_s did not affect the evolution of the surfactant concentration at the flow surface and, hence, they used $Sc_s = 1$. Other researchers used various Sc_s in their research. Tsai & Yue [102] chose $Sc_s = 0.83$ number as 0.83, while Tsai [106] [136] used a value of $Sc_s = 2$. Handler *et al.* [108] used values of $Sc_s = 0.056$ and 5.6, while Hasegawa & Kasagi [135], finally, assumed $Sc_s = 1$ for their experimental study.

To confirm that the Schmidt number independency reported previously by Khakpour *et al.* also holds in the present simulations, surfactant transport was simulated for a range of Schmidt numbers from 0.5 to 8.

5.2.1 Test for surfactant Schmidt number independency

Direct Numerical Simulations (DNS) were employed here to obtain highly resolved solutions of the flow field and the surfactant concentration. To investigate the influence of surfactant Schmidt number (Sc_s) on the evolution of the surfactant simulations were carried out for $t = 40$ time units using exactly the same initial conditions with a fully developed flow field. At $t = 0$, the surfactant was given a value of one (meaning one times the equilibrium value) everywhere at the surface and Ma/Ca was set to $Ma/Ca = 600$. The Re number was $Re = 600$, based on artificially chosen

characteristic scales that are more or less typical for lab-based experiments. The characteristic length scale was $L = 0.01m$, the kinematic viscosity $\nu = 10^{-6}m^2/s$ and the velocity scale U was $U = 600 * \frac{\nu}{L}$. The surfactant Schmidt numbers used in the simulations were $Sc_s = 0.5, 1, 2$ and 8.

Being able to perform simulations at a relatively low surfactant Schmidt number Sc_s (which could be much lower than the real one) is beneficial as otherwise a very fine mesh would be needed at the surface to properly resolve the surfactant.

5.2.2 Results

Using the test problem described above, the effect of various Schmidt numbers on the surfactant distribution at the flow surface was investigated Snapshots of the

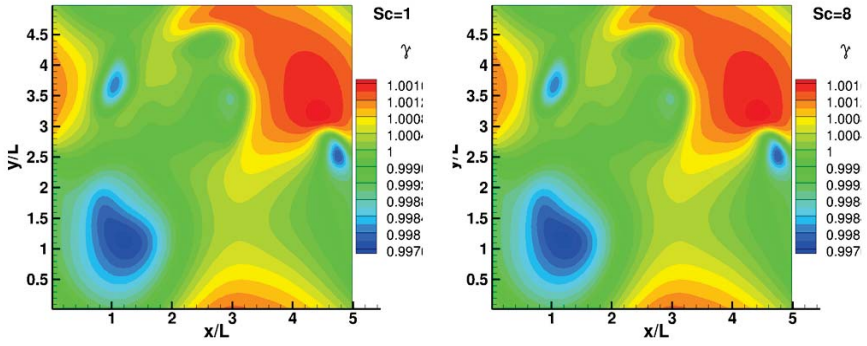

Fig. 5.1. Comparison of the surfactant distribution obtained for Schmidt numbers $Sc_s = 1$ and $Sc_s = 8$ at $t = 40L/U$

surfactant distribution obtained after 40 time-units of simulation at $Sc = 8$ and $Sc = 1$ are compared in Figure 5.1. It can be seen that the colour contours of the surfactant distribution are in very good agreement. Note that because of the relatively large Ma/Ca, this simulation would represent a very dirty interface. In order to further verify the Sc_s independency of the surfactant concentration γ/γ_0 in Figure 5.2 profiles of γ/γ_0 obtained at $Sc = 0.5, 1, 2, 8$ along $y/L = 2.5$ and $x/L = 2.5$ are compared. The profiles are in excellent agreement, so that it can be concluded

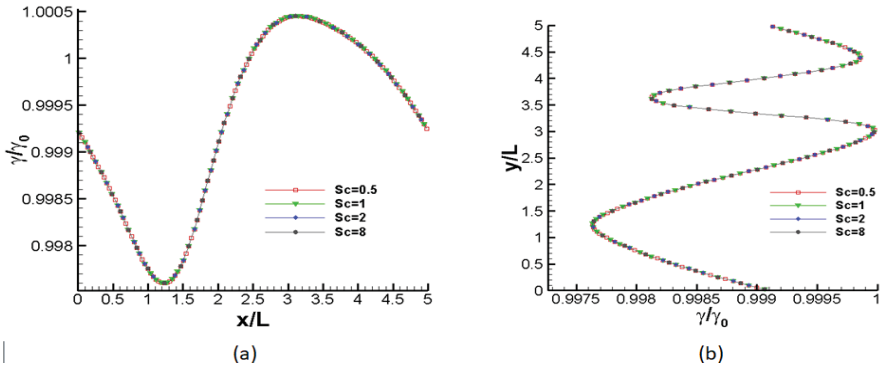

Fig. 5.2. Distribution of surfactant concentration on the flow surface at a certain location for range of Sc numbers

that the distribution of γ is indeed independent on Sc_s at least for $Sc = 0.5$ to $Sc_s = 8$. It is assumed that this independency will also hold for larger Sc_s. The latter could be verified by performing simulations of the surfactant distribution at higher Sc_s, or perhaps simulations using zero diffusivity, which was not within the scope of the present research.

The final part of the test is to find out whether the surface-velocities (which are affected by the surfactant distribution) are also independent of the Sc_s.

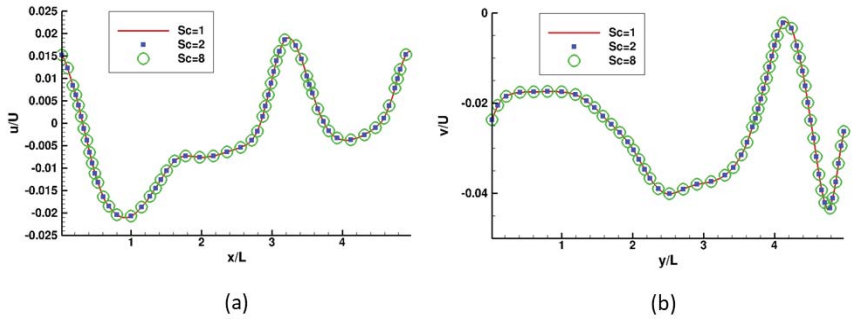

Fig. 5.3. Interfacial velocities for $Sc = 1, 2$ and 8 showing (a) u at the centre line $y/L = 2.5$ and (b) v at $x/L = 2.5$

Figure 5.3 shows that the centre line velocities are also in very good agreement for $Sc_s = 1 - 8$. Again, we assume that this will also be the case for larger Sc_s. In fact, the largest differences between the velocity profiles was less than 10^{-7}, which is negligibly small.

5.3 Overview of the simulations

A computational domain of size $L_x \times L_y \times L_z = 5L \times 5L \times 3L$ was used in the present DNS direct numerical simulations (see Section 3.3.4). In all simulations, a Reynolds numbers of $Re = UL/\nu = 600$ was chosen based on a characteristic length scale L of 0.01 m, with a kinematic viscosity of $\nu = 10^{-6}$ m^2/s and a characteristic velocity scale of $U = 0.06$ m/s. Note that the characteristic scales are of the same order of magnitude as the scales used in the experiments of [20]. In fact, they are just place holders as the relevant turbulent length and viscosity scales will only be known after the calculations. These turbulent scales will then be used to calculate the turbulent Reynolds number Re_T. In all simulations (apart from the surfactant) five scalar equations for gas transfer are simultaneously solved using Schmidt numbers of $Sc = 2, 4, 8, 16, 32$ in order to establish the scaling of the gas transfer velocity with Sc. The scalars with the smallest two Sc were resolved on the baseline-mesh, while the rest of the scalars were solved on the refined mesh with a refinement factor of 2. As can be seen in Figure 5.4, the simulation uses three computational domains which are mentioned in Section 3.3.4. The main computational domain (the DNS domain) was based on the experiments of Herlina *et al.* [137] The studies of Herlina & Wissink [11], [64] also considered the experiments performed by Jirka *et al.* [137]. The flow was solved using a $128 \times 128 \times 212$ baseline mesh (see Table **??**). Note that $\zeta = L_z - z$ is used in some of the figures, where L_z is the height of the computational domain and ζ is the distance to the surface. Note that the parameter Ma/Ca corresponds to $ReMa/We$ as used by e.g. Khakpour *et al.* [97], as explained in Section 3.1.1.

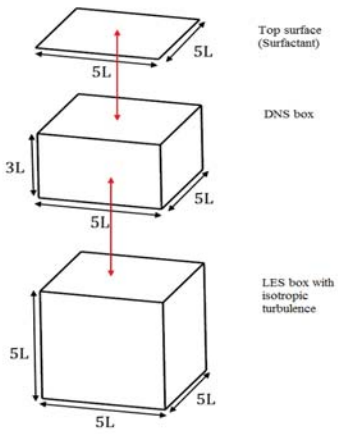

Fig. 5.4. Computational domain

Run	Ma/Ca	u_∞/U	L_∞/L	Re_T	Ma/Ca_T
S0	0.0	0.1130	1.0333	141	0
S1	0.12	0.1119	0.9579	128	1
S2	0.6	0.1169	0.9935	139	5
S3	1.2	0.1085	0.9835	131	11
S4	6	0.1104	0.9273	125	54
S5	30	0.1114	1.0209	138	269
SN	No-slip	0.1073	0.8984	117	No-slip

Table 5.1
Overview of the simulations

Because of the isotopic turbulence that is introduced at the bottom of the computational domain at the surface, the mean shear $(\overline{\frac{\partial u}{\partial z}} = \overline{\frac{\partial v}{\partial z}}) = 0$. The instantaneous or turbulent shear, however, is usually not zero and is heavily dependent on the isotropic turbulence diffusing from below. This importance of this turbulence is measured by the turbulent Reynolds number Re_T which requires knowledge on the integral length scale and the rms of the horizontal velocity u_{rms}. Because of that Re_T could only be determined after the simulation was performed. The size of com-

putational domains used in the DNS $[(L_x \times L_y \times L_z) = (5L \times 5L \times 3L)]$ and the LES $[(L_x \times L_y \times L_z) = (5L \times 5L \times 5L)]$ are quite small. Even though the isotropic turbulence introduced at the bottom of the DNS domain was of quite high intensity, the restriction on the integral length scale due to the small DNS domain resulted in relatively small turbulent Reynolds numbers.

The isotropic turbulence is generated in a separate, concurrently running large-eddy simulation (LES). A $64 \times 64 \times 64$ mesh was used to discretize the periodic box. At the bottom of all DNS calculations exactly the same sequence of turbulent flow fields (a horizontal cross-section of the turbulent flow field generated in the LES) was introduced. Because the DNS mesh was much finer than the LES mesh, a fourth-order interpolation of the LES flow field from the horizontal cross-section was carried out to obtain the bottom DNS boundary condition. Because of the absence of mean flow, $u_i' = u_i$, where the prime identifies the fluctuation velocity. The Turbulence level and turbulent kinetic energy were defined in Section 3.3.2 as $Tu = \sqrt{2 < k > /3} = 0.4$ and $k = \overline{u_i' u_i'}/2 = \overline{u'u'}/2$. Note that both in the LES and at the bottom of the DNS, due to the presence of isotropic turbulent flow, all components of the Reynolds' stress are the same e.g. $\overline{u'u'} = \overline{v'v'} = \overline{w'w'}$. where $\langle \cdot \rangle$ corresponds to averaging homogeneous directions and $\bar{(\cdot)}$ corresponds to averaging in time.

The Ma/Ca numbers employed in the simulations ranged from (free-slip) $Ma/Ca = 0$ to $Ma/Ca = 30$, to complete the series, the no-slip case was also included. This latter case corresponds to the severely contaminated surface condition, typical for very large Ma/Ca. The top boundary condition depends on the choice for Ma/Ca. which affects the near surface turbulence and increasingly damps (with increasing Ma/Ca) near surface turbulent fluctuations.

The rms of the horizontal velocity reads

$$u_{rms}(\zeta) = \sqrt{\overline{\langle u'u' \rangle}} \tag{5.2}$$

and the longitudinal integral length scale L_{11} is defined

$$L_{11}(\zeta) = \int_0^{L_x/2} R_{11}(r, \zeta) dr, \tag{5.3}$$

where the two point correlation R_{11} is defined by

$$R_{11}(r,\zeta) = \frac{\int_{x=0}^{L_x/2}\int_{y=0}^{L_y} u'(x,y,\zeta)u'(x+r,y,\zeta)dydx}{\int_{x=0}^{L_x/2}\int_{y=0}^{L_y} u'^2(x,y,\zeta)dydx}, \tag{5.4}$$

The integral length scale and the characteristic turbulent velocity were assessed based at $\zeta = L$, consequently;

$$\begin{aligned} u_\infty &= u_{rms}|_{\zeta=L}, \\ L_\infty &= \overline{L_{11}}|_{\zeta=L}. \end{aligned} \tag{5.5}$$

Following the experiments for grid-stirred turbulence by [138], [92], the turbulent length scale, Λ, used in Re_T was defined by $\Lambda = 2L_\infty$, so that turbulent Reynolds number reads

$$Re_T = \frac{u_\infty \Lambda}{\mu} \tag{5.6}$$

The turbulent capillary number Ca_T was defined in Section 3.1.1 by

$$Ca_T = \frac{\mu u_\infty}{\sigma} \tag{5.7}$$

Most of the analysis was carried out by time averaging the results from $t = 150$ to $t = 300$, which coincides with nearly seven eddy turnover times ($2L_\infty/u_\infty$). Because in this time-interval the gas concentration distribution became quasi-steady (i.e. de average values changed only very slowly in time). Note that the parameter Ma/Ca_T was characterised by the surfactant contamination level.

As explained in Section 5.2 the exact surfactant Schmidt number is not important for the calculation of the surfactant concentration. Therefore all simulations were performed using a surfactant Schmidt number of $Sc_s = 2$.

It is accepted that, according to works of Coantic [139] and Ledwell [140], the gas transfer velocity (K_L) scales as $Sc^{-1/2}$ for clean surface conditions (free-surface), while the transfer velocity (K_L) scales as $Sc^{-2/3}$ for dirty surface (no-slip) conditions. Furthermore, based on the numerical investigation of Hasegawa & Kasagi [135], Shen *et al.* [1] and Khakpour *et al.* [97], it can be concluded that severely contaminated water surfaces could be estimated by a no-slip surface boundary condition. However,

according to Hasegawa & Kasagi [135], who observed that for higher levels of contamination the interfacial mass transfer scaling, as a power of the Schmidt number, 'switches' from $Sc^{-0.5}$ to $Sc^{-0.7}$ for clean and severely contaminated surfaces, respectively. A modified version of Theofanous' *et al.* [19] dual-regime model, proposed by Herlina & Wissink [10] for no-slip surface boundary conditions, is given by

$$\frac{K_L}{u_\infty} \propto Sc^{-2/3} {Re_T}^{-1/2}, \tag{5.8}$$

$$\frac{K_L}{u_\infty} \propto Sc^{-2/3} {Re_T}^{-1/4}. \tag{5.9}$$

The $R_T < R_{T,crit}$ and $R_T > R_{T,crit}$ conditions correspond to Theafanous' large-eddy (5.8) and small-eddy (5.9) model respectively.

In order to investigate which scaling would be applicable for a range of contamination levels, it is assumed that the gas transfer velocity is a function of the Schmidt number and the turbulent Reynolds number and can be estimated by

$$\frac{K_L}{u_\infty} = c {S_c}^{-q} {Re_T}^{-r}. \tag{5.10}$$

Here, the high and low R_T regimes correspond to the powers $r = 1/2$ and $r = 1/4$ respectively. Based on this approximate expression (5.10), the dependency of the power q on the contamination level at the water surface is determined.
Note that in the DNS calculations, surface waves are assumed to be very shallow so that the interface can be modelled using a rigid lid assumption.

In order to obtain the actual power (q) that corresponds to certain contamination levels and to determine c (the constant of proportionality) the least squares method was employed using the DNS results obtained at various Sc.

The bulk concentration c_b was evaluated at the location z_b in the upper bulk where $c_{rms}(z_b) = \frac{1}{2} \max_z c_{rms}(z)$ holds. Using c_b, the instantaneous gas transfer velocity

$$k_L(t) = \left\langle -\frac{c_s}{c_s - c_b} \frac{1}{ReSc} \frac{\partial c}{\partial z}\bigg|_{z=L_z} \right\rangle \tag{5.11}$$

is determined, which is used to calculate the mean gas transfer velocity $K_L = \overline{k_L}$.

The analyses were performed using time-averaging over the interval from $t = 150$ to $t = 300$. The behaviour of the $S5$ and $S1$ cases are close to no-slip and free-slip boundary conditions, respectively. In other words, the power of the Schmidt number in the $S1$ ($Ma/Ca_T = 1$) case was found to be close to the one achieved in the clean surface condition ($Sc^{-1/2}$), while for $S5$ ($Ma/Ca_T = 269$) the power is similar to the one for severely contaminated conditions ($Sc^{-2/3}$) as obtained in case SN see Figure 5.5.

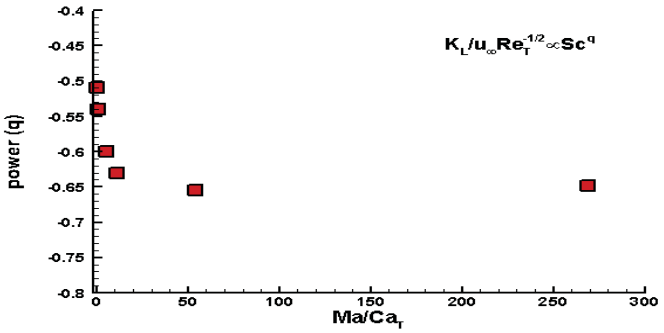

Fig. 5.5. Variation of power (q) with Ma/Ca_T

The scaling of the normalised gas transfer velocity (K_L) as a power, q, of the Schmidt number Sc was determined for a range of Ma/Ca_T. It can be seen that in Figure 5.5, the power q decreases from $-1/2$ for $Ma/Ca_T = 1$ to $-2/3$ for $Ma/Ca_T = 54$. For even higher Ma/Ca_T the power remains virtually constant. Thus the lowest contamination level considered, where $Ma/Ca_T = 1$, very nearly scales with $Sc^{-1/2}$ (clean case condition), while the highest level of contamination considered ($Ma/Ca_T = 54$) scales similar as the severely contaminated surface condition where $Sc^{-2/3}$.

5.4 Turbulent Flow Statistics

The effect of surface contamination on the turbulent flow statistics was evaluated for range of surfactants level. The same turbulent (*isotropic*) flow-field is presented at $z = 0$, whilst at the surface ($z = L_z$) the flow is completely homogeneous in the

horizontal directions and the effects of different levels of surfactants were introduced through changing the surface boundary conditions for the horizontal velocities in the Direct Numerical Simulations (DNS) as described earlier.

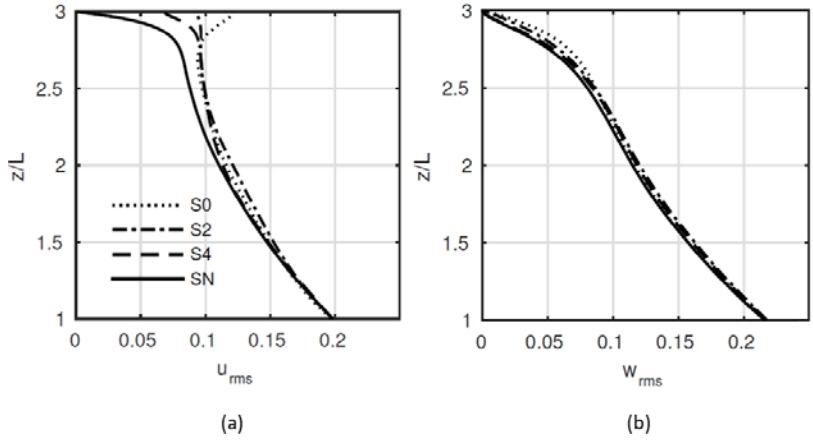

Fig. 5.6. Effect of Ma/Ca_T on the near surface turbulent flow statistics: (a) u_{rms} (b) w_{rms}

The turbulent velocity fluctuations are damped with increasing distance from the turbulence source at the bottom ($z = 0$). The horizontal velocity fluctuation, displayed in Figure 5.6a, were obtained by averaging the horizontal velocities components of u_{rms} and v_{rms} in time. Both horizontal and vertical velocity fluctuations show noticeable differences when approaching the surface due to the specific boundary condition at the surface. It can be seen that at the surface, the horizontal velocity fluctuation level changes dependent on the magnitude of Ma/Ca_T, while the rigid lid assumption caused the vertical velocity fluctuations to become zero for all cases. Note that in the lower part of the computational domain up to $\approx 1.5L$, the horizontal and vertical fluctuations show a very similar behaviour for all cases. (see Figure5.6a, b)

The detailed plots of the u_{rms} profiles close to the surface are shown in Figure 5.7. In all simulations, the horizontal velocity fluctuations (u_{rms}) profiles were found to be very similar up $\zeta \approx 2.8L$, with the exception of the SN simulation which shows quite a

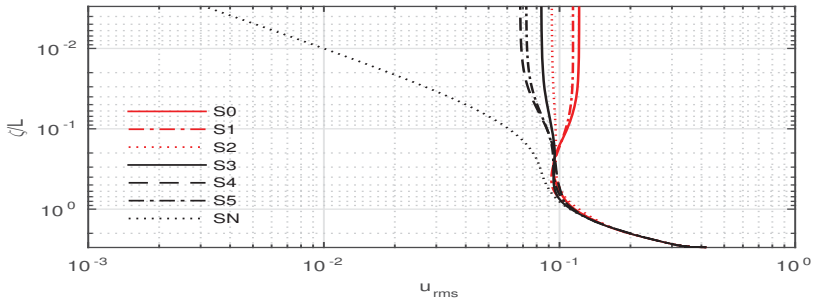

Fig. 5.7. effect of Ma/Ca_T on the near surface turbulent flow statistics detail plotted of u_{rms} in logarithmic scale and using the inverse coordinate $\zeta = L_z - z$. Shown in time averaged ($t = 150-300$) results.

different result due to the no-slip boundary condition at the surface. As opposed to the high Ma/Ca_T simulations, where the Marangoni forces push the surface divergence to zero so that the 2D surface velocity field becomes almost divergence-free (but not necessarily zero), in SN the horizontal velocity is forced to become zero. Apart from $S0$ and $S1$, in all simulations u_{rms} was found to decrease in the near surface region where $z > 2.8L$. In $S0$ and $S1$, however, u_{rms} was found to increase. Note that very similar results were obtained for $S0$ and $S1$ as well as for $S4$ and $S5$. The u_{rms} levels obtained were found decrease with with increasing levels of pollution ranging from $S0$ (free-slip) to $S5$. The decrease in u_{rms} illustrates that rising levels of surface contamination tend to increase near-surface turbulence damping. The increase in u_{rms} observed in $S0$ and $S1$ is caused by the redistribution of turbulent kinetic energy: close to the surface, the vertical velocity fluctuations decline and as a result the horizontal fluctuations are enlarged (see also Perot & Moin [141]). The aforementioned rising levels of surface contamination result in increased instantaneous shear and, hence, in increased damping of u_{rms} as can be seen in Figure 5.7 for $S2$–$S5$.

Figure 5.8 shows detailed profiles of w_{rms}. It is observed that the w_{rms} profiles exhibit a similar decreasing trend with Ma/Ca_T as obtained for u_{rms}. The w_{rms} profiles obtained in $S0$ and $S1$ and in SN and $S5$ almost coincide.

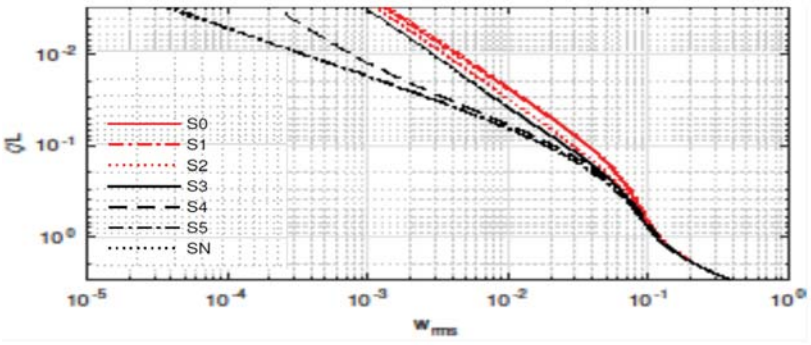

Fig. 5.8. effect of Ma/Ca_T on the near surface turbulent flow statistics. Detailed plot of w_{rms} with logarithmic scale, using the inverse coordinate $\zeta = L_z - z$. Shown are time averaged ($t = 150 - 300$) results.

With the exception of the no-slip simulation SN, all cases have a non-zero two-dimensional (2D) velocity field at the surface. While in the free-slip simulation the velocity field quickly becomes three-dimensional with increasing depth as $w \propto \zeta$, in cases with large Ma/Ca_T this takes much longer as $w \propto \zeta^2$. The latter is a result of the Marangoni effect caused by horizontal gradients in the surfactant concentration inducing a force counteracting the aforementioned surfactant gradients therefore effectively forcing the 2-D flow at the surface to become almost divergence free $\frac{\partial u}{\partial x} + \frac{\partial v}{\partial y} \approx 0$. The turbulent integral length scale and the Kolmogorov length scale are shown in Figure 5.9(a) and (b), respectively, for all simulations. The L_{11} results shown were time-averaged from $t = 150$ to 300, while the Kolmogorov length scale (η) profiles represent instantaneous results obtained at the final time step $t = 300$. L_{11} is first observed to increase with distance from the turbulent source until it reaches a local maximum at $\zeta \approx 0.5L$. After reaching the local maximum, L_{11} reduces to 0 towards the surface for the no-slip case ($S0$). However, for moderate to large levels of contamination (Ma/Ca_T), as in simulations $S2$ to $S5$, L_{11} increase again when approaching the surface. The increase in L_{11} is attributed to the presence of instantaneous shear which becomes stronger with increasing Ma/Ca_T such that for $S2$ to $S5$ an increased horizontal integral length scale is obtained. For zero or very low levels

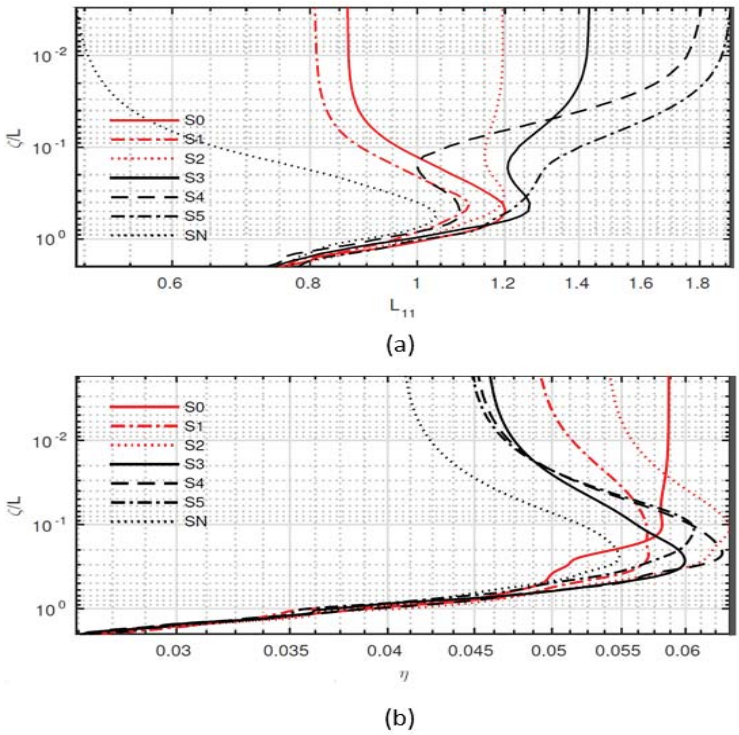

Fig. 5.9. Vertical variation of (a) turbulent integral length scale L_{11} (time averaged from $t = 150 - 300$) and (b) Kolmogorov length scale η at $t = 300$.

of contamination ($S0$ and $S1$), due to the reduction in instantaneous shear, L_{11} again reduces towards the surface and reaches levels of about 0.87 and 0.80, respectively.

The range of Kolmogorov length scales obtained at $t = 300\,L/U$ for various simulations is shown in Figure 5.9 (b). The Kolmogorov length scale $\eta = (\nu^3/\epsilon)^{1/4}$ is calculated using the dissipation ϵ of turbulent kinetic energy calculated by

$$\epsilon = \langle 2\nu S_{ij} S_{ij} \rangle \tag{5.12}$$

where $S_{ij} = \frac{1}{2}(\frac{\partial u'_i}{\partial x_j} + \frac{\partial u'_j}{\partial x_i})$. It can be seen that because of the dissipation of turbulent kinetic energy η increases from the bulk region until a maximum is obtained approximately between $\zeta = 0.1L$ and $\zeta = 0.2L$. With the exception of $S0$, η is observed to increase from the lower bulk upwards and reaches a maximum between $\zeta = 0.1L$ and $0.2L$. Closer to the surface for S0 η becomes constant while for the other sim-

ulations η reduces. The latter might indicate vortex stretching due to the presence of instantaneous shear resulting from either no-slip boundary conditions (in SN) or Marangoni forces.

The effect of shearing on the interfacial integral length scale L_{11} is demonstrated by visualising the vortical structures close to the surface in Figure 5.10. To identify these structures, the λ_2 criterion of Jeong& Hussain [142] was employed, where λ_2 is the second eigenvalue of the sum of the squares of the symmetric and antisymmetric parts of the velocity gradient tensor. The near-surface vortical structures obtained in simulations $S4$, $S5$ and $S0$ were found to be quite different. In $S0$, fewer structures were found to reach the surface than in $S5$ and $S5$. Also, while in $S0$ all structures that reach the surface are orthogonal and have constant diameter to the surface, in $S4$ and $S5$, they typically are non-orthogonal. The latter implies that their cross sectional area with the surface is increased (even though the diameter of the tubes is actually smaller). Note that the diameter of the vortex tubes typically scale with the Kolmogorov length scale [143]. The fact that the orthogonal tubes at the surface in $S0$ have constant diameter is in agreement with the constant value of η observed in Figure 5.9*b*. The observation that the vortex tubes in $S4$ and $S5$ are non-perpendicular to the surface (resulting in the aforementioned larger cross-sectional area) while at the same time the tube-diameter becomes wider when approaching to the surface may explain the larger L_{11} obtained at the surface. The non-perpendicular tubes at the surface are due to Marangoni forces inducing instantaneous shear.

The turbulent Reynolds number Re_T profiles obtained in the simulations $S0$, $S2$, $S4$, SN are shown in Figure 5.11. In all simulations, Re_T was found to be approximately constant between $z = 1.5L$ to $z = 2.25L$. This is in agreement with the observation made earlier by Wissink & Herlina [10], where the horizontal velocity fluctuations u_{rms} decayed when approaching the surface (in the z direction) while simultaneously L_{11} increased such that Re_T was observed to remain constant, see also in [92].

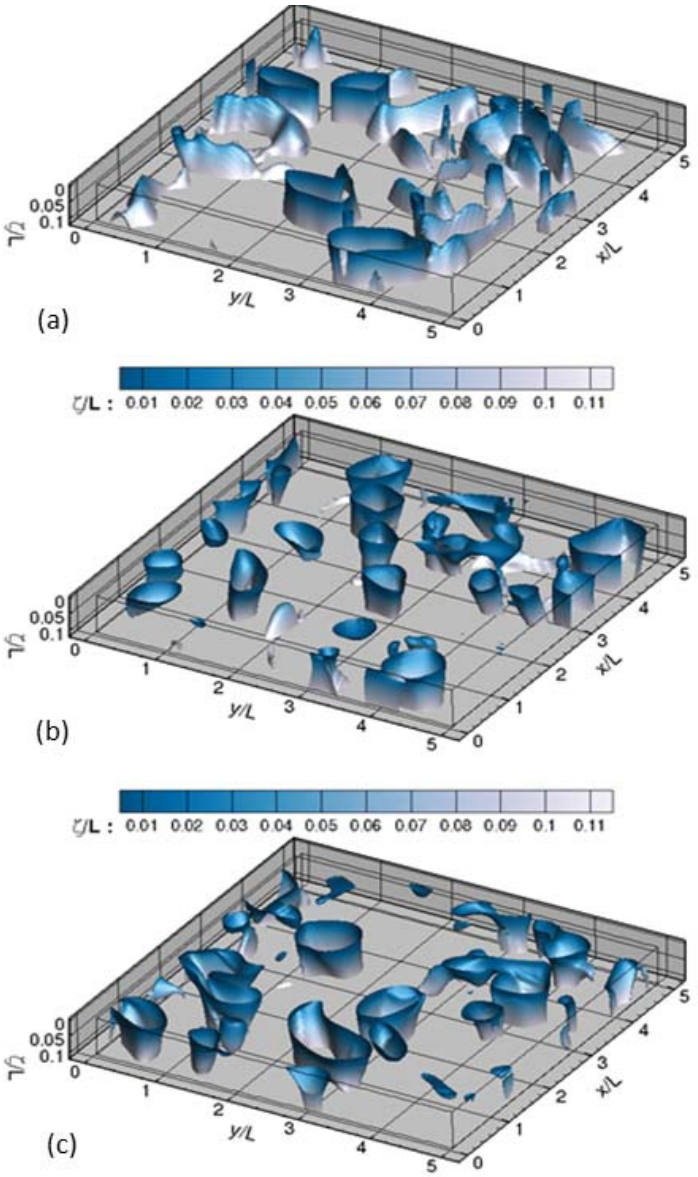

Fig. 5.10. Vortical structure identified using the isosurface of $\lambda_2 = -0.001$ from simulations (a) $S0$, (b) $S4$ and (c), $S5$ The isosurfaces are coloured by the distance ζ from the surface

5.5 Effect of Ma/Ca_T

5.5.1 Qualitative observations

The near surface horizontal velocity fluctuations, generated by the isotropic turbulence diffusing from below, was found to be significantly influenced by the level

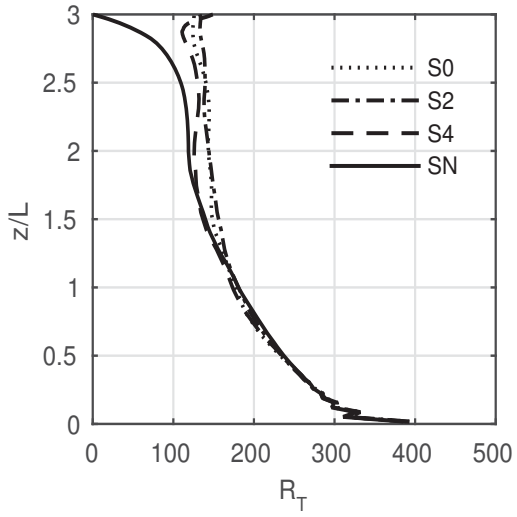

Fig. 5.11. Effect of Ma/Ca_T on Re_T. Shown are time-averaged ($t = 150 - 300$) results

of contamination. In particular, the upwelling and downwelling motion of the water was found to reduce with increasing contamination level, as measured by the parameter Ma/Ca_T. Figure 5.12 shows snapshots of the horizontal velocity field combined with colour contours of the velocity magnitude. It can be seen that the slightly contaminated case $S1$ shows significant horizontal velocity fluctuations which gradually reduce for $S3$ and $S5$ with increasing Ma/Ca_T. Also, the vector field in $S1$ shows relatively strong upwelling and downwelling motions, which in $S3$ and $S5$ become increasingly weak. These upwelling and downwelling motions are especially important for the promotion of gas-exchange. While at the air-water interface the gas transfer is fully dominated by diffusion, at lower levels, vertical velocity fluctuations become the main responsible for the transport of gases deeper down into the bulk. A damping of these vertical fluctuations will result in a reduction of atmospheric gas transfer. Hence, Figure 5.12 indirectly shows that the interfacial gas transfer will reduce with increasing levels of contamination. Note that for the vertical velocity fluctuations close to the surface to be reduced, it is not necessary that the horizontal velocity at the surface is reduced to zero.

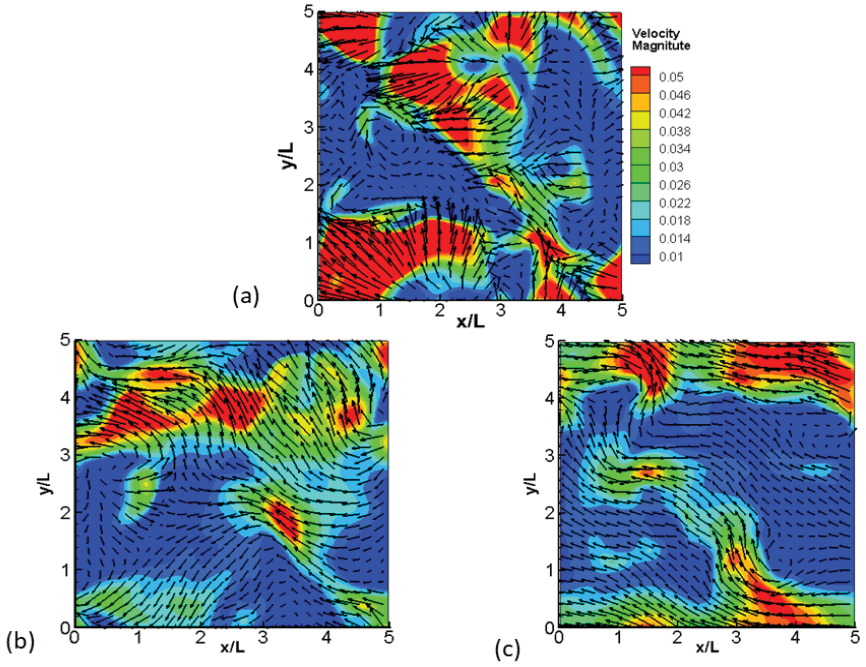

Fig. 5.12. Velocity vectors and magnitude (contours) at the interface of (*a*) $S1$, (*b*) $S3$ and (*c*) $S5$

Instantaneous concentration isosurfaces for $c_{Sc=4} = 0.5$ are shown in Figure 5.13 for simulations $S1$, $S2$ and $S4$. The surfactant concentration was normalised with the maximum instantaneous surfactant concentration γ_{max}, and the colours represent the normalised surfactant concentration at the corresponding (x, y) coordinates. The thickness of dynamic concentration boundary layer is affected by the isotropic turbulence diffusing from below. In general, strong upwelling and downwelling motions cause variation of the surfactant concentration at the water surface. The surfactants accumulate in the downwelling regions which can be identified by the increased thickness of concentration boundary layer. At the locations where the boundary layer is thin, surfactants are pushed to the side by strong upwelling motions. This is in agreement with what is shown in Figure 5.6, where the near surface turbulence (and hence the upwelling and downwelling motions) are damped with increasing levels of Ma/Ca_T.

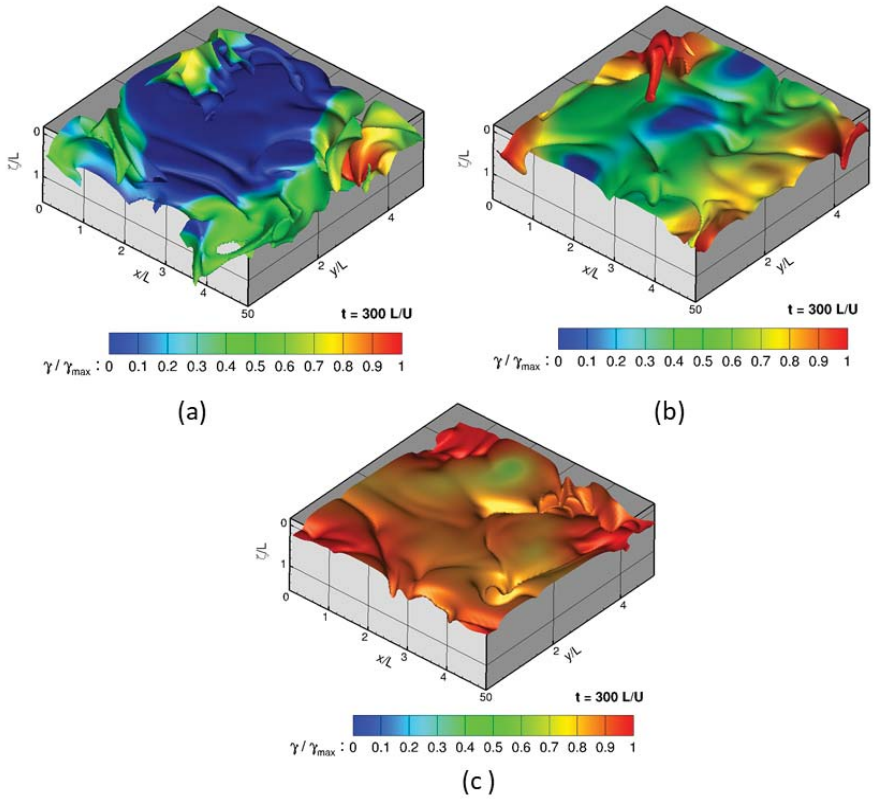

Fig. 5.13. Instantaneous isosurfaces of concentration at $c_{Sc=4} = 0.5$ from (a) $S1$, (b) $S2$ and (c) $S4$ $t = 300L/U$. The colour represent the normalised surfactant concentration at the corresponding interfacial (x, y) coordinates

Strong downwelling motions can penetrate deep inside the bulk, corresponding to the anti-splats observed for $S1$ in Figure 5.13 (a). Also, as a consequence of strong upwelling motions (splats) for low level Ma/Ca_T, large areas at the surface become virtually surfactant free. However, such surfactant-free areas quickly become smaller as the level of Ma/Ca_T increases, and finally completely disappear in simulation $S4$.

Figure 5.14 contrasts the correlation between the instantaneous concentration (colour contours) and the surface divergence (isolines), defined by

$$\beta = \left(\frac{\partial u}{\partial x} + \frac{\partial v}{\partial y} \right) |_{z=L_z} \tag{5.13}$$

in the grid plane adjacent to the surface of simulations $S1$ and $S5$. In $S1$, areas of

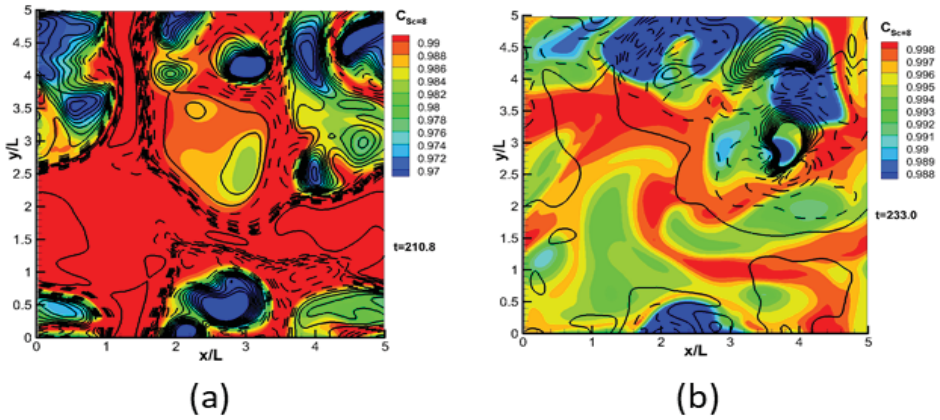

Fig. 5.14. Effect of increasing Ma/Ca_T on the correlation between the dissolved gas concentration (colour contours) and surface divergence (isolines). The solid and dotted lines correspond to positive and negative surface divergence, respectively. Snapshots are from (a) $S1$ and (b) $S5$.

low concentration coincide with strong positive surface divergence due to upwelling, while negative surface divergence (downwelling) is observed in areas with high concentration.

In contrast to this, in $S5$, the correlation between surface divergence and concentration levels is worse. Areas with strong positive surface divergence not always coincide with low concentration levels and vice versa. The reason for this is that in the simulations with large Ma/Ca_T (as in $S5$), strong Marangoni forces are generated that tend to reduce surface divergence and, hence, the correlation between β and c becomes worse than in simulations with low Ma/Ca_T, such as $S1$. Also, instantaneous shear stress is generated near the surface as can be seen in Figure 5.10 (see also Handler *et al.* [108]; Khakpour *et al.* [97]). Note that apparently the effects of instantaneous shear stresses in the high Ma/Ca_T simulations $S4$ and $S5$ resembles the effect of instantaneous shear in he no-slip case SN.

Figure 5.15 shows the effect of surfactant level on the surface divergence $\beta = (\partial u/\partial x + \partial v/\partial y)|_i$, which is related to 2D incompressibility of the interfacial velocity

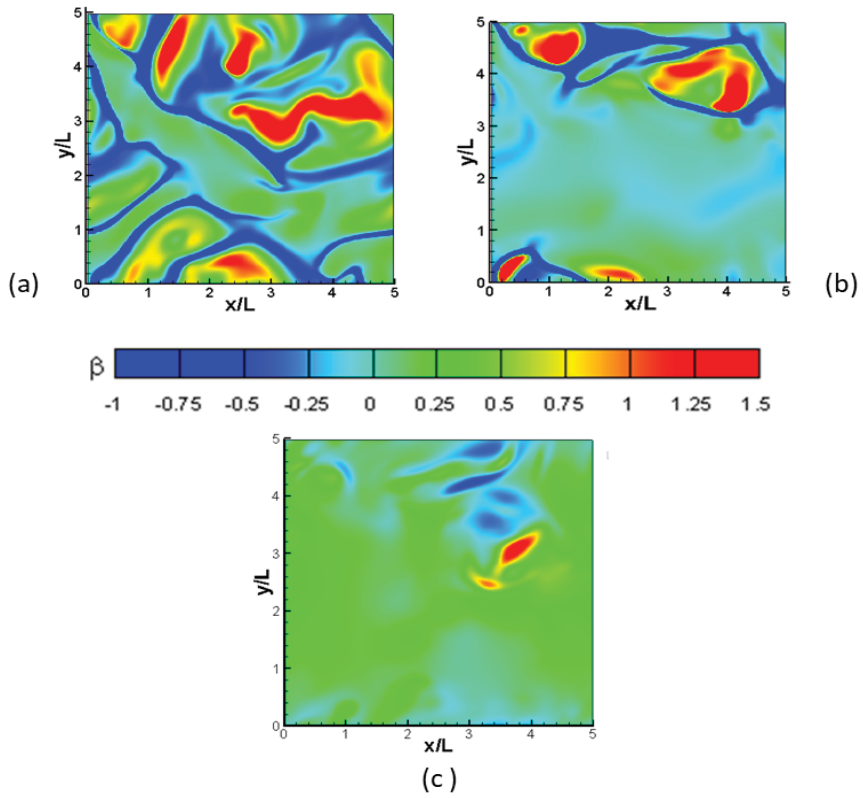

Fig. 5.15. Surface divergence for (a) $S1$, (b) $S3$ and (c) $S5$ at $t = 237L/U$

field. All three cases were evaluated at $t = 237.0L/U$. The red areas have positive surface divergence and coincide with up-welling of unsaturated fluid from the bulk towards the surface and the blue areas have negative β and correspond to the down welling of saturated fluid from the surface towards the bulk. Large values of $|\beta|$ indicate strong up and down-welling motions which typically correspond to high levels of gas transfer.

It can be seen that for $S1$, a relatively large variation in β is obtained which subsequently reduces with increasing Ma/Ca_T. Consequently, also β_{rms} will reduce and the vertical velocity immediately below the surface becomes progressively damped, because $\beta \to 0 \Rightarrow \frac{\partial w}{\partial z}\big|_i \longrightarrow 0$. This leads to a significant reduction of the interfacial gas transfer.

5.5.2 Effect of Ma/Ca_T on vertical mass transfer

To study the effect of Ma/Ca_T on mass transfer, vertical profiles of the average concentration together with the rms of its fluctuations and the diffusive and turbulent mass fluxes of simulations $S0$ - $S3$ and SN are shown in Figure 5.16. Note that the profiles for $S4$ and $S5$ are not plotted as they are very nearly the same as the SN profiles, indicating that even moderate levels of Ma/Ca_T manage to reduce mass transfer nearly as much as SN. Figure 5.16a depicts the normalised mean concentration profiles

$$\frac{\overline{\langle c \rangle} - \overline{\langle c_b \rangle}}{c_s - \overline{\langle c_b \rangle}}, \tag{5.14}$$

where c_b is evaluated in the bulk at $z = z_b$, chosen such that

$$c_{rms}(z_b) = 0.5 \max_{0 \le z \le l_z} (c_{rms}).$$

Increases in the contamination level were observed to lead to a thickening of the mean concentration boundary layer. The thickness δ of this layer can be identified by the depth where c_{rms} reaches its maximum. Figure 5.16b confirms that the peak in c_{rms} indeed moves further away from the surface with increasing Ma/Ca_T and the concentration boundary layer thickness δ gradually increases from 0.0239, 0.0273, 0.0345, 0.0424, 0.0487 for $S0$, $S1$, $S2$, $S3$, and SN, respectively. Furthermore, in general, the peaks in c_{rms} decrease with increasing surface contamination level with the exception of the peak in simulation $S0$. The comparatively large peak in $S1$ (compared to $S0$) is associated with increased vertical motions related to growing fluctuations in the surface divergence (β_{rms}) which is explained in more detail in Section 5.5.3

The total mass flux in the vertical direction is composed of the sum of the vertical diffusive and turbulent mass fluxes, $\langle \overline{D \frac{\partial c}{\partial z}} \rangle$ and $\langle \overline{c' w'} \rangle$, respectively. Because at the surface the vertical velocity is zero, diffusion fully dominates the vertical mass transfer at the surface. A decreasing concentration boundary layer thickness, associated with a reduction in Ma/Ca_T, results in steeper gradients of $\frac{\partial c}{\partial z}$ and, hence, an increased

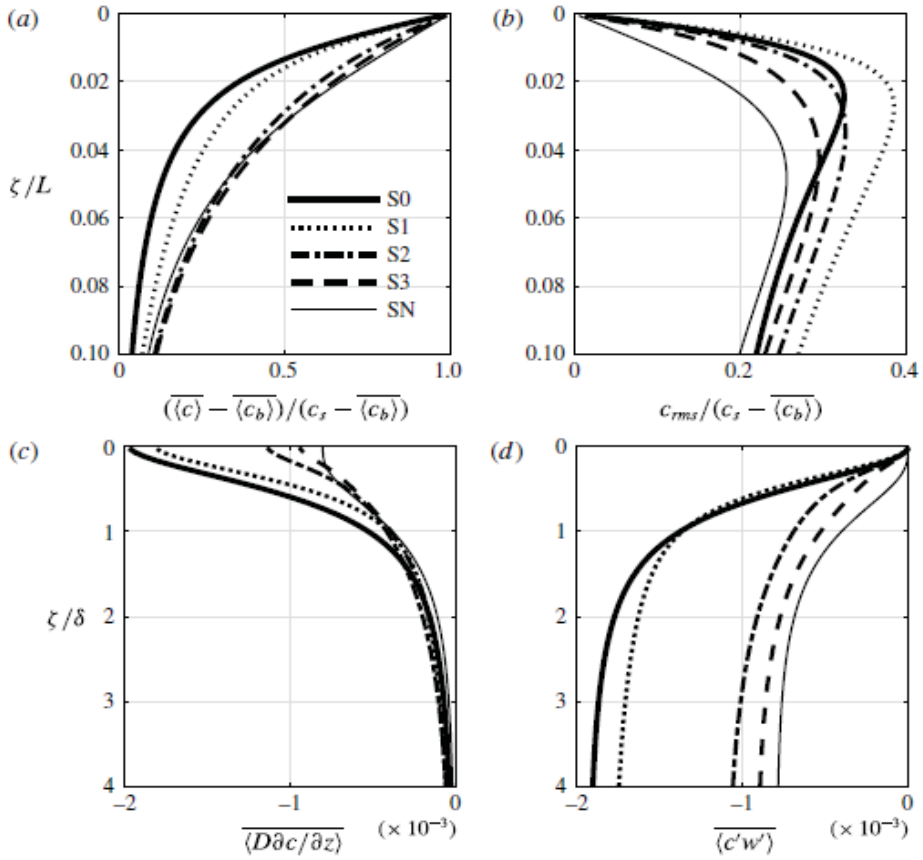

Fig. 5.16. Effect of Ma/Ca_T on the horizontally and time-averaged profiles of (a) normalised concentration, (b) normalised concentration fluctuations, (c) vertical scalar diffusion, (d) vertical turbulent scalar flux. In (c, d) the depth ζ is normalised using the boundary layer thickness. Note that the molecular diffusion coefficient D is defined by $D = 1/ReSc$

interfacial diffusive mass flux (see Figure 5.16c). Note that for the present no-slip simulation with $Re_T = 117$ this gradient (obtained at the surface) remains constant up to $\zeta/\delta \approx 0.2$. Hence, diffusion fully dominates mass flux not only at the surface but also immediately beneath. This observation is collaborated by the vanishing normal gradient of the scalar flux $\langle\overline{c'w'}\rangle$ shown Figure 5.16d. This results is a direct consequence of the fact that (1) $w' = 0$ at the surface and (2) the conservation of mass requirement for the no-slip simulation implies that $\frac{\partial w'}{\partial z} = 0$.

Because of the increased mixing due to turbulence, the diffusive mass flux can be seen to rapidly reduce with increasing distance from the surface. This decrease is balanced out be a simultaneous increase in the convective mass flux such that the total mass flux remains constant (see Figures 5.16c,d). The turbulent mass flux can be seen to virtually completely dominate the total mass flux at a depth of 3δ. In Figure 5.16d it can be seen that with increasing pollution levels, the turbulent mass flux tends to reduce.

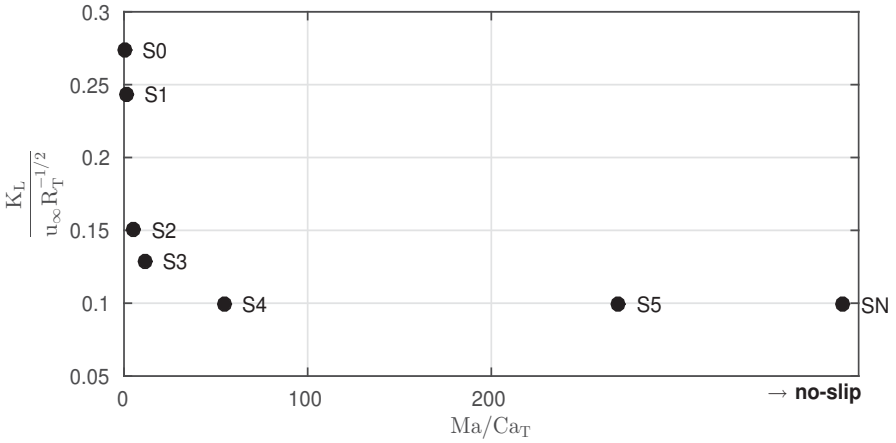

Fig. 5.17. Variation of K_L with Ma/Ca_T for $Sc = 32$

Figure 5.17 shows the effects of pollution, measured by Ma/Ca_T, on the mean gas transfer velocity K_L, as defined in Eq. (5.11). The figure shows that in the interval $Ma/Ca_T = 0$–11, the mean transfer velocity reduces very rapidly. As soon as $Ma/Ca_T \geq 54$, K_L becomes almost identical to the value obtained in the no-slip simulation $S0$. Note that because all Re_T are less than $Re_{T,crit} = 500$ (Theofanous *et al.* [19] ;Herlina & Wissink [10]) , the large-eddy regime rules apply and the K_L results, normalised by ${Re_T}^{-1/2}$, can be directly compared.

Figure 5.18 shows the evolution of the horizontally-averaged interfacial gas transfer velocity $k_L(t)$ for $S1$, $S3$ and $S5$ starting at $t = 200\ L/U$ until $t = 300\ L/U$. k_L was obtained using a Schmidt number of $Sc = 32$ and subsequently normalized by $u_\infty {Re_T}^{-1/2}$ and the bulk concentrations were assumed to be zero, see Eq. (5.11).

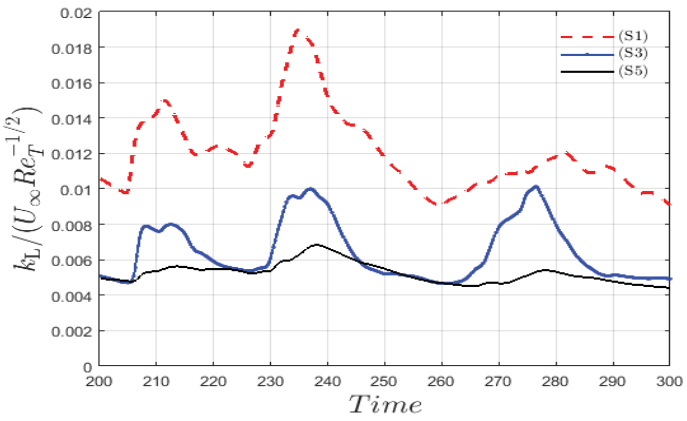

Fig. 5.18. Normalized horizontally-averaged gas transfer velocity k_L for $Sc = 32$ profiles (a) $S1$, (b) $S3$ and (c) $S5$

The horizontally-averaged gas transfer velocity was found to strongly depend on the contamination level. In $S1$, k_L was found to be significantly larger than in the other two cases with higher Ma/Ca_T. Contrasting the results obtained in $S3$ and $S5$ shows that at certain time-periods an almost identical transfer velocity was obtained while during other periods simulation $S3$ shows a significantly stronger increase in (k_L) than $S5$.

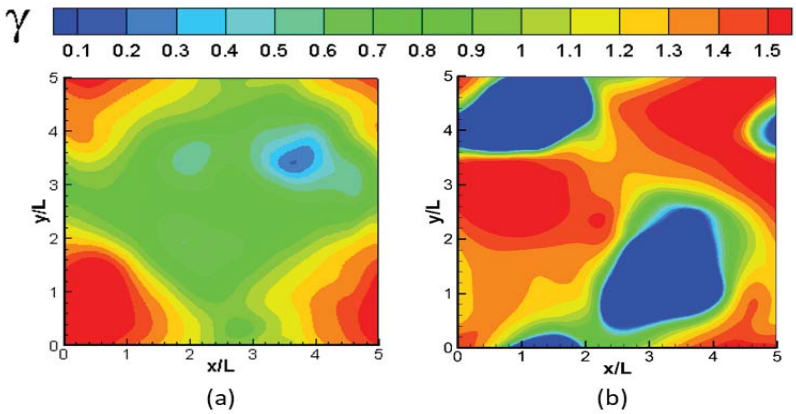

Fig. 5.19. Colour contours of surfactant concentration for $S3$ (a) for $t = 260L/U$, (b) $t = 276L/U$

This is further explored for case $S3$ ($Ma/Ca_T = 11$) in Figure 5.19 which shows snapshots of the surfactant concentration at the surface for $t = 260L/U$ and $t = 276L/U$, corresponding to a local minimum and maximum in k_L, respectively. It can clearly be seen that the larger value of k_L obtained at $t = 276L/U$ coincides with a relatively large area with a very low surfactant concentration (which is effectively clean). The low k_L obtained at $t = 260L/U$, on the other hand, corresponds to a very small clean area. Hence, we found evidence that the size of the clean area can be correlated with the horizontally-averaged gas transfer velocity.

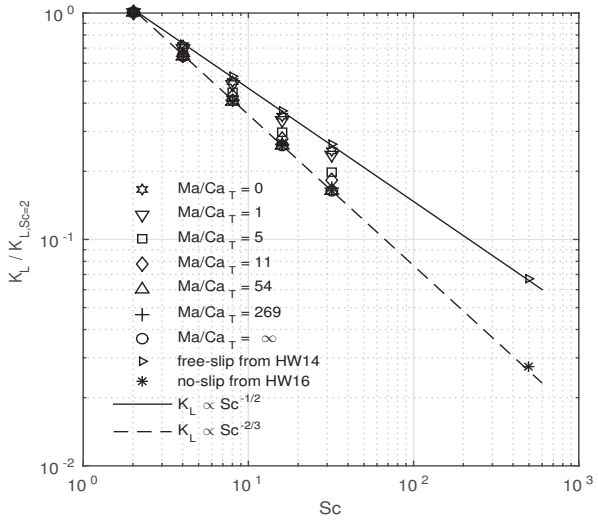

Fig. 5.20. K_L versus Sc for a range of Ma/Ca_T (see Table 5.1). HW14 and HW16 are taken from Herlina & Wissink [11] and Herlina & Wissink [10], respectively.

Figure 5.20 shows how $K_L/K_{L,Sc=2}$ changes with Schmidt number. The normalisation with $K_{L,Sc=2}$ was performed to ensure that both lines would fit nicely in the figure, it does not affect the scaling of $K_L \propto Sc^{-q}$ with Sc discussed here. It can be seen that, with increasing contamination level from $Ma/Ca_T = 0$ to 54, the power q gradually increases from 1/2 to 2/3, while beyond $Ma/Ca_T = 54$, q remains constant at 2/3 Herlina & Wissink (2014) [11] ($HW14$) and Herlina & Wissink (2016) [10] ($HW16$). In the aforementioned publications, the above scaling of the transfer ve-

locity with $Sc^{-1/2}$ and $Sc^{-2/3}$ for the free-slip and no-slip cases, respectively, was confirmed for Sc up to 500. Therefore, it is expected that also for cases $Ma/Ca_T > 0$ the obtained exponent q in $K_L \propto Sc^{-q}$ remains valid up to at least $Sc = 500$.

5.5.3 Surface divergence

An important model for the surface renewal rate r, is the so-called surface divergence model proposed by McCready *et al.* [13], which was discussed previously in Section 2.2.1.5. The model used the rms of the divergence of the horizontal velocity at the surface, see (2.11) and is defined by

$$K_L = c_\beta \sqrt{D\beta_{rms}}. \tag{5.15}$$

The importance of surface divergence model for interfacial gas transfer was shown in the study of McCready *et al.* [13]. Apart from this, the model was further verified using both experimental and numerical data e.g. McKenna & McGillis [47], Turney *et al.* [144], Magnaudet & Calmet [145], Kermani *et al.* [146], Wissink & Herlina [64] Herlina & Wissink [11]. These studies showed that the surface divergence model can produce high quality predictions of K_L. Unfortunately, the constant of proportionality c_β needed to be changed depending on the flow situation. In the numerical results obtained by Shen *et al.* [1], Khakpour *et al.* [97] and Hasegawa & Kasagi [135], it was found that increasing contamination levels cause a reduction in β_{rms}.

5.5.3.1 Qualitative observation of the relation between surface divergence beta and mass transfer velocity for various pollution levels

Here it is investigated for which level of surface pollution the surface divergence model for K_L begins to break down due to the increased damping of the surface divergence β_{rms}. Especially for large levels of contamination, this damping effect reaches to severe levels so that β_{rms} becomes virtually zero.

Colour contours of the instantaneous surface divergence were shown for the cases $S1$, $S3$ and $S5$ in Figure 5.15. Note that relatively large fluctuations in β were obtained in $S1$. However, with increasing Ma/Ca_T these fluctuations drastically reduce. Based on this it is save to assume that also β_{rms} will reduce. The latter is confirmed in Figure 5.21 where β_{rms} with increasing Ma/Ca_T can be seen to reduce

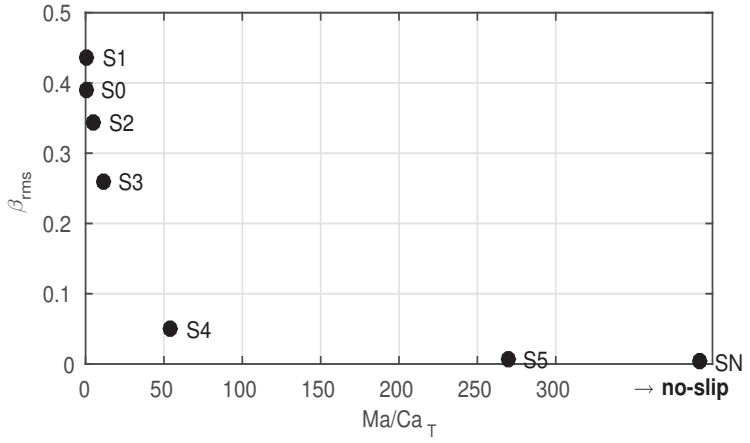

Fig. 5.21. Effect of increasing Ma/Ca_T on β_{rms}

to zero for large levels of pollution. Above it was shown that the surface divergence model can produce high quality predictions for K_L indicating that in the absence of pollution K_L is sensitively dependent on β_{rms}. As can be seen in Figure 5.21, β_{rms} reduces sharply towards zero within a very small Ma/Ca_T range. So that we can conclude that the surface divergence model may only be useful for surfaces with low to moderate levels of Ma/Ca_T. However, it will break down for β_{rms} close to the zero. This effect of contamination on β_{rms} was also studied previously by Shen *et al.* [1]

Note that β_{rms} in $S1$ is larger than in $S0$ (Figure 5.21) this unexpected result is likely related to over and underestimations in the surface divergence that are a result of large Marangoni forces suppressing strong up and downwellings. Because of the increased over and underestimations in $S1$ results in a slightly larger value for β_{rms} in $S1$ than in $S0$, one might expect that also K_L in $S1$ would be larger than in $S0$.

This, however, is not true. (see Figure 5.17). A likely explanation for this could be the presence of high intensity (but very localised) small scale structures in the β distribution of $S1$.

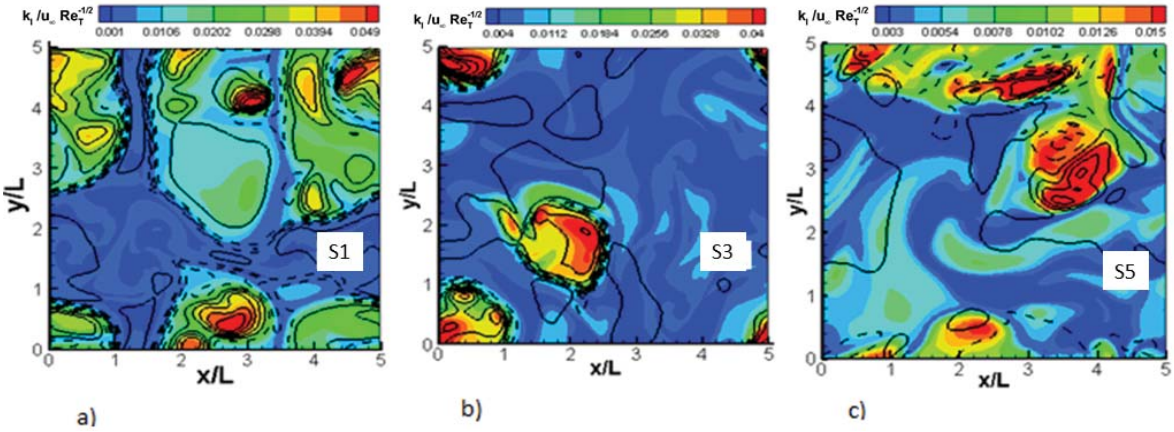

Fig. 5.22. Colour contours of $k_l/(u_\infty {Re_T}^{-1/2})$ combined with line contours of β , (a) $S1$, (b) $S3$, (c) $S5$

Contours of the local gas transfer velocity, k_l, combined with isolines of the surface divergence are shown for $Sc = 32$ in Figure 5.22. In the absence of surface shear (free-slip surface conditions), high values of k_l coincide with unsaturated flow washed up from the bulk, while low values of k_l correspond with saturated flow areas. However, the presence of surfactants induces instantaneous shear $(\frac{\partial u}{\partial z}, \frac{\partial v}{\partial z})$ near the surface causing a differential horizontal velocity between the surface and the flow immediately underneath. This leads to a non-uniform horizontal transport and explains the imperfect correlation between the instantaneous k_l and β as observed in Figure 5.22 (c), which shows that in the presence of surfactants high values of k_l do not always coincide with positive values of β and vice versa.

Figure 5.23 shows the evolution of the correlation $\rho(\beta, k_l)$ in time. It can be seen that for $S1$ the correlation is fluctuating about a value of 0.6, for $S3$ the correlation fluctuates about 0.2 and for $S5$ about 0. This result implies that the spatial correlation

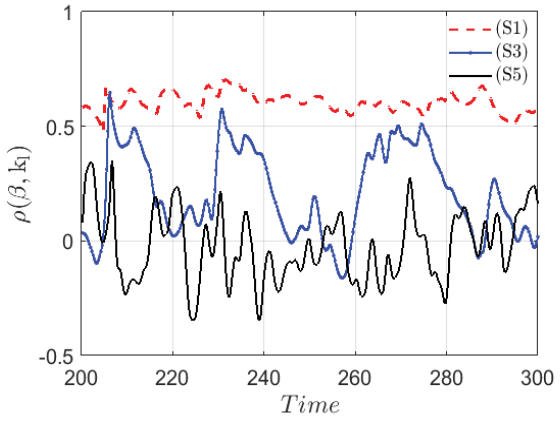

Fig. 5.23. Correlation of the instantaneous k_l and β in time

between the local instantaneous β and k_l deteriorates with increasing Ma/Ca_T. While for $S1$ the correlation is still quite strong, it is basically non-existent (zero) for $S5$. The latter implies that the surface divergence model is not so suitable to predict gas transfer in the presence of significant surface contamination.

Simulation	$\overline{\rho}(k_l, \beta)$	$\rho(k_L, \beta_{rms})$
$S1$	0.60	0.78
$S3$	0.21	0.93
$S5$	-0.02	0.30

Table 5.2
Correlation of the horizontally averaged k_L which is obtined for $Sc = 32$ and β over the final 100 time of the simulations

Table 5.2 shows the mean spatial correlation $\overline{\rho}(k_l, \beta)$ for $S1$ $S3$, $S5$ confirming the observations made in Figure 5.23. The temporal correlations $\rho(k_L, \beta_{rms})$ between the spatial fluctuations in surface divergence and the spatial average of k_l show a somewhat better correlation ranging from values of about 0.9 for $S1$ and $S3$ (which is very good) to a value of only 0.3 for $S5$, which confirms that the surface divergence

model (which uses β_{rms} to predict K_L) breaks down when the surface is severely contaminated.

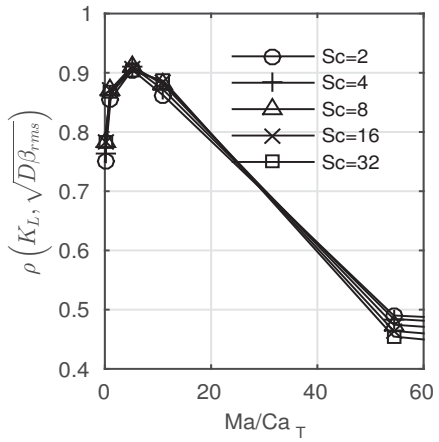

Fig. 5.24. Effect of increasing Ma/Ca_T on the correlation coefficient of K_L and $\sqrt{D\beta_{rms}}$

The validity of the surface divergence model for a shear free-surface boundary condition was checked by Herlina & Wissink [11], Wissink & Herlina [64] and Magnaudet & Calmet [145]. Furthermore, several researchers also determined the gas transfer velocity by using the surface divergence model for situations with surface shear (Law & Khoo [147], Banerjee & MacIntyre [49], Turney *et al.* [32])

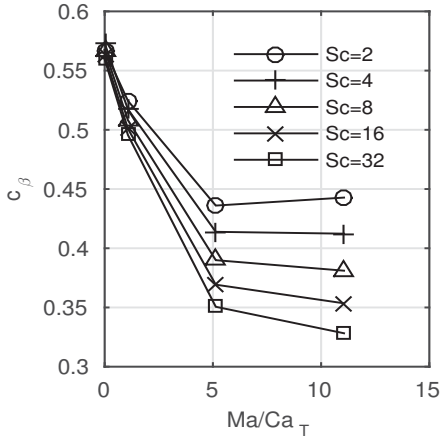

Fig. 5.25. Effect of increasing Ma/Ca_T on c_β

The variation of c_β with Ma/Ca_T is shown in Figure 5.25. The constant of proportionality c_β of the surface divergence model, defined in Eq. (5.15), needed to be reduced in order to represent the damping effect on K_L due to the presence of surfactants. For the cases with $Ma/Ca_T \leq 1$ the constant of proportionality was about 0.5 to about 0.58. For case $S2$ ($Ma/Ca_T \approx 5$), c_β decreases to 0.35 at $Sc = 32$. Hence, it can be concluded that for a prediction of K_L with the surface divergence model, each surface condition needs their constant of proportionality. Similar results were obtained in [47].

In agreement with Figure 5.20, Figure 5.25 also shows that a collapse of data points only occurs for very small values of surface contamination (Ma/Ca_T). This provides even more evidence that the surface divergence model is valid only for low to moderate levels of contamination and cannot be used to estimate K_L for higher levels of contamination.

5.5.4 Clean surface fraction ($\overline{\alpha}$)

The pollution parameter Ma/Ca_T was used to characterise the level of contamination at the water surface. The results indicated that for small levels of surfactants, large parts of the surface area become virtually surfactant-free. A model is proposed that predicts K_L from the surfactant-free (clean) fraction of the surface area $\overline{\alpha}$. Both the exponent (q) and the constant of proportionality c in (5.10), depend on the level of surface contamination and derivations are for both parameters are produced below. First we assume that

$$K_L = cSc^{-q} = \overline{\alpha}c_f Sc^{-q_f} + (1-\overline{\alpha})c_n Sc^{-q_n}, \tag{5.16}$$

with $q_f \leq q \leq q_n$, where q_f, c_f and q_n, c_n correspond to the exponents of Sc and the constant of proportionality for the free-slip and no-slip cases, respectively.
After substituting the Taylor expansions

$$Sc^{-q_f} = Sc^{-(q-h_1)} \approx Sc^{-q} + h_1(\ln Sc)Sc^{-q} + \bigcirc({h_1}^2), \tag{5.17}$$

$$Sc^{-q_n} = Sc^{-(q-h_2)} \approx Sc^{-q} - h_1(\ln Sc)Sc^{-q} + \bigcirc({h_2}^2). \tag{5.18}$$

After substituting the latter two expressions in Eq. (5.16), while ignoring second and higher order terms, we obtain

$$cSc^{-q} = [\overline{\alpha}c_f(1 + h_1 \ln Sc) + (1 - \overline{\alpha})c_n(1 - h_2 \ln Sc)]Sc^{-q} \tag{5.19}$$

and

$$c = \overline{\alpha}c_f(1 + h_1 \ln Sc) + (1 - \overline{\alpha})c_n(1 - h_2 \ln Sc) \tag{5.20}$$

because c is supposed to be independent of Sc, the non-constant $\ln Sc$ needs to be eliminated from this expression; by using $h_1 + h_2 = \frac{1}{6}$ or $h_1 = \frac{1}{6} - h_2$ we obtain

$$\overline{\alpha}c_f(\frac{1}{6} - h_2)\ln Sc - (1 - \overline{\alpha})c_n h_2 \ln Sc = 0 \Longleftrightarrow \overline{\alpha}c_f(\frac{1}{6} - h_2) = (1 - \overline{\alpha})c_n h_2, \tag{5.21}$$

and finally

$$h_2 = \frac{\frac{1}{6}\overline{\alpha}c_f}{(1 - \overline{\alpha})c_n + \overline{\alpha}c_f}, \tag{5.22}$$

$$q = \frac{2}{3} - h_2 \leftrightarrow q(\overline{\alpha}, c_f, c_n) = \frac{2}{3} - h_2(\overline{\alpha}, c_f, c_n), \tag{5.23}$$

$$c = \overline{\alpha}c_f + (1 - \overline{\alpha})c_n, , \tag{5.24}$$

where the exponents q_f and q_n are determined to be 1/2 and 2/3, respectively. The constants of proportionality c_f and c_n need be determined for free-slip and no-slip cases, respectively. Following that, the normalised gas transfer velocity $K_L/(u_\infty {Re_T}^{-r})$ can be calculated as a function of $\overline{\alpha}$.

5.5.4.1 Clean surface area

The flow near the contaminated surface is affected by horizontal gradients in the surfactant concentration as can be seen from

$$\left.\frac{\partial u_i}{\partial z}\right|_{z=L_z} = -\frac{Ma}{Ca}\frac{\partial \gamma}{\partial x_i} \qquad\qquad i = (1, 2).$$

These gradients generate Marangoni forces, of which the strength depends on Ma/Ca_T. The regions where the surfactant concentration is small are observed to reduce in size

with increasing Marangoni forces as can be seen in the instantaneous visualisations shown in Figure 5.26.

To establish whether part of a surface is clean or dirty, a threshold is defined for the surfactant concentration. The surfactant concentration was normalised by using the maximum instantaneous concentration of the surfactant γ_{max}. Hence, the clean surface fraction $0 \leq \alpha \leq 1$ is defined by the fraction of the total area where

$$\gamma/\gamma_{max} < \gamma_{th}. \tag{5.25}$$

The threshold of the surfactant concentration is represented by γ_{th}. The size of the

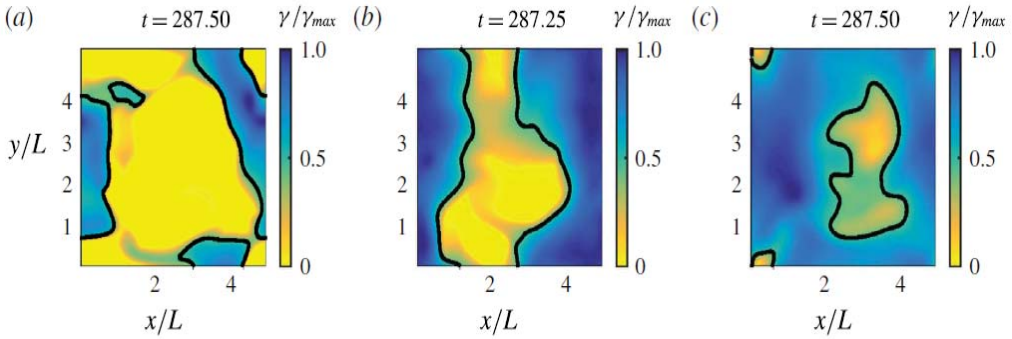

Fig. 5.26. Effect of increasing Ma/Ca_T on the 'surfactant-free' fraction of the total surface area. (a) $S1$, (b) $S2$, (c) $S3$. The solid black lines identify $\gamma/\gamma_{max} = 0.45$. Note that the purpose of these snapshots is only to give an impression of the effect of Ma/Ca_T on the surfactant-free area, the actual times are not important.

area where the surfactant concentration is reduced with increasing Ma/Ca_T can be seen in Figure 5.26. The figure also shows isolines of he threshold defined as $\gamma_{th} = 0.45$. In $S1$ the clean and dirty surface regions are separated clearly by steep gradients of the surfactant concentration. However, the separation of the clean and dirty surface regions is not very clear in $S2$ and $S3$, as the gradient becomes more diffuse with increasing contamination level (Ma/Ca_T). Simultaneously, the clean surface fraction α also steadily reduces in size.

Various thresholds $\gamma_{th} = 0.1, 0.3, 0.45$ and 0.70 were used to establish the relation between the time-averaged clean surface faction $\overline{\alpha}$ and Ma/Ca_T in Figure 5.27. For cases $S0$ to $S3$ with $Ma/Ca_T < 11$, a sharp reduction is obtained in $\overline{\alpha}$ with a

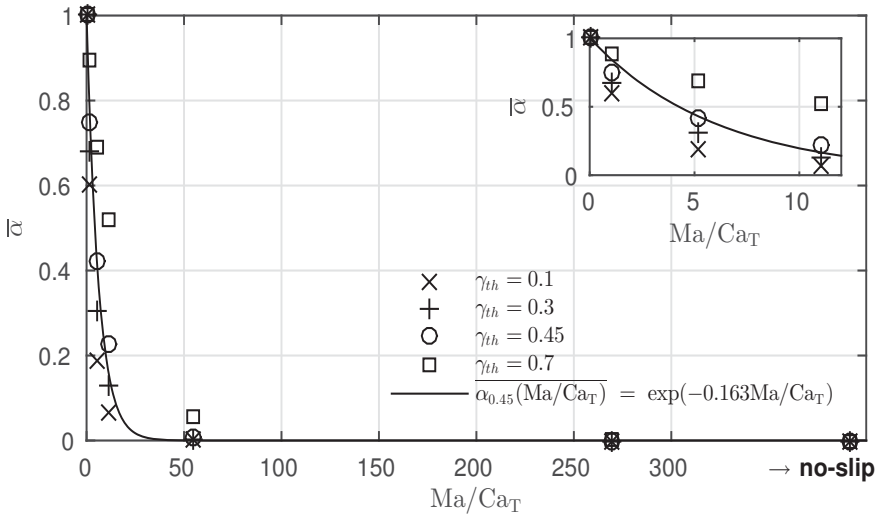

Fig. 5.27. Variation of clean surface fraction $\overline{\alpha}$ with Ma/Ca_T

only slight increase in contamination level. However, for severely contaminated cases ($Ma/Ca_T \geq 54$) the clean surface fraction $\overline{\alpha}$ was found to be virtually zero. Furthermore, the variation of $\overline{\alpha}$ with Ma/Ca_T can be reasonably well represented by an exponential relationship. Using the least squares method, for $\gamma_{th} = 0.45$ the best fit was found to be

$$\overline{\alpha_{\gamma_{th}}} = \overline{\alpha}_{0.45} = e^{-0.163 Ma/Ca_T} \tag{5.26}$$

5.5.4.2 Correlation between clean surface fraction α and gas transfer velocity k_L

In the absence of pollution ($Ma/Ca_T = 0$), the clean boundary at the surface is modelled using a free-slip boundary condition, corresponding to $\alpha = 1$ (simulation $S0$). For an extremely polluted surface, the covering with surfactants will be complete at all times so that the clean surface fraction becomes $\alpha = 0$. Even for moderate values

of Ma/Ca_T, as in simulations $S5$ and also $S4$, α was found to be almost zero when using a surfactant threshold of $\gamma_{th} \leq 0.5$. Consequently, the instantaneous transfer velocity in $S5$ and $S4$ is likely to scale the same as when using the no-slip boundary conditions, where $K_L \propto Sc^{-2/3}$. This is in agreement with the scaling of the time-average K_L values shown in Figure 5.20.

		$\rho(k_L, \alpha_{\gamma_{th}})$					
Run	Ma/Ca_T	$\gamma_{0.1}$	$\gamma_{0.2}$	$\gamma_{0.3}$	$\gamma_{0.4}$	$\gamma_{0.5}$	$\gamma_{0.6}$
$S1$	1	0.7543	0.7391	0.6802	0.6060	0.5030	0.4151
$S2$	5	0.8466	0.7795	0.6864	0.5808	0.4707	0.4089
$S3$	11	0.9568	0.9497	0.9045	0.7738	0.4182	0.0696

Table 5.3
Correlation coefficients at $Sc = 32$ for various thresholds $\alpha_{\gamma_{th}}$

The instantaneous clean surface fraction (α) was found to have a significant effect on the instantaneous gas transfer velocity (k_L) for cases $S1$, $S2$ and $S3$. Table 5.3 shows the correlation coefficient $\rho(k_L, \alpha_{\gamma_{th}})$ of the instantaneous gas transfer velocity k_L and the instantaneous clean surface fraction α obtained at $Sc = 32$ for $\gamma_{th} = 0.1 - 0.6$. It can be seen in Table 5.3 that the instantaneous transfer velocity is very strongly correlated with $\alpha_{\gamma_{th}}$ for $\gamma_{th} = 0.1$. In general, it was found that the correlation decreases with increasing γ_{th}. Furthermore, it can be seen that for $\gamma_{th} < 0.4$, the correlation increases with the level of contamination, while for $\gamma_{th} > 0.4$ the correlation decreases with the level of contamination.

The time-evolution of $\alpha_{\gamma_{th}}$, k_L and $-q$ obtained using the horizontally averaged instantaneous concentration profiles from simulation $S2$ are shown in Figure 5.28. In general, it can be seen that when α decreases (small clean surface fraction so that almost the entire interface is covered with surfactant), the power q gets larger and approaches a value of 2/3, that corresponds to very high levels of surfactant pollution. In contrast, q generally decreases and moves towards the clean surface value $q = 1/2$

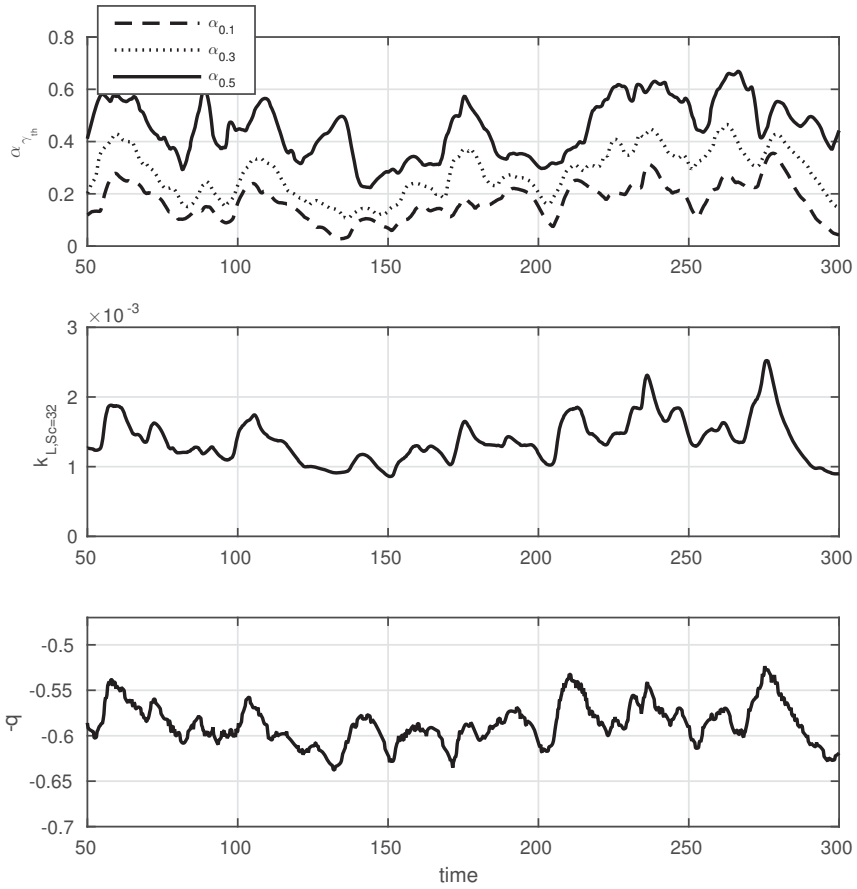

Fig. 5.28. Time series of the clean surface fraction (upper pane), the instantaneous gas transfer velocity k_l (middle pane) and the power coefficient $-q$ (lower pane)

when the clean surface fraction (α) increases. Also, it can be seen that a (positive) correlation exists between $\alpha_{\gamma_{th}}$ and k_L which becomes slightly worse with increasing threshold (because for increasing threshold the clean surface area becomes less and less "clean"), which is in agreement with the results presented in Table 5.3.

5.5.4.3 Comparison between observed mean q, c and K_L with their prediction based on α

Table 5.3, displays the temporal correlation between various $\alpha_{\gamma_{th}}$ and k_L for the cases $S1$, $S2$ and $S3$ obtained at $Sc = 32$. The very good correlation obtained for $\alpha_{0.1}$, however, does not necessarily mean that the actual prediction of the magnitude of the normalised gas transfer velocity

$$\frac{K_L}{u_\infty {Re_T}^{-1/2}}(\overline{\alpha}) = c(\overline{\alpha}){S_c}^{-q(\overline{\alpha})}, \tag{5.27}$$

where $c(\overline{\alpha})$, $-q(\overline{\alpha})$ are defined in Eq. (5.24) and (5.23), is correct using the DNS results (obtained at various Sc numbers simultaneously), for each Ma/Ca_T case the power q and the constant of proportionality c in the equation above can be estimated using the least squares method. The results obtained estimating $-q$ and c are shown in Figures 5.29a) and b), respectively, for a range of (Ma/Ca_T). Smooth variations are observed for both parameters. The exponent $-q$ reduces from $-1/2$ to $-2/3$ with increasing (Ma/Ca_T). Simultaneously, c reduces from $c \approx 1.55$ to $c \approx 0.94$ when (Ma/Ca_T) increases from 0 to beyond 50. To determine the clean surface fraction $\overline{\alpha}$ in Eqs: (5.23) and (5.24) from the numerical results, first the optimum threshold γ_{th} needs to be determined. To achieve this, we need to minimize the sum of the squared errors

$$SSE(\overline{\alpha_{\gamma_{th}}}) = \sum_{S0}^{SN} \left[K_L - K_L(\overline{\alpha_{\gamma_{th}}})\right]^2, \tag{5.28}$$

where K_L is the reference value calculated directly from the numerical results and the predicted gas transfer velocity, $K_L(\overline{\alpha_{\gamma_{th}}})$ is calculated by using Eqs: (5.23), (5.24) and (5.10). The parameters of $c_f = 1.55$ and $c_n = 0.94$ were determined from the results of $S0$ (free-slip) and SN (no-slip) in [11] and [10], respectively. $r = 1/2$ in Eq. (5.10) was assumed due to the low to moderate intensity levels of the turbulence in the simulations.

Figure 5.30 shows the effect of the threshold γ_{th} on the sum of squared errors, SSE. The threshold was varied from $\gamma_{th} = 0.1$ to 0.5 in order to estimate the minimum SSE.

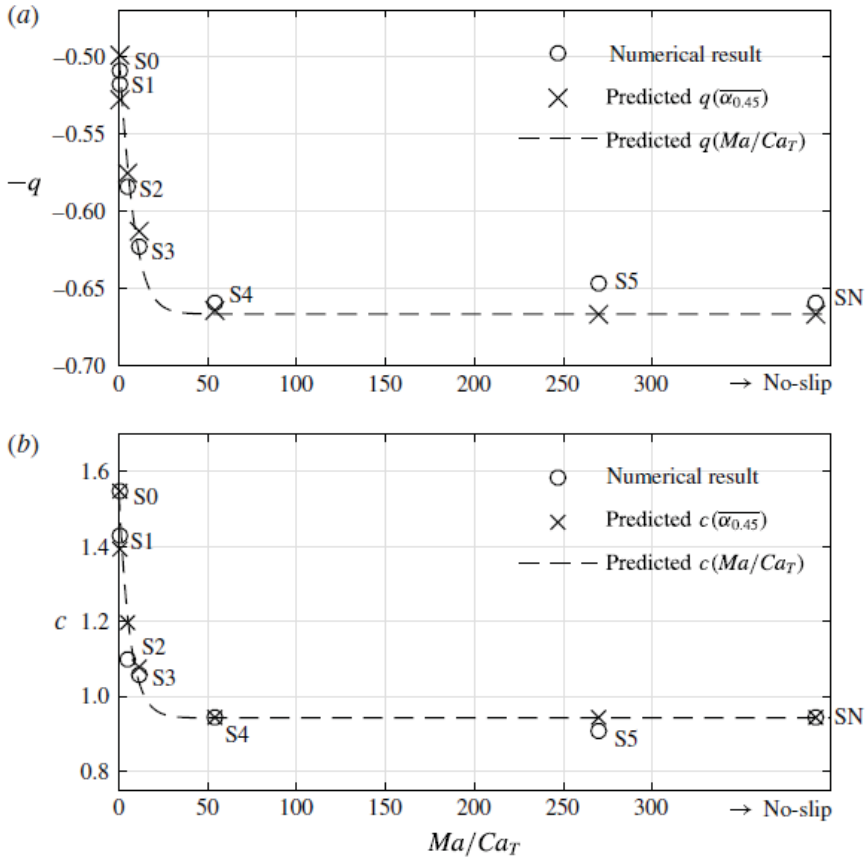

Fig. 5.29. Variation of (a) the exponent $-q$ and (b) the constant of proportionality c with (Ma/Ca_T). The results are averaged from $t = 150$ to $t = 300$.

While for small threshold values the temporal correlation $\rho(k_L, \alpha_{0.1}\gamma_{th})$ was relatively high, the smallest SSE was obtained for a larger γ_{th} between 0.4 and 0.5. Note that for smaller γ_{th}, $K_L = \overline{k_L}$ was significantly underestimated. In the remainder, unless specified differently, a threshold of $\gamma_{th} = 0.45$ was used for the determination of $\overline{\alpha}$.

To test the quality of our predictions for q and c, using $\overline{\alpha_{0.45}}$, in Figure 5.29 the predicted data points are shown alongside the numerical results. It can be seen that a reasonably good agreement was obtained (error in $|q|$ less than 0.025 and the error in $|c|$ less than 0.1). In addition, the dashed line, which was produced using the

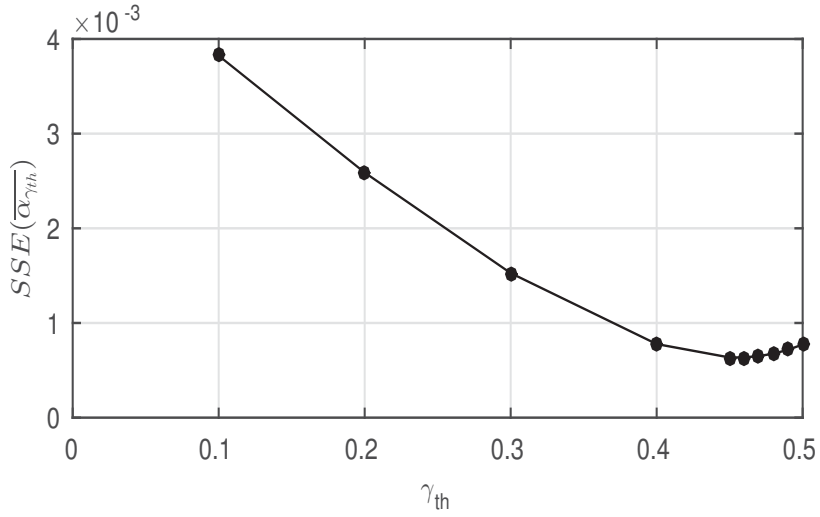

Fig. 5.30. The sum of squared errors defined in Eq. (5.28)

exponential relationship (5.26) between Ma/CaT and $\overline{\alpha_{0.45}}$, which provides a good interpolation between the data points.

Finally, the prediction given above for q and c, leads us to expect that the proposed model based on the clean surface fraction also provides a reasonable prediction of at least similar quality for the transfer velocity. This is indeed confirmed in Figure 5.31, illustrating that the calculation of the normalised transfer velocity from Eq. (5.27) both (i) directly by employing the observed $\overline{\alpha_{0.45}}$ so that

$$\frac{K_L}{u_\infty Re_T^{-1/2}}(\overline{\alpha_{0.45}}), \tag{5.29}$$

and (ii) indirectly by using (5.26), where $\overline{\alpha_{0.45}}$ is estimated as a function of Ma/Ca_T, giving

$$\frac{K_L}{u_\infty Re_T^{-1/2}}(Ma/Ca_T) = \frac{K_L}{u_\infty Re_T^{-1/2}}(\overline{\alpha_{0.45}}(Ma/Ca_T)), \tag{5.30}$$

agree well with the normalised transfer velocity K_L that was directly calculated from the numerical data. In particular, the rapid reduction in K_L for small values of Ma/Ca_T is reproduced as is the smooth transition from K_L values that are typical for clean conditions to those typical for very dirty conditions.

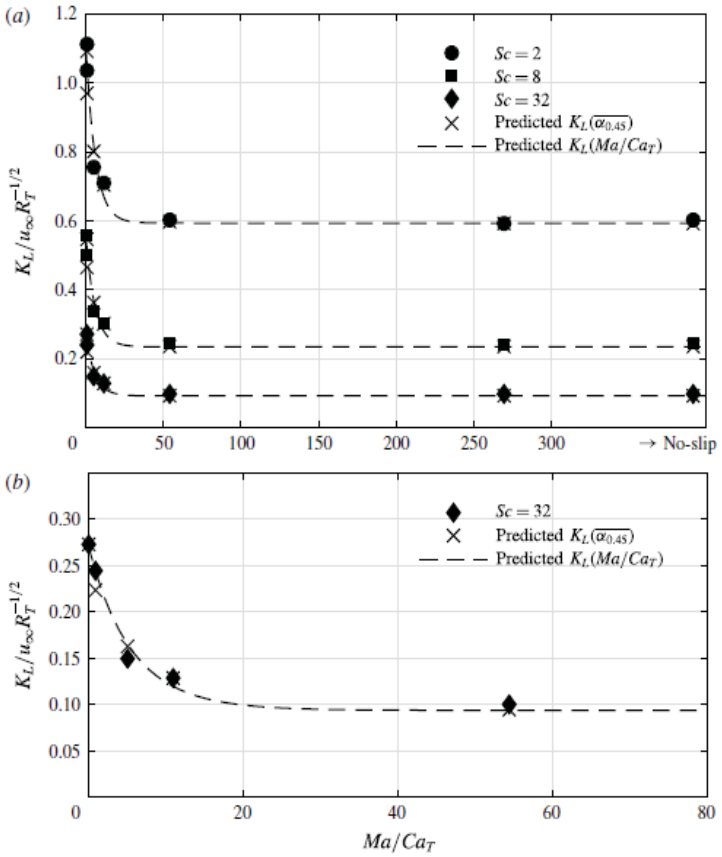

Fig. 5.31. Comparison of the predicted K_L with the K_L calculated directly from the numerical results for various levels of contamination Ma/Ca_T. (a) Results obtained for $Sc = 2$, 8, 32, (b) close up of $Sc = 32$ results for low to moderate Ma/Ca_T .

Chapter 6: Effect of slip-length on the interfacial mass transfer

6.1 Introduction

The transfer velocity, K_L, of atmospheric gasses towards the bulk of the water is largely controlled by the hydrodynamic condition at the water side, where it may be affected by a wide range of environmental variables. For a fluid flowing parallel to a boundary, the viscous boundary layer is a thin layer in which the velocity of the fluid rapidly adjusts to the velocity of the wall (boundary) therefore generating mean shear. In our case, the isotropic turbulence has zero mean shear but is damped towards the surface. Hence, a viscous boundary layer would only be visible in the rms (root-mean-square) plot of the horizontal velocity. A very important boundary layer in our simulation is the concentration boundary layer in which the concentration of dissolved atmospheric gases changes from its bulk value to the fully saturated state reached at the surface. The surface hydrodynamic condition is affected, for instance, by cleanliness of the water (e.g. presence of surfactants).

If the water surface is completely clean, the tangential stress vanishes due to the absence of forces at the surface. Hence, the normal gradient of the horizontal velocity components becomes zero (free-slip condition). That is: $\frac{\partial u}{\partial z} = \frac{\partial v}{\partial z} = 0$, while the vertical velocity w becomes virtually zero because of surface tension. Hence, both

the bottom and the top boundary have zero mass flux [97]. However, if contamination is present tangential stresses will occur because of the generation of Marangoni forces due to variations in surfactant concentrations. The reason for this is that surface tension reduces with increasing surfactant concentrations. As a result, near surface turbulent velocity fluctuations are damped [148]. As shown in Chapter 5, the surfactant contamination of the water surface is measured by the ratio between Marangoni number and turbulent capillary number, $\frac{Ma}{Ca_T}$ [149]. We aim to model this near-surface-turbulence damping by surfactants by prescribing a finite slip-length λ, ranging from no-slip conditions ($\lambda = 0$) to free-slip conditions (corresponding to $\lambda = \infty$).

The effect of slip-length on the interfacial gas transfer of atmospheric gasses into water was investigated performing Direct Numerical Simulations. The interfacial gas transfer mechanism is driven by isotropic turbulence diffusing from below. The model proposed here aims to relate the slip-length surface boundary condition to the surfactant contamination level. In other words, we aim to find a relation between λ and Ma/Ca_T for a range of Schmidt numbers Sc. Simulations were performed at various slip-lengths, including the free-slip and no-slip boundary conditions. For $Sc = 4, 8, 32$, the gas transfer velocity K_L was determined as a function of slip length and subsequently compared to previous DNS results in which K_L was determined as a function of Ma/Ca_T.

When using a finite slip length, the turbulence damping near the surface differs from the damping owing to surfactant-induced Marangoni forces. Increasing Ma/Ca_T will progressively reduce the horizontal divergence of the near surface flow, but will still allow the horizontal velocities to remain non-zero. Decreasing the slip-length at the surface, however, progressively reduces the actual magnitude of the horizontal velocities. Still, the scaling of K_L with $Sc^{-2/3}$, which is typical for heavily contaminated surfaces, is found both at very large Ma/Ca_T and at $\lambda = 0$. Also, for clean surface conditions (free-slip boundary conditions) where $Ma/Ca_T = 0$ and $\lambda = \infty$, K_L scales with $Sc^{-1/2}$. Previously, when studying the effects of surfactants, a smooth

transition of the power q in the scaling $K_L \propto Sc^q$ was found from $q = -1/2$ for clean conditions to $q = -2/3$ for very dirty conditions [149]. Here it is investigated whether a similar smooth transition of q can be found when reducing the slip length λ from ∞ to 0.

The purpose of finding this correlation between pollution level and slip-length is mainly to facilitate modelling. By replacing surface pollution by a simpler boundary condition, computational time can be saved as there is no need to explicitly solve an additional $2D$ convection-diffusion equation for the surfactant every time step. A finite slip length is used as a modelling tool by various researchers who need a boundary condition "between no-slip and free-slip". For instance, when modelling the flow of liquid on superhydrophobic surfaces. Philip & John [150], [151] investigated the flow in a pipe of radius R with stripes (grooves) parallel to the flow. Here, the pipe surface was modelled by identifying no-slip and free-slip regions modelled by a slip-length of

$$\lambda = \frac{L}{\pi} \ln \left[\frac{1}{\cos(\alpha_g \frac{\pi}{2})} \right] \tag{6.1}$$

for $Re \to \infty$, where α_g is the gas (free-slip) fraction area and L is the size of the surface structure. Lauga & Stone [152] proposed a slip-length model for a smooth hydrophobic surfaces in a pressure-driven Stokes flow with grooves perpendicular to the flow direction, where

$$\lambda = \frac{L}{2\pi} \ln \left[\frac{1}{\cos(\alpha_g \frac{\pi}{2})} \right]. \tag{6.2}$$

A semi-analytical calculation was also used by Ybert *et al.* [153] to find the effective slip-length. They calculated the effective slip-length using the proportion of the surface area with zero slip-length, which they referred to as the solid fraction α_s. Their model reads

$$\lambda_{eff} = \left(\frac{\delta_v}{\ell^2} + \frac{1}{\lambda_{ideal}} \right)^{-1}, \tag{6.3}$$

where $\lambda_{ideal} = \ell(\frac{0.325}{\sqrt{\alpha_s}} - 0.44)$, δ_v is the viscous penetration depth and ℓ is the typical length scale of the gas area. Davis *et al.* [154] performed an analytical calculation to express the effective slip-length on a superhydrophobic surface by introducing strong

drag reduction terms. Various experimental techniques were used to measure slip-length on a superhydrophobic surface. Particle image velocimetry (PIV), Pressure-drop, Surface force apparatus (SFA), atomic force microscope (AFM) measurements are some of the measurements techniques used. Choi & Kim [155] used a cone and plate rheometer system to work with a superhydrophobic surface, where they minimised the contact area of the liquid and the solid. Slip-lengths of the surface were obtained around 20 and 30 μm for water and glycerine, respectively. However Bocquet *et al.* [156] found that the experiments of Choi & Kim [155] contained significant uncertainty regarding the slip-length of the superhydrophobic surface, which had a magnitude ranging from $20 - 100$ micrometers.

Priezjev & Nikolai [157] studied the slip-length between a fluid surface and a solid wall by performing molecular dynamics simulations of micro- and nano-channel flows confined between atomically smooth surfaces. They investigated the influence of shear rate and surface energy on the slip-length. They found that when the shear rate increased the slip-length did not increase in a linear way. They modelled the slip-velocity and slip-length as a function of the shear rate by $\frac{\partial v}{\partial z}(-h) = \frac{V_S}{\lambda}$, where V_S is the slip velocity at the wall and v is the wall-parallel velocity.

6.2 Overview of the simulations

The problem under consideration is the effect of limited slip-length on the interfacial gas transfer in a turbulent water environment driven by isotropic turbulence diffusing from below. DNS calculations were employed to study the effect of such a boundary condition for the velocity on the interfacial mass transfer. The isotropic turbulence was generated in a separate large-eddy simulation in a cubic domain with periodic (cyclic) boundary conditions in each direction. The LES was run in parallel with the DNS using the same time step. Every time step instantaneous flow in an (x, y) cross-section of the LES domain is used as a boundary condition at the bottom of the DNS calculation. The periodic boundary conditions used in the LES are needed

to obtain a isotropic flow used as a computationally inexpensive model for "real-life" turbulence. In the DNS periodic conditions were only employed in the horizontal directions.

As can be seen in Figure 6.1, the computational domain consists of two parts. The upper part shows the computational domain of the DNS, while the LES is calculated in the lower (cubic) domain. The sizes of the 3D LES and DNS computational domains are the same as the ones employed in the simulations presented in Chapter 5.1. The

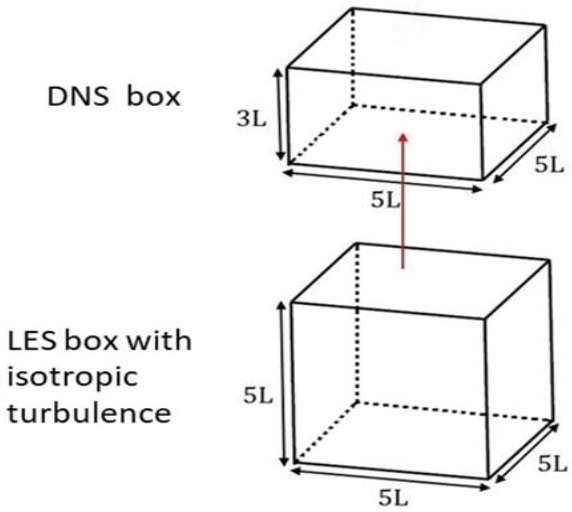

Fig. 6.1. Computational domain

$2D$ numerical simulation, used to calculate the evolution of the surfactant at the surface in Chapter 5, is absent from the present set-up because of the change in upper boundary condition where the influence of surfactants is modelled by a finite slip-length at the surface.

In the DNS calculations the mesh was stretched in the z-direction to achieve a finer mesh towards the surface and a total of $128 \times 128 \times 212$ grid points was used to resolve the flow inside the $L_x \times L_y \times L_z = 5L \times 5L \times 3L$ domain. For the LES a coarser $64 \times 64 \times 64$ mesh with a domain size of $L_x \times L_y \times L_z = 5L \times 5L \times 5L$ was used. To model the subgrid scale stresses, the standard Smagorinsky model was employed with a Smagorinsky constant of $C_S = 0.22$. In the LES, both the isotropy and a turbulence

level of $Tu = 0.40\,U$ were maintained by rescaling the velocity fluctuations each time step.

After a transient period starting from $t = 0$ to $t = 300\,L/U$ the turbulence in the DNS (and LES) calculations was found to be fully developed. All simulations were subsequently run for a further 300 time-units to gather turbulence statistics. In both DNS and LES, a Reynolds number of $Re = \frac{UL}{\nu} = 600$ - based on a characteristic length-scale of $L = 0.01$ m, a kinematic viscosity of $\nu = 10^{-6}m^2/s$ and a velocity scale of $U = 0.06$ m/s - was employed. The mass transfer calculation in the DNS was performed for Schmidt numbers $Sc = 4, 8$ and 32.

The vertical z coordinate points upwards with $z = 0$ corresponding to the bottom of the computational domain. At times it is more convenient, however, to plot quantities against the distance to the surface defined by $\zeta = L_z - z$, where $L_z = 3\text{“}L$ is the height of the computational domain. Note that the integral length scale L_∞ and characteristic turbulent velocity scale u_∞ are assessed at the same location $\zeta = L$, while the turbulent Reynolds number is defined by Eq. (5.6).

The DNS and LES meshes were the same as those used in previous simulations [11], [149]. The mesh density was shown to provide a good resolution of both the turbulent flow and the mass transfer.

Ten simulations were performed with varying slip-lengths $\lambda = 0$, 0.001, 0.01, ..., 0.5, 2.0, ∞ (see Table 6.1). Note that the free-slip and no-slip simulations are identical to the ones presented in [149]. The turbulent velocity and length scales, reported in Table 6.1, are extracted at a distance of one-L from the surface.

The concept of finite slip-length is explained in Figure 6.2, showing a grooved surface. The lower part of the surface shown shows ridges of width a that are in direct contact with water. The grooves of width b, on the other hand, are filled with air and provide an almost stress-free interface. The combined area of the ridges can be modelled using a no-slip interface, whilst the combined area of the grooves corresponds to a free-slip interface.

Run	λ/L	u_∞/U	L_∞/L	Re_T
S0	0.0	0.107	0.898	117
S1	0.001	0.104	0.940	118
S2	0.01	0.111	0.911	121
S3	0.02	0.111	0.894	119
S4	0.05	0.111	0.929	124
S5	0.1	0.114	1.002	137
S6	0.2	0.113	1.004	136
S7	0.5	0.116	1.026	143
S8	2.0	0.113	1.076	163
SN	∞	0.113	1.033	141

Table 6.1
Overview of the simulations, L_∞, u_∞ are the turbulent length and velocity scales defined by Eq. (5.5), λ is the slip-length and Re_T is the turbulent Reynolds number defined by Eq. (5.6).

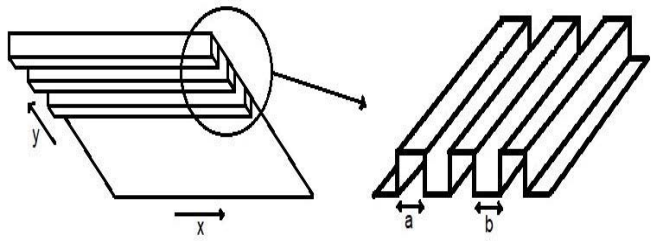

Fig. 6.2. Schematic of surface structure showing ridges and grooves to represent areas of the surface which are (ridges) and are not (grooves) in direct contact with water

The ratio of the total area accupied by grooves b to the entire surface area of the plate corresponds to the clean surface fraction ($\overline{\alpha}$) which is mentioned in the previous work [149] and Section 5.5.4.1. Two extreme cases can be identified:

1. $\overline{\alpha} = 0$ corresponding to all the grooves having zero width ($b = 0$), modelled using a no-slip interface, $\lambda = 0$.

2. $\overline{\alpha} = 1$ corresponding to all the ridges having zero width ($a = 0$), modelled using a free-slip interface, corresponding to $\lambda = \infty$

Based on this the clean surface fraction $\overline{\alpha}$ is defined by ($\overline{\alpha} = \frac{b}{a+b}$).

6.2.1 Slip-length boundary condition

As mentioned in the introduction, the focus of this chapter is to try and use a finite slip-length boundary condition as a model for surface contamination. The slip-length is defined as the distance to the surface where the extrapolated horizontal velocity becomes zero. The horizontal velocities at the surface are subsequently determined by using linear extrapolation of the corresponding velocities adjacent to the surface inside the computational domain, (see Figure 6.3).

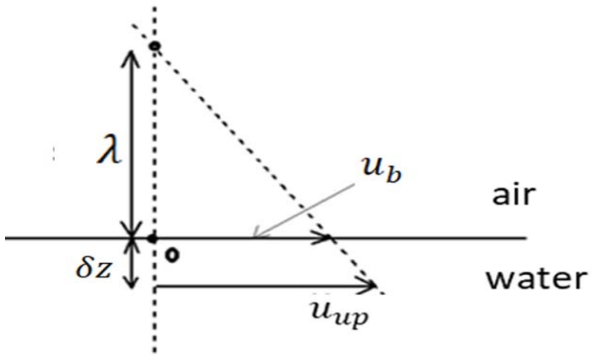

Fig. 6.3. Schematic of the slip-length definition, δz is the distance to the surface of the locations where the upper horizontal velocities are defined, λ is slip-length.

Figure 6.3 shows how the boundary condition for the horizontal velocities at the surface is determined. Using the distance δz between the surface and the surface-

nearest grid-plane where the upper horizontal velocities u_{up} are defined, the corresponding surface-boundary-condition u_b is obtained from

$$u_b = \frac{\lambda}{\lambda + \delta z} u_{up}. \tag{6.4}$$

The vertical velocity at the surface is set to $w = 0$ and (as mentioned earlier) periodic boundary conditions were used in the horizontal directions of the DNS domain to reflect a much larger size that is generally used in experiments. At the bottom of the DNS, the isotropic turbulence that was introduced was generated in a separate LES of isotropic turbulence in a periodic box. To allow a time-accurate turbulent boundary condition for the DNS.

6.3 Results

6.3.1 Effect of slip-length on the near-surface turbulent flow

Figure 6.4 shows the root-mean-square of the horizontal and vertical velocities

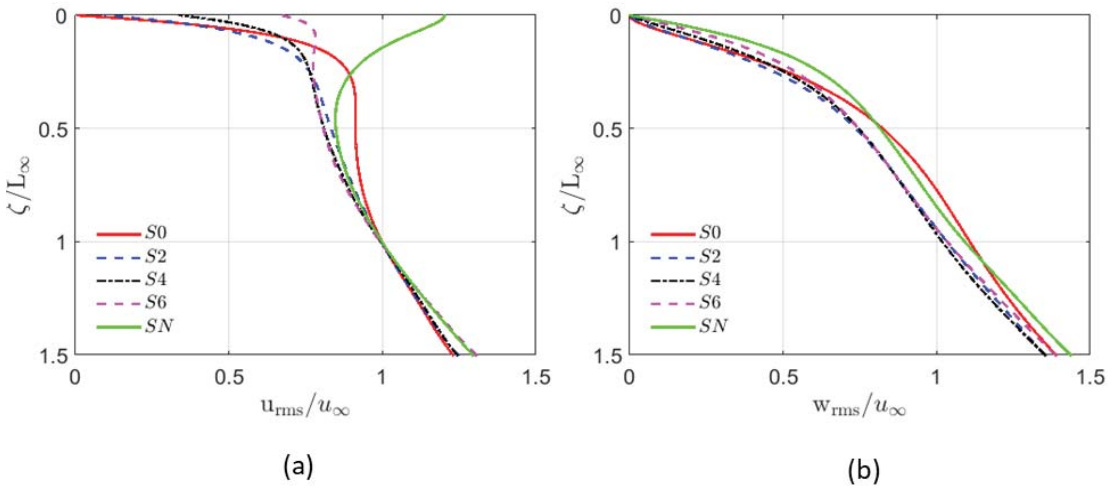

Fig. 6.4. Effect of limited slip-length on the near surface turbulent flow statistics for $S0$, $S2$, $S4$, $S6$, SN based on a combination of horizontal and time averaging from $t = 150 - 300$ (a) u_{rms} (b) w_{rms}.

close to the surface for simulations $S0$, $S2$, $S4$, $S6$ and SN. In this region the

isotropic turbulence, introduced at the bottom, is affected by the presence of the rigid lid and loses its isotropy. The rms values were obtained by averaging in the homogeneous horizontal directions as well as in time (from $t = 150$ to $t = 300$, during which the results were found to have become quasi-steady). Generally, with increasing slip-length the velocity fluctuations at the surface also tend to increase. Because of the rigid lid assumption, the vertical velocity fluctuations all reduce to zero when approaching the surface. As can be seen in Figure 6.5, the gradient $dw_{rms}/d\zeta$ becomes zero at the surface only for the no-slip case $S0$, while for the other cases it gradually increases with increasing slip-length until it reaches a maximum for the free-slip case SN (see also below). Figure 6.6 shows the time-averaged vertical gradient $dw_{rms}/d\zeta$

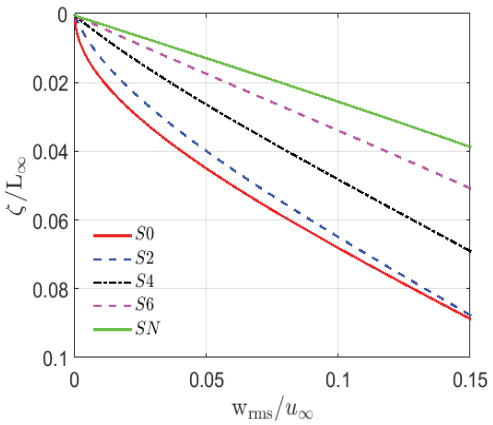

Fig. 6.5. Detail plot of w_{rms} for $S0$, $S2$, $S4$, $S6$, SN based on a combination of horizontal and time averaging from $t = 150 - 300$

at the surface, normalised using u_∞ and L_∞. As already indicated in Figure 6.5, the zero slip-length simulation, $S0$, has indeed zero normal gradient for w_{rms}. For increasing slip-lengths, this gradient is confirmed to gradually increases to a value of 0.0023 for the free-slip case.

The near-surface variation of the horizontal integral length scale, L_{11}, see (5.3) with the ζ-location (distance to the surface) is shown in Figure 6.7 for simulations $S0$, $S2$, $S4$, $S6$, SN. It can be seen that in all simulations the horizontal integral

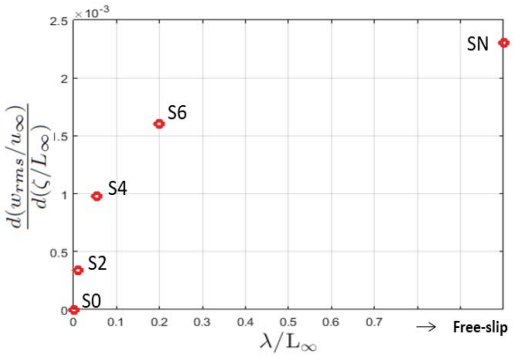

Fig. 6.6. Vertical gradient of w_{rms} at the surface versus slip-length

length scale reaches a clear maximum, while closer to the surface the integral length scale tends to reduce with decreasing slip length. This is probably directly related

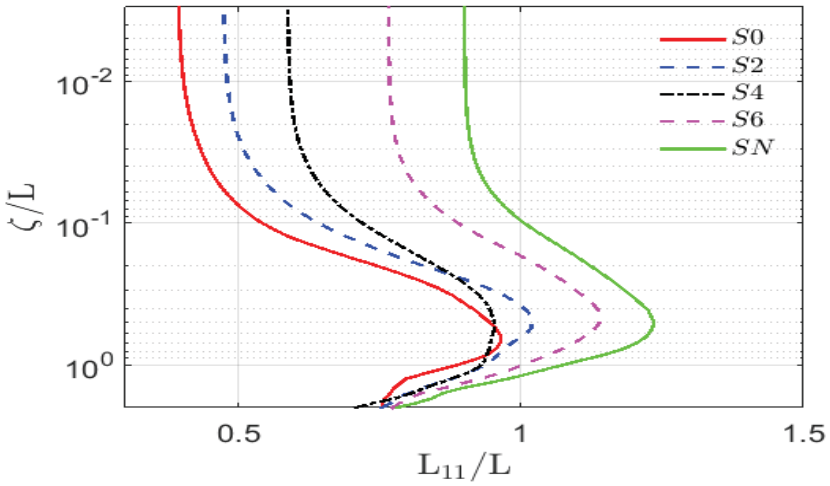

Fig. 6.7. Vertical variation of turbulent integral length scale L_{11} for $S0$, $S2$, $S4$, $S6$, SN (results are time-averaged from $t = 150$ to 300).

to the present of instantaneous shear at the surface in all slip length cases where $\lambda < \infty$. Instantaneous surface shear may reduce the two point correlation, resulting in a reduction of the horizontal integral length scale L_{11}. In the free-slip case, SN,

there is no instantaneous surface shear resulting in a better horizontal correlation and, hence, a larger integral length-scale.

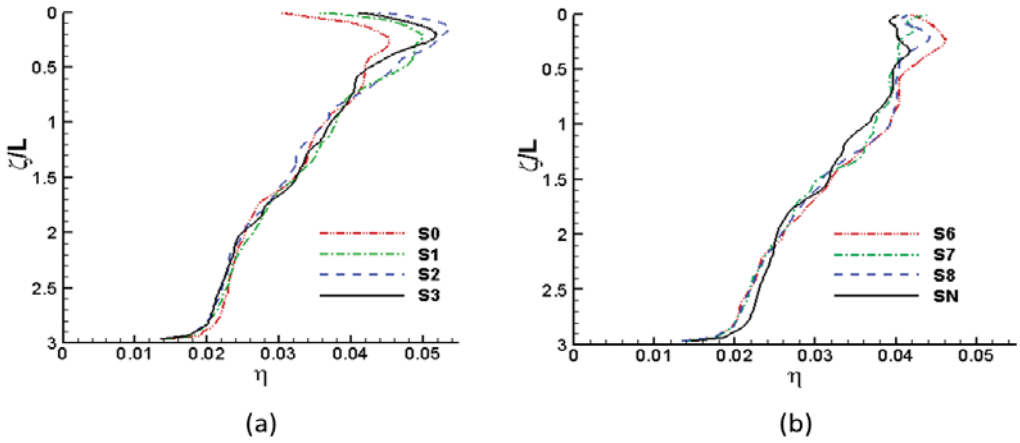

Fig. 6.8. vertical variation of the Kolmogorov length scale η at $t = 300$, simulations (a) $S0$, $S1$, $S2$, $S3$ and (b) $S6$, $S7$, $S8$, SN

The variation of the Kolmogorov length scale (η) with distance to the surface is shown in Figure 6.8 at $t = 300$. It can be seen that close to the surface (η) becomes constant for SN, while it tends to decrease towards the surface for cases with small slip lengths ($S0$, $S1$, $S2$ and $S3$), see Figure 6.8 (a). The latter is likely a consequence of vortex stretching by instantaneous shear forces that experience little to no damping. Please note that the diameter of these vortex tubes typically scales with η, see Jimenez *et al.* [143]. In the cases with large slip lengths, see figure 6.8 (b), such stretching is absent because the near surface horizontal velocity is (nearly) constant close to the surface. Hence, vorticity tubes are not stretched but just convected along the surface by the velocity. as a result η does not reduce significantly when approaching the surface.

Using snapshots with isosurfaces of $\lambda_2 = -0.09$ (corresponding to the second eigenvalue of the sum of the squares of the symmetric and anti-symmetric part of the velocity gradient tensor, see Jeong & Hussain [142]) vortical structures present in the free-slip (SN) and no-slip ($S0$) cases are visualised in Figures 6.9a and 6.9b, respec-

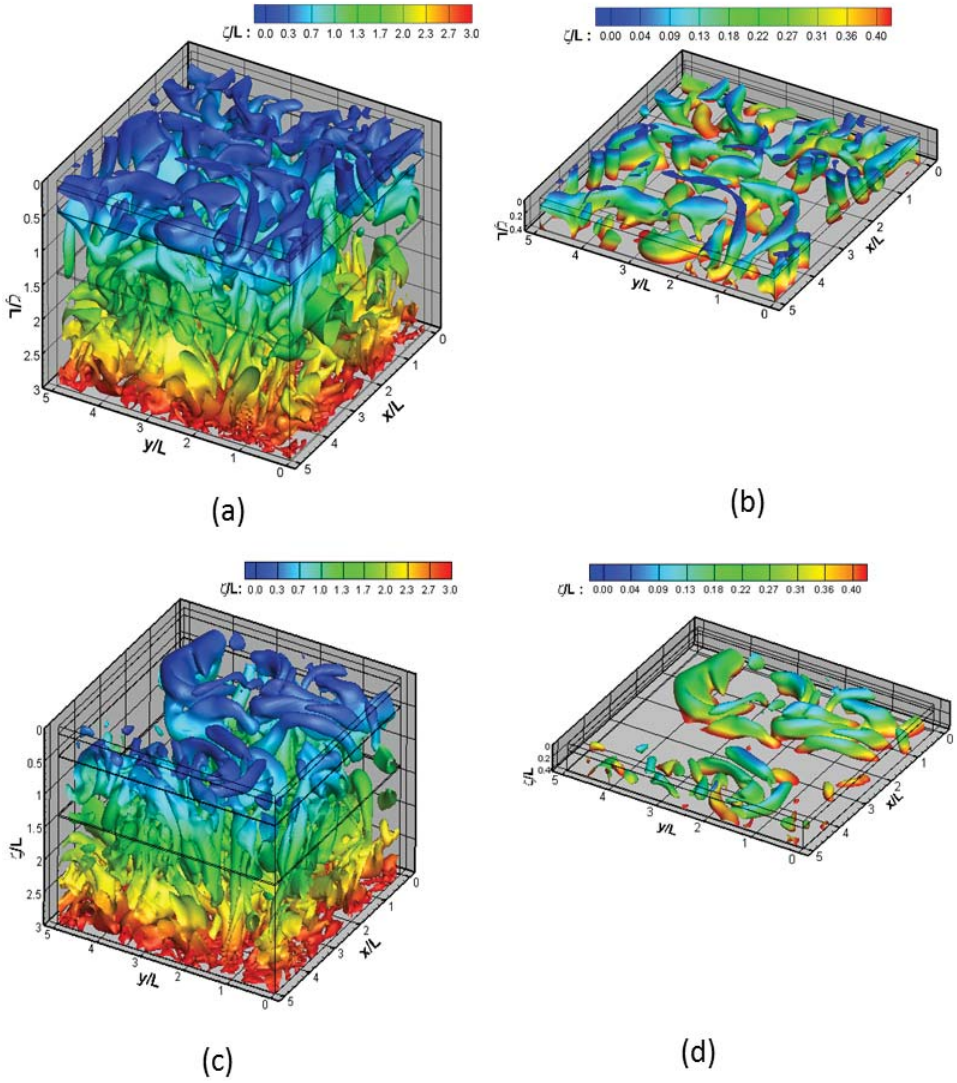

Fig. 6.9. Vortical structures identified using the λ_2 iso-surface at $\lambda_2 = -0.09$ (a) SN, (b) top surface for SN and (c) $S0$, (d) top surface for $S0$, see [142]

tively. The effect of the limiting free-slip case SN on the Kolmogorov length-scale, measured by the width of the vortex tubes, is illustrated clearly. In this simulation, the vortex tubes tend to be either orthogonal or parallel to the surface and those that are parallel do not show much reduction in diameter when approaching the surface. In the no-slip case, there is much more damping close to the surface, but it is very

difficult to identify the vortex stretching due to instantaneous shear. This would require a more detailed study.

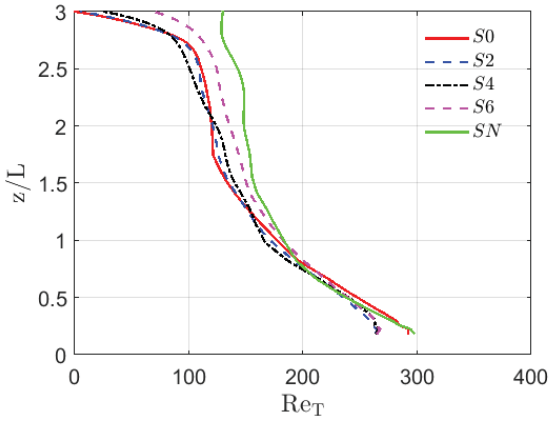

Fig. 6.10. Effect of limited slip-Length on the $Re_T(z)$. Results are obtained by averaging over the interval $t = 150 - 300$.

Figure 6.10 shows the turbulent Reynolds number profiles for various limited slip-length cases obtained after time-averaging the results from $t = 150$ to $300\, L/U$. Please note that here

$$Re_T(z) = \frac{2u_{rms}(z)L_{11}(z)}{\nu}, \tag{6.5}$$

using $u_{rms}(z)$ and $L_{11}(z)$ to replace U_∞ and L_∞ in order to obtain a turbulent Reynolds number that is a function of z. While the horizontal velocity fluctuations u_{rms} reduce when approaching the surface, the integral length scale L_{11} generally increases with the exception of the upper bulk (corresponding to surface-influenced layer). In Figure 6.10, Re_T was found to be approximately constant between $z = 2.0L$ and $z = 2.5L$. This constant Re_T is typical for decaying isotropic turbulence, where the decrease in u_{rms} towards the surface is balanced by the increase in L_{11}, see [92]. The region at the bottom of the computational domain where Re_T is not constant is probably related to the LES-generated isotropic turbulence needing space and time to complete the turbulent spectrum by the generation of small scales that were unresolved in the LES (subgrid-scales). Close to the surface, with the exception of the

free-slip simulation SN, Re_T is generally found to decrease with reducing distance to the surface. In fact, it can be seen that at the surface Re_T reduces with decreasing slip length, (see Figure 6.10).

To illustrate the effects of Re_T, horizontal and vertical velocity fluctuations were compared for the free-slip and no-slip surface boundary conditions, in Figures 6.11 and 6.12, respectively, contrasting the present results to results obtained at various other turbulent Reynolds numbers, as presented in [11] and [10]. To facilitate the

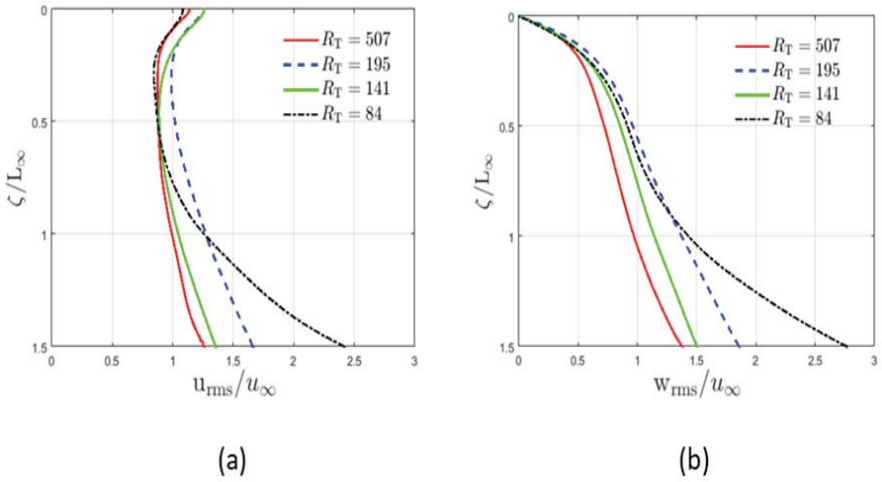

Fig. 6.11. The effect of various turbulent Reynolds numbers on the velocity fluctuations in the presence of the free-slip surface boundary condition. (DNS results from Herlina & Wissink 2014) and Wissink *et. al.* [149] (a) u_{rms} (b) w_{rms}

analysis, we focussed on the middle to upper bulk area. The root-mean-square (rms) of the horizontal and vertical velocity fluctuations for the free-slip case are shown in Figures 6.11a and 6.11b, respectively. It can be seen that the presence of the surface causes the velocity fluctuations to lose their isotropy in the upper bulk region even though at the bottom of the domain isotropic turbulence was introduced. When approaching the surface, the vertical fluctuations are strongly damped, and reduced to zero at the surface, while at the same time kinetic energy is transferred from the vertical to the horizontal fluctuations (which is a result of the conservation of kinetic

energy). The latter explains the increase in the horizontal fluctuations close to the surface.

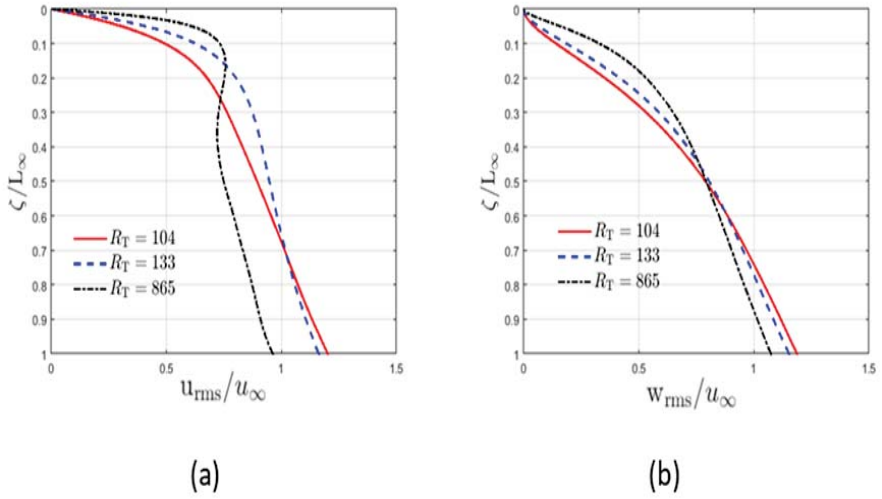

Fig. 6.12. The effect of various turbulent Reynolds numbers on the velocity fluctuations in the presence of a no-slip surface boundary condition. (DNS results from Herlina Wissink 2016) (*a*) u_{rms} (*b*) w_{rms}

The effect of no-slip surface boundary conditions for various Re_T is shown in Figure 6.12. It can be seen that both the horizontal and vertical fluctuations reduce to zero when approaching the surface. Compared to the free-slip simulations, where $\partial w_{rms}/\partial\zeta \neq 0$ (in general), for the no-slip simulations $\partial w_{rms}/\partial\zeta = 0$. Because of this, towards the surface the vertical fluctuations are damped much stronger than the horizontal ones. As a result, as in the free-slip simulations, kinetic energy is transferred from the vertical fluctuations to the horizontal fluctuations. In Figure 6.12a this is clearly evidenced by the local maximum in the horizontal fluctuations at $Re_T = 865$. For the two lower Re_T, the kinetic energy transfer from vertical to horizontal fluctuations is much smaller and hardly (if at all) visible.

The near surface horizontal velocity fluctuations, generated by the initially isotropic turbulence diffusing from below, was found to be significantly influenced by the slip-length. This is illustrated in Figure 6.13, which shows snapshots of the horizontal

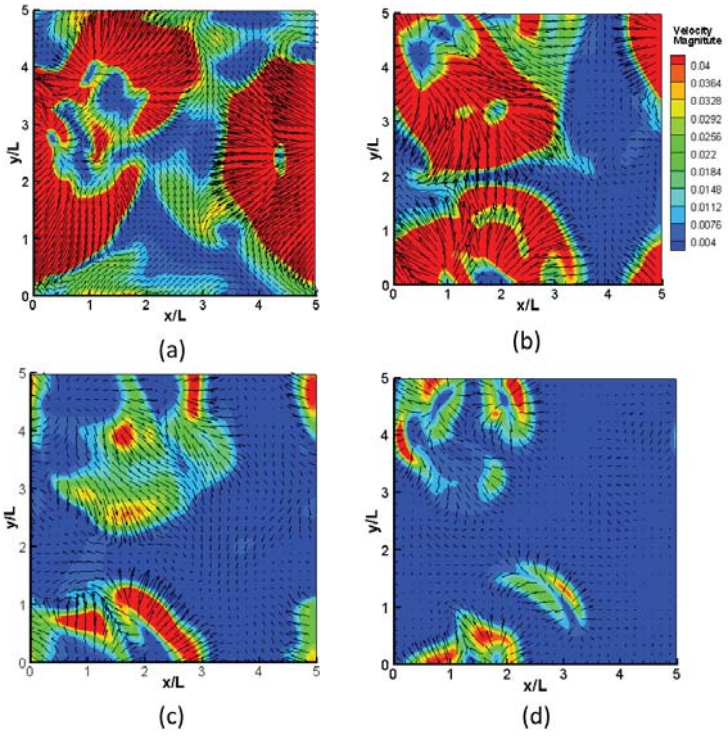

Fig. 6.13. Velocity vectors and magnitude (contours) at the surface of SN, $S7$, $S5$ and $S2$, respectively. Snapshots were taken at $t = 290.0L/U$(see also Table 6.1).

velocity field combined with colour contours of the velocity magnitude. It can be seen that in the largest slip-length case (SN) significant horizontal velocity fluctuations are generated at the surface which gradually reduce for ($S7$), ($S5$) and ($S2$) with decreasing slip-length. Also, the vector field in (SN) indicates the presence of relatively strong up- and down-welling motions. For smaller slip-lengths, e.g. in ($S7$), ($S5$) and ($S2$), these vertical motions become increasingly weaker because of the increased damping of the horizontal velocities at the surface. These vertical up- and down-welling motions are vital for the promotion of interfacial gas exchange between the air and the water. The gas transfer is govern by diffusion at the water surface. However, deeper down, vertical velocity fluctuation tend to exchange gas-saturated water from the surface with unsaturated water from the bulk. Therefore, reducing the thickness of the concentration boundary layer which, in turn, promotes the gas

diffusion at the water surface. As a result, the damping of these vertical fluctuations will cause reduction in the air-water atmospheric gas transfer.

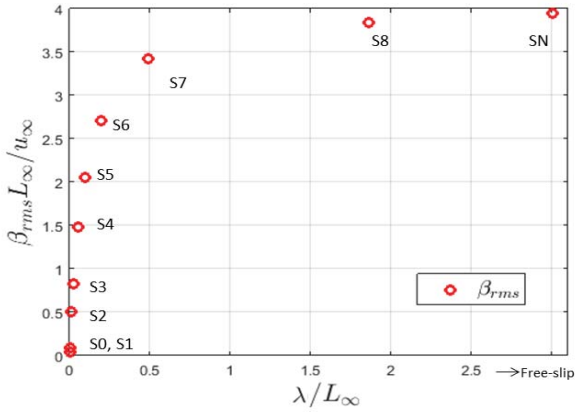

Fig. 6.14. Time-averaged surface divergence $\beta_{rms}L_\infty/u_\infty$ as a function of slip-length.

The root-mean-square of the surface divergence, β_{rms}, was normalised by multiplying it with L_∞/u_∞. The result was subsequently averaged from $t = 150L/U$ to $t = 300L/U$. β_{rms} was calculated for all cases $S0 - SN$ and the results are shown in Figure 6.14. It can be seen that the case with infinite slip-length (the free-slip case) has the largest surface divergence. The surface divergence subsequently smoothly reduces with decreasing slip-length from $S8$ to $S7, \cdots$, to $S1$ and $S0$. The observed smooth reduction in β with decreasing slip-length resembles the smooth reduction in β observed with increasing surfactant pollution level measured by Ma/Ca_T (see Chapter 5). As can be seen below, this observed similarity correctly indicates that it is possible to model the reduction in gas transfer due to Marangoni effects by using limited slip-length as a surface boundary condition.

Figure 6.15 shows the effect of surface slip-length on the surface divergence β. Three slip-length cases are compared, SN, $S7$ and $S2$. The red areas corresponds to positive surface divergence and indicates the upwelling of unsaturated fluid from the bulk. Negative surface divergence is indicated by blue areas and corresponds to the

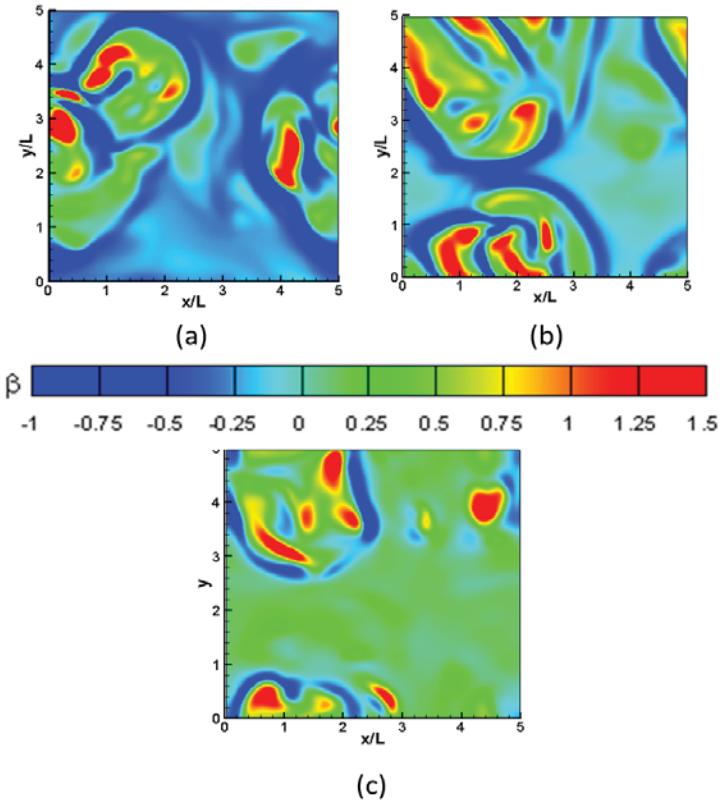

Fig. 6.15. Instantaneous surface divergence (β) contours for SN, $S7$ and $S4$ respectively, snapshots taken at $t = 290.0L/U$

down-welling of saturated fluid from the surface towards the bulk. Large values of β indicate strong up and down-welling motions. It can be seen that for case SN a relatively large variation in β is obtained. This variation in β subsequently reduces with decreasing slip-length.

6.3.2 The effect of slip-length (λ) on the interfacial gas transfer

As shown in Chapter 2, the gas transfer velocity is defined by

$$K_L = \frac{c_s}{c_s - c_b}\bar{j}, \tag{6.6}$$

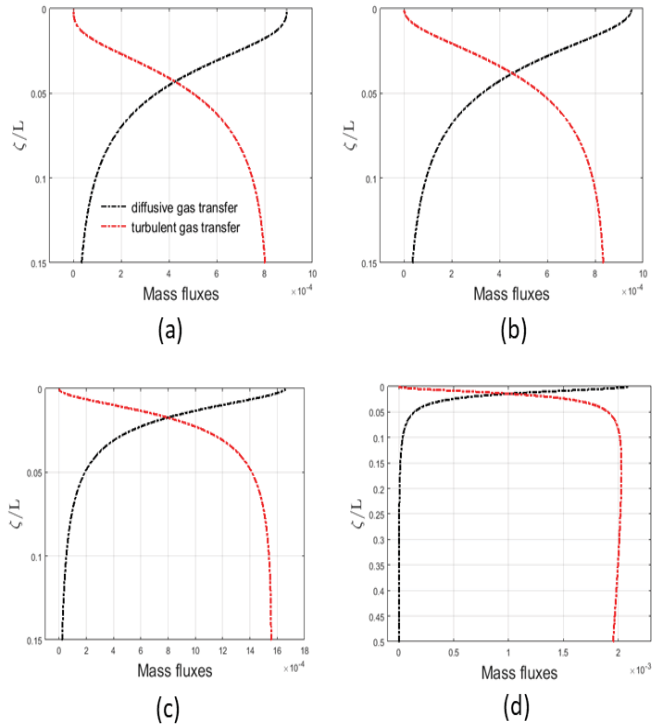

Fig. 6.16. Variation of mass fluxes with depth ζ/L. The total mass flux $-(D\partial\overline{c}/\partial z + \overline{c'w'})$ in time is averged from $t = 150$ to $t = 300$ (a) case $S0$, (b) case $S2$, (c) case $S6$, (d) case SN

where j is the total mass flux component in the z-direction, defined by

$$\bar{j} = \overline{c'w'} - \frac{1}{ScRe}\left.\frac{\partial\overline{c}}{\partial z}\right|_i, \tag{6.7}$$

where $-\frac{1}{ScRe}\left.\frac{\partial\overline{c}}{\partial z}\right|_i$ is the diffusive mass flux and $\overline{c'w'}$ is the turbulent mass flux. It can be seen that very close to the water surface, the mass flux is fully dominated by diffusion. Further down, turbulent convection begins to take over to eventually fully dominate the gas transfer towards the deeper bulk. With increasing slip length, the location of the intersection of the diffusive and turbulent (or convective) contribution to the mass fluxes moves closer to the surface ($\zeta/L = 0.0431, 0.0382, 0.0174, 0.0141$ for $S0, S2, S6$ and SN, respectively) indicating that the diffusive concentration boundary layer thickness decreases in size. This is explained by the damping of turbulence when decreasing the slip length as also seen in Figure 6.4.

Using $\langle c \rangle$ to denote the horizontally averaged concentration, we can differentiate four cases;

1. $c - \langle c \rangle > 0$ and $w > 0$: downward flux of high gas concentration fluid,
2. $c - \langle c \rangle < 0$ and $w < 0$: upward flux of low gas concentration fluid,
3. $c - \langle c \rangle > 0$ and $w < 0$: upward flux of high gas concentration fluid,
4. $c - \langle c \rangle < 0$ and $w > 0$: downward flux of low gas concentration fluid.

If high gas concentration fluid moves downwards (case 1) and is being replaced by low gas concentration fluid moving upwards (case 2) we obtain a positive contribution to the vertical mixing process. If, however, a relatively high gas concentration fluid moves up (case 3) and/or a low gas concentration moves down (case 4), the vertical mixing is reduced.

Figure 6.17 shows the effect of slip length on the normalised instantaneous interfacial gas transfer velocity k_l for two Schmidt numbers $Sc = 8, 32$. For clarity of illustration, two cases ($S2$ and $S7$) with significantly different slip-lengths were selected. It can be seen that with increasing slip length from 0.01 (for $S2$) to 0.50 (for $S7$), k_l significantly increases. This is not only the case for the two selected cases $S2$ and $S7$ which are the closest to the no-slip and free-slip conditions, respectively, but was also found to be a general trend. As well as this, the effect of increasing the Schmidt number Sc is shown in Figure 6.17. In both cases, an increase in Sc from $Sc = 8$ to $Sc = 32$ was found to result in both a reduction in the normalised gas transfer velocity k_l and finer structures appearing in the k_l contours.

Figure 6.18a shows gas transfer velocities obtained for three Schmidt numbers $Sc = 4$, 8 and 32, against L_∞/λ. Figure 6.18b shows gas transfer velocities, obtained for four Schmidt numbers, $Sc = 4$,8, 16 and 32, against Ma/Ca_T. The solid lines interpolating the data points were produced by assuming exponential relationships defined below by Eq. (6.8). It can be seen that in both the surfactant simulations and the slip length simulations, the K_L results can be interpolated very accurately

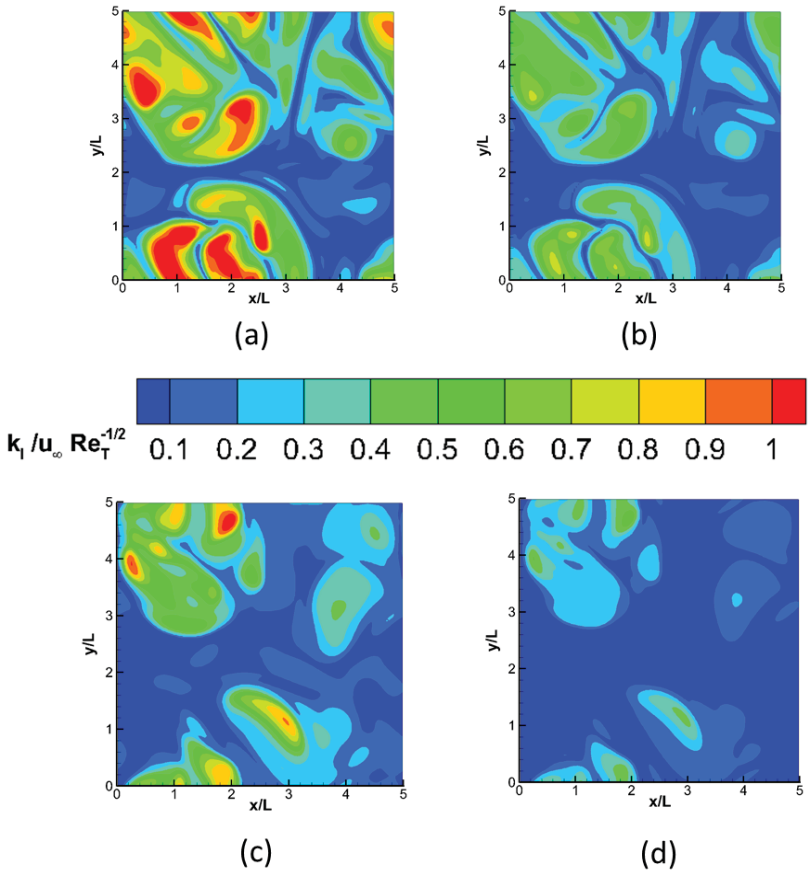

Fig. 6.17. Instantaneous interfacial gas transfer velocity $k_l/u_\infty {Re_T}^{-1/2}$ for (a) $S7$ with $Sc = 8$, (b) $S7$ with $Sc = 32$, (c) $S2$ with $Sc = 8$ and (d) $S2$ with $Sc = 32$. Snapshots were taken at $t = 290.0L/U$.

using similar exponential functions. Note that the data points in Figure 6.18b were obtained using the model of Wissink *et al.* [149] (see also Chapter 5).

Figure 6.19 shows colour contours of the instantaneous gas concentration in the horizontal plane where the concentration fluctuation is maximum. (Note that this location is sometimes used to identify the thickness of the concentration boundary layer.) In all three cases, $S1$, $S6$, and SN, the gas concentration was obtained using a Schmidt number of $Sc = 8$, which provides results that are qualitatively typical of the result obtained at other Sc. The high gas concentration areas (in red) identify

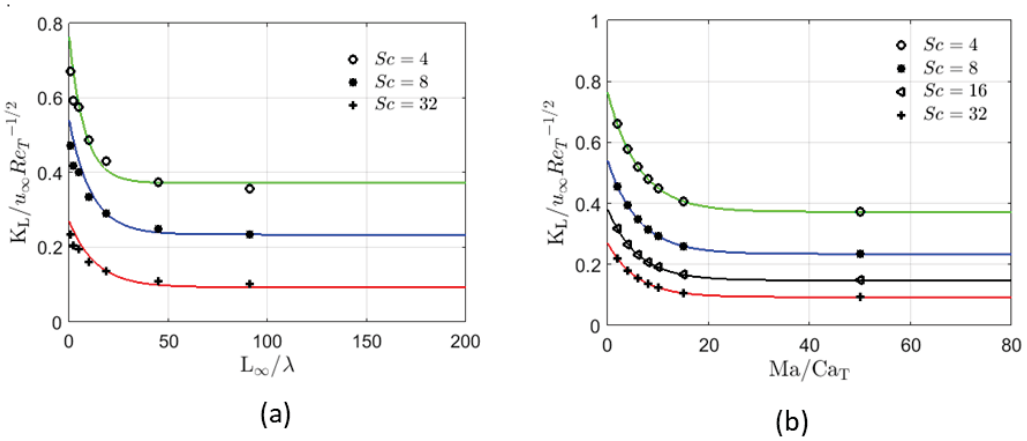

Fig. 6.18. The comparison of K_L for (a) L_∞/λ, (b) Ma/Ca_T

high concentration fluid that was transported downward from the surface, while the low concentration areas (in blue) identify fluid that originates from the bulk. In SN large areas with low gas concentration can be seen. This is a result of the increased turbulence level transporting low concentration fluid from the bulk upwards. For smaller slip lengths, for $S6$ and especially for $S1$, the amount of low concentration fluid reduces because of the decreasing near surface turbulence level with decreasing slip-length.

In Figure 6.4b it was shown that w_{rms} becomes larger with increasing slip length. Hence, it is expected that also the maximum concentration fluctuation c_{rms} obtained at $\zeta = \delta$ would show a similar behaviour and becomes larger with increasing slip length. As can be seen in Figure 6.20, however, this is only true for the smallest slip-lengths (for example for $S0$ - $S3$, as shown in Figure 6.20a). For large slip lengths it was found that the maximum c_{rms} behaves differently and reduces with slip length (for $S6$ - SN, as shown in Figure 6.20b). A possible explanation of this is that increasing w_{rms} causes an increased vertical mixing of the dissolved gases. Such an increased mixing eventually results in smaller variations in concentration (well-mixed region) and hence in a reduced c_{rms}, In other words, what we observed is that if the gas concentration is not yet well mixed, increasing w_{rms} will increase c_{rms}. If w_{rms}

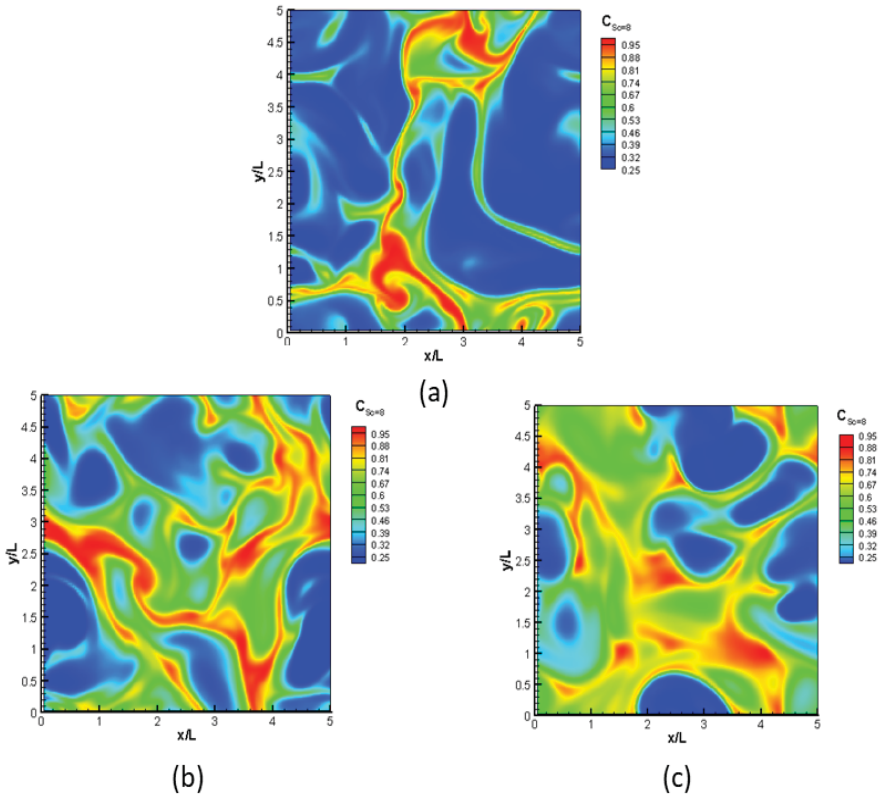

Fig. 6.19. Horizontal cross section through the computational domain at the location where where c_{rms} is maximum. (a) SN, (b) $S6$, (c) $S1$ respectively, snapshots were taken at $t = 300.0L/U$

becomes even larger, the concentration becomes so well-mixed that c_{rms} begins to reduce with slip-length.

6.3.3 Modeling of surfactant pollution effects on gas transfer using slip-length

The normalised gas transfer velocity $K_L^\star$ is obtained by dividing K_L by $u_\infty Re_T^{-1/2}$ (see Eq. 5.10). Using the numerical results obtained in the present simulations and in the surfactant simulations [149], presented in Chapter 5, normalised gas transfer

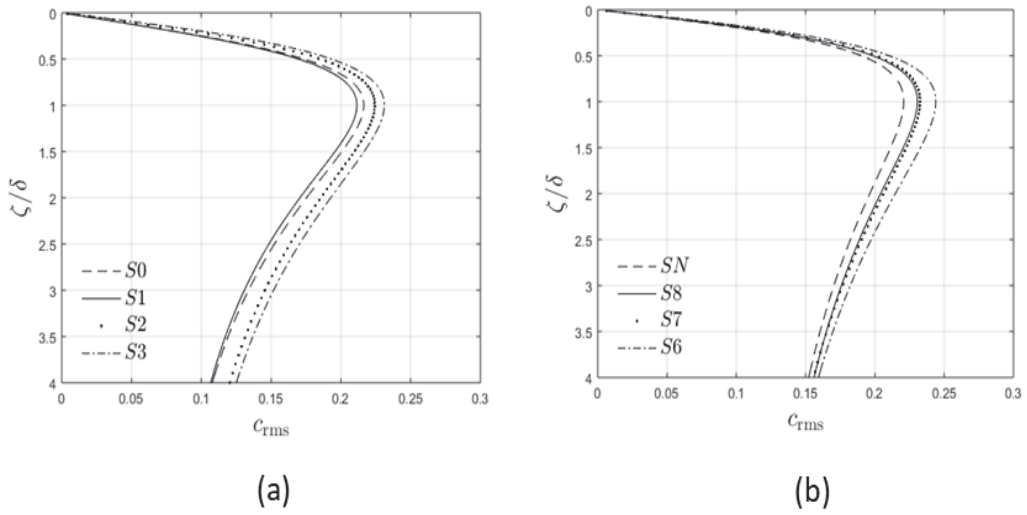

Fig. 6.20. The evaluation of rms of gas concentrations along with the normalised depth by delta δ for various Slip-Length cases (a) $S0$, $S1$, $S2$, $S3$ (b) SN, $S8$, $S70$, $S6$

velocities $K_L^\star(L_\infty/\lambda)$ and $K_L^\star(Ma/Ca_T)$ are obtained. To find the connection between λ and Ma/Ca_T, the following expressions are used as an ansatz

$$\begin{cases} K_L^\star(\frac{L_\infty}{\lambda}) = (K_L^\star(\infty) - K_L^\star(0))\ e^{s\left(\frac{L_\infty}{\lambda}\right)} + K_L^\star(0) \\ K_L^\star\left(\frac{Ma}{Ca_T}\right) = (K_L^\star(\infty) - K_L^\star(0))\ e^{r\left(\frac{Ma}{Ca_T}\right)} + K_L^\star(0) \end{cases}, \tag{6.8}$$

where s and r need to be fitted using the least squares method is, while $K_L^\star(\infty)$ and $K_L^\star(0)$ are the normalised transfer velocities for free-slip (clean) and no-slip (very dirty) boundary conditions at the interface. Note that for $s, r < 0$ this ansatz provides a smooth transition between the free-slip boundary condition (corresponding to $\lambda = \infty$ and $Ma/Ca_T = 0$) and the no-slip boundary condition (corresponding to $\lambda = 0$ and $Ma/Ca_T = \infty$).

Figure 6.21 shows that for both slip-length and surfactant, the powers s and r in Eq. (6.8) depend on the Schmidt number Sc. To approximate these powers as a function of Sc, we assume that they can be represented by power laws

$$\begin{cases} s_{(Sc)} = a_1\, Sc^{b_1}, \\ r_{(Sc)} = a_2\, Sc^{b_2}. \end{cases} \tag{6.9}$$

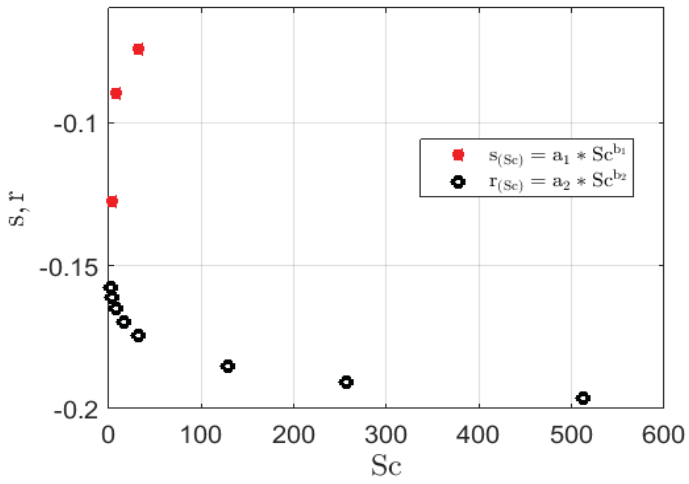

Fig. 6.21. The effect of Schmidt number on the powers s and r in Eq. (6.8)

Because of the limited range of Schmidt numbers employed (especially in the slip-length simulations), the range of Sc over which the approximations are valid is rather limited. It can be seen in Figure 6.21 that the behaviour of s and r is very different. While r tends to increase with decreasing Sc, s tends to decrease. The surfactant simulations show that for large Sc the power r tends to become almost constant. Using the least squares method to approximate the powers in Eq. (6.9), for the slip-length simulation results the best fit was found to be $a_1 = -0.1658$ and $b_1 = -0.2416$, while for the surfactant simulation the best fit was $a_2 = -0.1523$ and $b_2 = 0.0403$.

By equating $K_L^\star(\frac{L_\infty}{b})$ and $K_L^\star\left(\frac{Ma}{Ca_T}\right)$ from (6.9), we obtain the simple expression

$$e^{s\left(\frac{L_\infty}{\lambda}\right)} = e^{r\left(\frac{Ma}{Ca_T}\right)} \Rightarrow s\left(\frac{L_\infty}{\lambda}\right) = r\left(\frac{Ma}{Ca_T}\right) \tag{6.10}$$

so that explicitly writing s and r as functions of the Schmidt number as

$$\frac{\lambda}{L_\infty} = \frac{s(Sc)}{r(Sc)\frac{Ma}{Ca_T}}. \tag{6.11}$$

After substituting (6.9) into (6.11) we finally obtain

$$\frac{\lambda}{L_\infty} = \frac{1.089Sc^{-0.2819}}{\frac{Ma}{Ca_T}}. \tag{6.12}$$

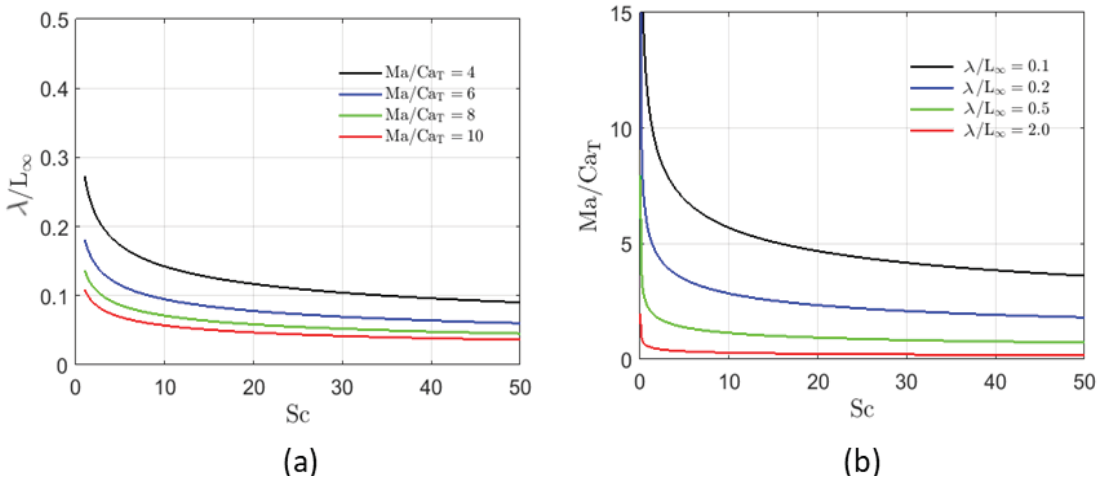

Fig. 6.22. The effect of Sc numbers on the relation between λ/L_∞ and Ma/Ca_T see Eq. (6.12)

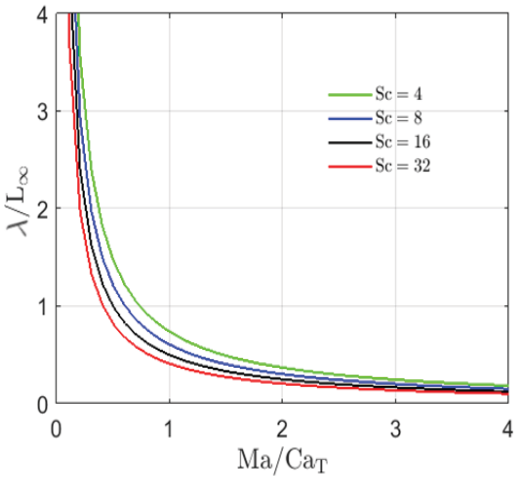

Fig. 6.23. Relation between Ma/Ca_T and λ/L_∞ for various Sc numbers.

It can be seen that the model that was obtained for the slip-length as a function of $\frac{Ma}{Ca_T}$ indeed depends on the Sc number. However, the model is valid for a large range of slip-lengths λ as indicted in Table 6.1. Because the concentration boundary layer becomes extremely thin for very high Sc numbers. There is a indication that in this regime any Sc effects would become negligible. To evaluate the validity of the results for larger Sc, however, is beyond the scope of this chapter.

Figure 6.22 shows the effect of varying Sc with (a) varying λ/L_∞ and fixed Ma/Ca_T and (b) varying Ma/Ca_T and fixed λ/L_∞. The curves shown are solutions of (6.12) and indicate that for large Sc the relation between λ/L_∞ and Ma/Ca_T may become independent on the Schmidt number. For small Sc, however, the relation between λ/L_∞ and Ma/Ca_T begins to heavily depend on Sc. Figure 6.23 shows the relation between Ma/Ca_T and λ/L_∞ obtained when keeping Sc fixed at $Sc = 4, 8, 16, 32$. It can be seen that increases in pollution level correspond to decreases in slip-length. On the other hand, Ma/Ca_T approaches zero, when λ goes to ∞, corresponding to the free-slip condition as explained in Section 6.3.3. Also the distance between subsequent curves tends to become increasingly small, again indicating that for the large Sc the relation between λ/L_∞ and Ma/Ca_T will be virtually Sc independent.

6.4 Conclusion

The aim of the research presented in this chapter was to investigate whether surface contamination by immiscible (with water) surfactants can be modelled by a limited slip boundary condition. It was found that a similar exponential relationship between the surfactant contamination (measured by Ma/Ca_T) and the slip length simulations (as a function of L_∞/λ) exists. Unfortunately, the parameters needed to obtain a good approximation were found to depend on the Schmidt number. However, it appears that for larger Schmidt numbers this dependency on Sc becomes much less important. The latter might be related to the concentration boundary layer becoming exceedingly thin with increasing Sc. Further investigations at higher Sc are needed to confirm this reduced dependency of the parameters on Sc.

Chapter 7: Conclusions and recommendations for future work.

7.1 Conclusions

To study and model the influence of surface contamination on interfacial gas transfer, various Direct Numerical Simulations (DNS) with different levels of contamination were performed. For simplicity, the water surface is assumed to remain perfectly flat (rigid lid assumption) at all times. The gas transfer at the water surface is promoted by isotropic turbulence that is introduced at the bottom of the computational domain. The isotropic turbulence is generated in a large-eddy simulation (LES) that runs concurrently with the DNS. In all gas transfer simulations, up to 5 scalar equations were solved simultaneously. The latter allowed an unbiased comparison of instantaneous results obtained at various Schmidt numbers. In the scalar equations for the dissolved gases, the classical WENO scheme of Liu *et al.* [2] was used to discretise the convection. Diffusive terms in both the scalar equations and the Navier-Stokes equations were discretised using fourth-order central schemes. Time integration was done using a three-stage Runge-Kutta method for the scalars and the second-order-accurate Adams-Bashforth method for the flow solver.

The pollution considered in this work consists of immiscible surfactants like oleyl alcohol. In the surfactant simulations, at the surface, the convection-diffusion equa-

tion for the surfactant was solved using the WENO-Z scheme of Borges *et al.* [3] for convection. Using one-dimensional and two-dimensional test cases the classical WENO scheme was compared to the WENO-Z scheme. It was found that the WENO-Z scheme was able to reach the correct (fifth) order convergence already using relatively coarse meshes, while the original WENO scheme needed much finer meshes to exhibit the theoretical (fifth) order convergence. Also on coarse meshed the results obtained using the WENO-Z scheme significantly more accurate than the the results obtained on the same mesh with the classical WENO scheme. Furthermore, the influence of the parameter ϵ in the weights of the WENO schemes was investigated. For large values of ϵ, both WENO schemes converted to the upwind central scheme. In the end it was decided to employ the WENO-Z scheme for the discretisation of the surfactant as it was more accurate than the classical WENO scheme on uniform, coarse meshes. The actual Schmidt number of the surfactant was confirmed not to influence the surfactant distribution at the surface for $Sc \geq 0.5$. Based on the results obtained in the DNS of interfacial gas transfer affected by the presence of surfactants, a model for the mean (normalised) gas transfer velocity

$$\frac{K_L}{u_\infty \, Re_T^{-1/2}} = c \, Sc^{-q} \tag{7.1}$$

was proposed, where the constant of proportionality is given by

$$c = 1.55 \, \overline{\alpha} + 0.94 \, (1 - \overline{\alpha}), \tag{7.2}$$

and the power coefficient is given by

$$q = 2/3 - 0.258 \, \overline{\alpha}/c. \tag{7.3}$$

This model was found to produce a reasonably good prediction of the gas transfer velocity (with a maximum error of about 10%) for a range of Schmidt numbers and a range of pollution levels. While for low levels of contamination, the instantaneous clean surface fraction was well defined with steep gradients between the clean and dirty areas, with increasing levels of contamination these gradients become less and

less steep. Hence, it became much more difficult to differentiate between dirty and clean areas. To still obtain a good quantitative approximation of the mean gas transfer velocity it was needed to introduce a threshold vale to determine which areas of a surface where deemed to be clean and which were dirty.

In principle, the model above, that predicts the mean gas transfer velocity based on $\overline{\alpha}$, can be used to determine K_L by remotely determining the clean surface fraction of water combined with measurements of the turbulence length and velocity scales.

Furthermore, it was found that the well-known surface divergence model completely breaks down in the presence of surfactant pollution. Even relatively small levels of pollution have a significant effect on the gas transfer velocity due to the the Marangoni forces' damping of near surface turbulence. This damping involves a reduction of the surface divergence to zero for larger levels of pollution, making the surface divergence model unusable.

To model the effect of surfactant pollution on the mean gas transfer velocity using finite slip lengths, further DNS were performed. In these DNS a limited slip length λ was introduced at the surface to determine its effect on the gas transfer velocity. In these simulations, clean conditions correspond to an infinite slip-length which was represented by a free-slip surface boundary condition. To model very dirty conditions a zero slip-length was used. With decreasing slip length, a smooth transition was found for the mean gas transfer velocity between the value typical for clean conditions and the value typical for very dirty conditions. Using a similar smooth transition (with increased level od pollution) obtained in the surfactant simulation a model was derived that relates Ma/Ca_T to λ as

$$\frac{\lambda}{L_\infty} = \frac{1.089\, Sc^{-0.2819}}{Ma/Ca_T}, \tag{7.4}$$

where L_∞ is the integral length. It can be seen that this relation is not Schmidt number independent. As it was derived only for rather small Schmidt numbers (up to $Sc = 32$). The Schmidt number dependency was found to be quite strong, especially for the lower Schmidt numbers. For larger Schmidt numbers, however, it appeared that the Schmidt number dependency became much less pronounced.

7.2 Recommendations for future work

Various surfactants may have non-zero solubility in water. It is interesting to perform further simulations in order to study how these surfactants affect gas transfer and how their concentration at the surface reduces in time.

Also, the limited slip-length simulations only gave a prediction for the effect of λ on the mean gas transfer velocity K_L for relatively small Schmidt numbers. Further simulations, preformed at larger Sc are needed to improve or confirm the relation between λ and Ma/Ca_T (see in Section 7.1).

It would be recommendable to replace the classical WENO scheme for the scalar convection calculations in the DNS by the WENO-Z scheme when calculating on a uniform mesh. If needed a mixture of classical (for non-uniform directions) and WENO-Z (for uniform directions) schemes could be used.

LIST OF REFERENCES

LIST OF REFERENCES

[1] L. Shen, D. K. Yue, and G. S. Triantafyllou, "Effect of surfactants on free-surface turbulent flows," *Journal of Fluid Mechanics*, vol. 506, pp. 79–115, 2004.

[2] X.-D. Liu, S. Osher, and T. Chan, "Weighted essentially non-oscillatory schemes," *Journal of Computational Physics*, vol. 115, no. 1, pp. 200–212, 1994.

[3] R. Borges, M. Carmona, B. Costa, and W. S. Don, "An improved weighted essentially non-oscillatory scheme for hyperbolic conservation laws," *Journal of Computational Physics*, vol. 227, no. 6, pp. 3191–3211, 2008.

[4] M. A. Donelan and R. Wanninkhof, "Gas transfer at water surfaces—concepts and issues," *Gas Transfer at Water Surfaces*, pp. 1–10, 2002.

[5] "Ipcc, 2001: climate change 2001: the scientific basis. contribution of working group 1 to the third assessment report of the intergovernmental panel on climate change, author=Smithson, Peter A, journal=International Journal of Climatology, volume=22, number=9, pages=1144–1144, year=2002, publisher=Wiley Online Library,"

[6] J. Raven, K. Caldeira, H. Elderfield, O. Hoegh-Guldberg, P. Liss, U. Riebesell, J. Shepherd, C. Turley, and A. Watson, *Ocean acidification due to increasing atmospheric carbon dioxide*. The Royal Society, 2005.

[7] H. Riebeek, "The carbon cycle: Feature articles," 2011.

[8] E. B. Kraus and J. A. Businger, *Atmosphere-ocean interaction*, vol. 27. Oxford University Press, 1994.

[9] L. Lombard, "Oceanic oxygen changes as a bellwether of climate change," p. 3, 2007.

[10] H. Herlina and J. Wissink, "Isotropic-turbulence-induced mass transfer across a severely contaminated water surface," *Journal of Fluid Mechanics*, vol. 797, pp. 665–682, 2016.

[11] H. Herlina and J. G. Wissink, "Direct numerical simulation of turbulent scalar transport across a flat surface," *Journal of Fluid Mechanics*, vol. 744, pp. 217–249, 2014.

[12] W. K. Lewis and W. G. Whitman, "Principles of gas apsorption," *Industrial and Engineering Chemnisty*, vol. 16, 1924.

[13] M. J. McCready, E. Vassiliadou, and T. J. Hanratty, "Computer simulation of turbulent mass transfer at a mobile interface," *AIChE Journal*, vol. 32, pp. 1108–1115, 1986.

[14] R. Higbie, "The rate of absorption of a pure gas into still liquid during short periods of exposure," *Gas Transfer at Water Surfaces*, 1935.

[15] P. V. Dancwerts, "ifisance of liqui nts in gas absor," *Gas Transfer at Water Surfaces*, vol. 43, pp. 1460–1467, 1951.

[16] G. Fortescue and J. R. A. Pearson, "On gas absorption into a turbulent liquid," *Chemical Engineering Science*, vol. 22, 1967.

[17] S. Banerjee, D. Scott, and E. Rhodes, "Mass transfer to falling wavy liquid films in turbulent flow," *Industrial & Engineering Chemistry Fundamentals*, vol. 7, no. 1, pp. 22–27, 1968.

[18] J. C. Lamont and D. S. Scott, "An eddy cell model of mass transfer into the surface of a turbulent liquid," *AIChE Journal*, vol. 16, 1970.

[19] T. G. Theofanous, R. N. Houze, and L. K. Brumfield, "Turbulent mass transfer at free, gas-liquid interfaces, with applications to open-channel, bubble and jet flows," *International Journal of Heat and Mass Transfer*, vol. 19, 1976.

[20] Herlina2005, "Gas transfer at the air-water interface in a turbulent flow environment," *Universitaetsverlag Karlsruhe*, ISBN 3-937300-74-0.

[21] G. Matthess, "wind/wave-tunnel experiment on the schmidt number-and wave field dependence of air/water gas exchange," vol. 65, pp. 303–309, 1984.

[22] Jähne and Haußecker, "Air water gas exchange," *Annual Review of Fluid Mechanics*, vol. 30, pp. 443–468, 1998.

[23] P. Liss, "Processes of gas exchange across an air-water interface," in *Deep Sea Research and Oceanographic Abstracts*, vol. 20, pp. 221–238, Elsevier, 1973.

[24] Engineeringtoolbox.com, "Density of dry air, water vapor and moist humid air," 2015.

[25] H. Jirka, Gerhard, H. Herlina, and A. Niepelt, "Gas transfer at the air-water interface: Experiments with different turbulence forcing mechanisms," *Experiments in Fluids*, vol. 49, pp. 319–327, 2010.

[26] D. J. O'Connor and W. E. Dobbins, "The mechanics of reaeration in natural streams," *Journal of the Sanitary Engineering Division*, vol. 82, no. 6, pp. 1–30, 1958.

[27] M. Churchill *et al.*, "Effect of water temperature on stream reaeration," *J Sanitary Eng*, vol. 504, no. 5, p. 87, 1961.

[28] E. L. Thackston and P. A. Krenkel, "Reaeration prediction in natural streams," *Journal of the Sanitary Engineering Division*, vol. 95, no. 1, pp. 65–94, 1969.

[29] E. Plate and R. Friedrich, "Reaeration of open channel flow," in *Gas Transfer at Water Surfaces*, pp. 333–346, Springer, 1984.

[30] J. S. Gulliver and M. J. Halverson, "Air-water gas transfer in open channels," *Water Resources Research*, vol. 25, no. 8, pp. 1783–1793, 1989.

[31] D. B. Moog and G. H. Jirka, "Air-water gas transfer in uniform flows with large gravel-bed roughness," *Gas Transfer at Water Surfaces*, pp. 371–375, 2002.

[32] D. E. Turney, W. C. Smith, and S. Banerjee, "A measure of near-surface fluid motions that predicts air-water gas transfer in a wide range of conditions," *Geophysical Research Letters*, vol. 32, no. 4, 2005.

[33] B. H. Brumley and G. H. Jirka, "Air water transfer of slightly soluble gases-turbulence, interfacial processes and conceptual models," *Physicochemical Hydrodynamics*, vol. 10.3, pp. 295–319, 1988.

[34] B. Jähne, K. O. Münnich, R. Bösinger, A. Dutzi, W. Huber, and P. Libner, "On the parameters influencing air-water gas exchange," *Journal of Geophysical Research: Oceans*, vol. 92, no. C2, pp. 1937–1949, 1987.

[35] B. Jähne, W. Huber, A. Dutzi, T. Wais, and J. Ilmberger, "Wind/wave-tunnel experiment on the schmidt number—and wave field dependence of air/water gas exchange," in *Gas Transfer at Water Surfaces*, pp. 303–309, Springer, 1984.

[36] R. Upstill-Goddard, A. Watson, P. Liss, and M. Liddicoat, "Gas transfer velocities in lakes measured with sf6," *Tellus B*, vol. 42, no. 4, pp. 364–377, 1990.

[37] A. Jessup, W. Asher, M. Atmane, K. Phadnis, C. J. Zappa, and M. Loewen, "Evidence for complete and partial surface renewal at an air-water interface," *Geophysical Research Letters*, vol. 36, no. 16, 2009.

[38] P. Harriott, "A random eddy modification of the penetration theory," *Chemical Engineering Science*, vol. 17, pp. 149–154, 1962.

[39] Q. Liao and B. Wang, "Near surface turbulence and gas exchange across the air-sea interface," vol. 1, p. 3, 2013.

[40] T. Theofanous, "Conceptual models of gas exchange," in *Gas Transfer at Water Surfaces*, pp. 271–281, Springer, 1984.

[41] C. R. Chu and G. H. Jirka, "Turbulent gas flux measurements below the air-water interface of a grid-stirred tank," *International Journal of Heat and Mass Transfer*, vol. 35, no. 8, pp. 1957–1968, 1992.

[42] W. E. Asher and J. F. Pankow, "The interaction of mechanically generated turbulence and interfacial films with a liquid phase controlled gaslliquid transport process," *Tellus B: Chemical and Physical Meteorology*, vol. 38, no. 5, pp. 305–318, 1986.

[43] H. Tennekes and J. L. Lumley, *A first course in turbulence*. MIT press, 1972.

[44] S. B. Pope, "Turbulent flows," 2001.

[45] C. Pozrikidis, *Fluid dynamics: theory, computation, and numerical simulation*. Springer, 2016.

[46] S. P. McKenna and W. R. McGillis, "Surface divergence and air-water gas transfer," *Gas transfer at Water Surfaces*, pp. 129–134, 2002.

[47] S. McKenna and W. McGillis, "The role of free-surface turbulence and surfactants in air–water gas transfer," *International Journal of Heat and Mass Transfer*, vol. 47, no. 3, pp. 539–553, 2004.

[48] Y. Hasegawa and N. Kasagi, "Turbulent mass transfer mechanism across a contaminated air-water interface," in *TSFP DIGITAL LIBRARY ONLINE*, Begel House Inc., 2005.

[49] S. Banerjee and S. MacIntyre, "The air-water interface: Turbulence and scalar exchange," in *PIV and Water Waves*, pp. 181–237, World Scientific, 2004.

[50] J. W. Deardorff, G. E. Willis, and D. K. Lilly, "Laboratory investigation of non-steady penetrative convection," *Journal of Fluid Mechanics*, vol. 35, no. 1, pp. 7–31, 1969.

[51] K. B. Katsaros, W. T. Liu, J. A. Businger, and J. E. Tillman, "Heat thermal structure in the interfacial boundary layer measured in an open tank of water in turbulent free convection," *Journal of Fluid Mechanics*, vol. 83, no. 2, pp. 311–335, 1977.

[52] T. J. Shay and M. C. Gregg, "Turbulence in an oceanic convective mixed layer," *Nature*, vol. 310, no. 5975, p. 282, 1984.

[53] T. J. Shay and M. Gregg, "Convectively driven turbulent mixing in the upper ocean," *Journal of Physical Oceanography*, vol. 16, no. 11, pp. 1777–1798, 1986.

[54] N. Graham and T. Barnett, "Sea surface temperature, surface wind divergence, and convection over tropical oceans," *Science*, vol. 238, no. 4827, pp. 657–659, 1987.

[55] J. Imberger, "The diurnal mixed layer," *Limnology and Oceanography*, vol. 30, no. 4, pp. 737–770, 1985.

[56] J. M. Brubaker, "Similarity structure in the convective boundary layer of a lake," *Nature*, vol. 330, no. 6150, p. 742, 1987.

[57] J. Sander, A. Simon, T. Jonas, and A. Wüest, "Surface turbulence in natural waters: A comparison of large eddy simulations with microstructure observations," *Journal of Geophysical Research: Oceans*, vol. 105, no. C1, pp. 1195–1207, 2000.

[58] T. Jonas, A. Stips, W. Eugster, and A. Wüest, "Observations of a quasi shear-free lacustrine convective boundary layer: Stratification and its implications on turbulence," *Journal of Geophysical Research: Oceans*, vol. 108, no. C10, 2003.

[59] O. Zeman and J. L. Lumley, "Modeling buoyancy driven mixed layers," *Journal of the Atmospheric Sciences*, vol. 33, no. 10, pp. 1974–1988, 1976.

[60] S. MacIntyre, W. Eugster, and G. W. Kling, "The critical importance of buoyancy flux for gas flux across the air-water interface," *Gas Transfer at Water Surfaces*, pp. 135–139, 2001.

[61] W. Eugster, G. Kling, T. Jonas, J. P. McFadden, A. Wüest, S. MacIntyre, and F. S. Chapin, "Co2 exchange between air and water in an arctic alaskan and midlatitude swiss lake: Importance of convective mixing," *Journal of Geophysical Research: Atmospheres*, vol. 108, no. D12, 2003.

[62] M. Lee, "Visualization of oxygen transfer across the air–water interface using a fluorescence oxygen visualization method," *Water Research*, vol. 36, no. 8, pp. 2140–2146, 2002.

[63] S. G. Schladow, M. Lee, B. E. Hürzeler, and P. B. Kelly, "Oxygen transfer across the air-water interface by natural convection in lakes," *Limnology and Oceanography*, vol. 47, no. 5, pp. 1394–1404, 2002.

[64] J. Wissink and H. Herlina, "Direct numerical simulation of gas transfer across the air–water interface driven by buoyant convection," *Journal of Fluid Mechanics*, vol. 787, pp. 508–540, 2016.

[65] F. Ali, J. G. Wissink, and H. Herlina, "Modeling air-water heat transfer induced by buoyant convection," *International Journal of Computational Physics Series*, vol. 1, no. 2, pp. 15–16, 2018.

[66] B. Jahne, K. Münnich, and U. Siegenthaler, "Measurements of gas exchange and momentum transfer in a circular wind-water tunnel," *Tellus*, vol. 31, no. 4, pp. 321–329, 1979.

[67] L. Merlivat and L. Memery, "Gas exchange across an air-water interface: Experimental results and modeling of bubble contribution to transfer," *Journal of Geophysical Research: Oceans*, vol. 88, no. C1, pp. 707–724, 1983.

[68] B. Jähne and H. Haußecker, "Air-water gas exchange," *Annual Review of Fluid Mechanics*, vol. 30, no. 1, pp. 443–468, 1998.

[69] N. M. Frew, E. J. Bock, U. Schimpf, T. Hara, H. Haußecker, J. B. Edson, W. R. McGillis, R. K. Nelson, S. P. McKenna, B. M. Uz, *et al.*, "Air-sea gas transfer: Its dependence on wind stress, small-scale roughness, and surface films," *Journal of Geophysical Research: Oceans*, vol. 109, no. C8, 2004.

[70] R. Lee and J. Saylor, "The effect of a surfactant monolayer on oxygen transfer across an air/water interface during mixed convection," *International Journal of Heat and Mass Transfer*, vol. 53, no. 17-18, pp. 3405–3413, 2010.

[71] L. Wolff and T. Hanratty, "Instantaneous concentration profiles of oxygen accompanying absorption in a stratified flow," *Experiments in Fluids*, vol. 16, no. 6, pp. 385–392, 1994.

[72] P. T. Woodrow and S. R. Duke, "Laser-induced fluorescence studies of oxygen transfer across unsheared flat and wavy air- water interfaces," *Industrial & Engineering Chemistry Research*, vol. 40, no. 8, pp. 1985–1995, 2001.

[73] T. Münsterer, H. J. Mayer, and B. Jähne, "Dual-tracer measurements of concentration profiles in the aqueous mass boundary layer," in *Air-Water Gas Transfer: 3rd International Symposium on Air-Water Gas Transfer*, pp. 637–648, 1995.

[74] T. Münsterer, *LIF Investigation of the Mechanisms Controlling Air–Water Mass Transfer at a Free Interface*. PhD thesis, 1996.

[75] T. Münsterer and B. Jähne, "Lif measurements of concentration profiles in the aqueous mass boundary layer," *Experiments in Fluids*, vol. 25, no. 3, pp. 190–196, 1998.

[76] W. L. Peirson, "Measurement of surface velocities and shears at a wavy air–water interface using particle image velocimetry," *Experiments in Fluids*, vol. 23, no. 5, pp. 427–437, 1997.

[77] D. J. O'Connor, "Wind effects on gas-liquid transfer coefficients," *Journal of Environmental Engineering*, vol. 109, no. 3, pp. 731–752, 1983.

[78] S. Kitaigorodskii, "On the fluid dynamical theory of turbulent gas transfer across an air-sea interface in the presence of breaking wind-waves," *Journal of Physical Oceanography*, vol. 14, no. 5, pp. 960–972, 1984.

[79] C. R. Chu and G. H. Jirka, "Wind and stream flow induced reaeration," *Journal of Environmental Engineering*, vol. 129, no. 12, pp. 1129–1136, 2003.

[80] J. Crusius and R. Wanninkhof, "Gas transfer velocities measured at low wind speed over a lake," *Limnology and Oceanography*, vol. 48, no. 3, pp. 1010–1017, 2003.

[81] T. Kunugi, S.-i. Satake, and Y. Ose, "Direct numerical simulation of carbon-dioxide gas absorption caused by turbulent free surface flow," *International Journal of Heat and Fluid Flow*, vol. 22, no. 3, pp. 245–251, 2001.

[82] R. Kurose, N. Takagaki, A. Kimura, and S. Komori, "Direct numerical simulation of turbulent heat transfer across a sheared wind-driven gas–liquid interface," *Journal of Fluid Mechanics*, vol. 804, pp. 646–687, 2016.

[83] D. Lakehal, M. Fulgosi, G. Yadigaroglu, and S. Banerjee, "Direct numerical simulation of turbulent heat transfer across a mobile, sheared gas-liquid interface," *Journal of Heat Transfer*, vol. 125, no. 6, pp. 1129–1139, 2003.

[84] G. H. Jirka and A. H.-W. Ho, "Measurements of gas concentration fluctuations at water surface," *Journal of Hydraulic Engineering*, vol. 116, no. 6, pp. 835–847, 1990.

[85] D. B. Moog and G. H. Jirka, "Analysis of reaeration equations using mean multiplicative error," *Journal of Environmental Engineering*, vol. 124, no. 2, pp. 104–110, 1998.

[86] D. B. Moog and G. H. Jirka, "stream reaeration in non-uniform channel flow," *Journal of Hydraulic Engineering*, vol. 125, no. 1, pp. 11–16, 1999.

[87] M. A. Atmane and J. George, "Gas transfer across a zero-shear surface: A local approach," *Gas Transfer at Water Surfaces*, pp. 255–259, 2002.

[88] B. Brumley, "Air-water transfer of slightly soluble gases: Turbulence, interfacial processes and conceptual models," *Physicochemical Hydrodynamics*, vol. 10, no. 3, pp. 295–319, 1988.

[89] A. Tamburrino and J. S. Gulliver, "Free-surface turbulence and mass transfer in a channel flow," *AIChE Journal*, vol. 48, no. 12, pp. 2732–2743, 2002.

[90] Y. Lau, "experimental investigation of reaeration in open-channel flow," *Progress in Water Technology*, 1975.

[91] K. Suga and M. Kubo, "Modelling turbulent high schmidt number mass transfer across undeformable gas–liquid interfaces," *International Journal of Heat and Mass Transfer*, vol. 53, no. 15-16, pp. 2989–2995, 2010.

[92] B. H. Brumley and G. H. Jirka, "Near-surface turbulence in a grid-stirred tank," *Journal of Fluid Mechanics*, vol. 183, pp. 235–263, 1987.

[93] J. Hunt and J. Graham, "Free-stream turbulence near plane boundaries," *Journal of Fluid Mechanics*, vol. 84, no. 2, pp. 209–235, 1978.

[94] J. Hunt, "Turbulence structure and turbulent diffusion near gas-liquid interfaces," in *Gas Transfer at Water Surfaces*, pp. 67–82, Springer, 1984.

[95] R. H. Sabersky and A. J. A. E. G. Hauptenn, "Fluid flow; a first course in fluid mechanics, macmillan publishing company," *New York*, 1989.

[96] G. Lapham, D. Dowling, and W. Schultz, "In situ force-balance tensiometry," *Experiments in Fluids*, vol. 27, no. 2, pp. 157–166, 1999.

[97] R. Khakpour, Hamid, L. Shen, and D. K. P. Yue, "Transport of passive scalar in turbulent shear flow under a clean or surfactant-contaminated free surface,"

[98] H. C. Broecker, "The influence of wind on co_2-exchange in a wind-wave tunnel, including the effect of monolayers," *J. mar. Res.*, vol. 36, pp. 595–610, 1978.

[99] S. E. K. Rideal and D. M. Robb, *Interfacial phenomena*. 1963.

[100] J. Saylor, G. Smith, and K. Flack, "The effect of a surfactant monolayer on the temperature field of a water surface undergoing evaporation," *International Journal of Heat and Mass Transfer*, vol. 43, no. 17, pp. 3073–3086, 2000.

[101] W.-t. Tsai and K.-K. Liu, "An assessment of the effect of sea surface surfactant on global atmosphere-ocean co2 flux," *Journal of Geophysical Research: Oceans*, vol. 108, no. C4, 2003.

[102] W.-T. Tsai and D. K. Yue, "Effects of soluble and insoluble surfactant on laminar interactions of vortical flows with a free surface," *Journal of Fluid Mechanics*, vol. 289, pp. 315–349, 1995.

[103] J. C. Goldman, M. R. Dennett, and N. M. Frew, "Surfactant effects on air-sea gas exchange under turbulent conditions," *Deep Sea Research Part A. Oceanographic Research Papers*, vol. 35, no. 12, pp. 1953–1970, 1988.

[104] E. J. Bock, T. Hara, N. M. Frew, and W. R. McGillis, "Relationship between air-sea gas transfer and short wind waves," *Journal of Geophysical Research: Oceans*, vol. 104, no. C11, pp. 25821–25831, 1999.

[105] J. Lucassen, "Longitudinal capillary waves. part 1.—theory," *Transactions of the Faraday Society*, vol. 64, pp. 2221–2229, 1968.

[106] W.-T. Tsai, "Impact of a surfactant on a turbulent shear layer under the air-sea interface," *Journal of Geophysical Research: Oceans*, vol. 101, no. C12, pp. 28557–28568, 1996.

[107] Q. Zhang, R. A. Handler, and S. T. Fredriksson, "Direct numerical simulation of turbulent free convection in the presence of a surfactant," *International Journal of Heat and Mass Transfer*, vol. 61, pp. 82–93, 2013.

[108] R. Handler, R. Leighton, G. Smith, and R. Nagaosa, "Surfactant effects on passive scalar transport in a fully developed turbulent flow," *International Journal of Heat and Mass Transfer*, vol. 46, no. 12, pp. 2219–2238, 2003.

[109] L. Bernal, A. Hirsa, J. Kwon, and W. Willmarth, "On the interaction of vortex rings and pairs with a free surface for varying amounts of surface active agent," *Physics of Fluids A: Fluid Dynamics*, vol. 1, no. 12, pp. 2001–2004, 1989.

[110] D. G. Anthony, A. Hirsa, and W. W. Willmarth, "On the interaction of a submerged turbulent jet with a clean or contaminated free surface," *Physics of Fluids A: Fluid Dynamics*, vol. 3, no. 2, pp. 245–247, 1991.

[111] C. E. Willert and M. Gharib, "The interaction of spatially modulated vortex pairs with free surfaces," *Journal of Fluid Mechanics*, vol. 345, pp. 227–250, 1997.

[112] K. Flack, J. Saylor, and G. Smith, "Near-surface turbulence for evaporative convection at an air/water interface," *Physics of Fluids*, vol. 13, no. 11, pp. 3338–3345, 2001.

[113] W. R. Smith and J. G. Wissink, "Parameterization of travelling waves in plane poiseuille flow," *The IMA Journal of Applied Mathematics*, vol. 79, no. 1, pp. 22–32, 2012.

[114] J. Wissink, "On unconditional conservation of kinetic energy by finite-difference discretizations of the linear and non-linear convection equation," *Computers & Fluids*, vol. 33, no. 2, pp. 315–343, 2004.

[115] F. H. Harlow and J. E. Welch, "Numerical calculation of time-dependent viscous incompressible flow of fluid with free surface," *The Physics of Fluids*, vol. 8, no. 12, pp. 2182–2189, 1965.

[116] P. J. Roache, "Verfication and validation in computational science and engineering," 1998.

[117] Y. Morinishi, T. S. Lund, O. V. Vasilyev, and P. Moin, "Fully conservative higher order finite difference schemes for incompressible flow," *Journal of Computational Physics*, vol. 143, no. 1, pp. 90–124, 1998.

[118] Y. Hasegawa and N. Kasagi, "Hybrid dns/les of high schmidt number mass transfer across turbulent air–water interface," *International Journal of Heat and Mass Transfer*, vol. 52, no. 3, pp. 1012–1022, 2009.

[119] F. Schwertfirm and M. Manhart, "Dns of passive scalar transport in turbulent channel flow at high schmidt numbers," *International Journal of Heat and Fluid Flow*, vol. 28, no. 6, pp. 1204–1214, 2007.

[120] B. Kubrak, H. Herlina, F. Greve, and J. Wissink, "Low-diffusivity scalar transport using a weno scheme and dual meshing," *Journal of Computational Physics*, vol. 240, pp. 158–173, 2013.

[121] G.-S. Jiang and C.-W. Shu, "Efficient implementation of weighted eno schemes," *Journal of Computational Physics*, vol. 126, no. 1, pp. 202–228, 1996.

[122] D. S. Balsara and C.-W. Shu, "Monotonicity preserving weighted essentially non-oscillatory schemes with increasingly high order of accuracy," *Journal of Computational Physics*, vol. 160, no. 2, pp. 405–452, 2000.

[123] A. K. Henrick, T. D. Aslam, and J. M. Powers, "Mapped weighted essentially non-oscillatory schemes: achieving optimal order near critical points," *Journal of Computational Physics*, vol. 207, no. 2, pp. 542–567, 2005.

[124] S. Gottlieb and C.-W. Shu, "Total variation diminishing runge-kutta schemes," *Mathematics of computation of the American Mathematical Society*, vol. 67, no. 221, pp. 73–85, 1998.

[125] B. Geurts, *Elements of direct and large-eddy simulation*. RT Edwards Philadelphia, 2004.

[126] P. Sagaut, "Turbulence direct numerical simulation and large-eddy simulation," *Encyclopedia of Computational Mechanics*, 2004.

[127] C. Wagner, T. Hüttl, and P. Sagaut, *Large-eddy simulation for acoustics*, vol. 20. Cambridge University Press, 2007.

[128] D. C. Wilcox, "Turbulence modeling for cfd, dcw industries, 1998," *Google Scholar*, 1994.

[129] P. Sagaut, *Large eddy simulation for incompressible flows: an introduction*. Springer Science & Business Media, 2006.

[130] J. Smagorinsky, "General circulation experiments with the primitive equations: I. the basic experiment," *Monthly Weather Review*, vol. 91, no. 3, pp. 99–164, 1963.

[131] J. M.Peric, *Computational Methods for Fluid Dynamics*. Springer, 2002.

[132] B. A. Johnson and E. A. Cowen, "Turbulent boundary layers absent mean shear," *Journal of Fluid Mechanics*, vol. 835, p. 217–251, 2018.

[133] H. Herlina and J. Wissink, "Simulation of air–water interfacial mass transfer driven by high-intensity isotropic turbulence," *Journal of Fluid Mechanics*, vol. 860, pp. 419–440, 2019.

[134] G. Grötzbach, "Spatial resolution requirements for direct numerical simulation of the rayleigh-bénard convection," *Journal of Computational Physics*, vol. 49, no. 2, pp. 241–264, 1983.

[135] Y. Hasegawa and N. Kasagi, "Systematic analysis of high schmidt number turbulent mass transfer across clean, contaminated and solid interfaces," *International Journal of Heat and Fluid Flow*, vol. 29, no. 3, pp. 765–773, 2008.

[136] W.-t. Tsai, "Vortex dynamics beneath a surfactant-contaminated ocean surface," *Journal of Geophysical Research: Oceans*, vol. 103, no. C12, pp. 27919–27930, 1998.

[137] G. H. JIRKA *et al.*, "Experiments on gas transfer at the air–water interface induced by oscillating grid turbulence," *Journal of Fluid Mechanics*, vol. 594, pp. 183–208, 2008.

[138] E. Hopfinger and J.-A. Toly, "Spatially decaying turbulence and its relation to mixing across density interfaces," *Journal of Fluid Mechanics*, vol. 78, no. 1, pp. 155–175, 1976.

[139] M. Coantic, "A model of gas transfer across air-water interfaces with capillary waves," *Journal of Geophysical Research: Oceans*, vol. 91, no. C3, pp. 3925–3943, 1986.

[140] J. J. Ledwell, "The variation of the gas transfer coefficient with molecular diffusity," in *Gas Transfer at Water Surfaces*, pp. 293–302, Springer, 1984.

[141] B. Perot and P. Moin, "Shear-free turbulent boundary layers. part 1. physical insights into near-wall turbulence," *Journal of Fluid Mechanics*, vol. 295, pp. 199–227, 1995.

[142] J. Jeong and F. Hussain, "On the identification of a vortex," *Journal of Fluid Mechanics*, vol. 285, pp. 69–94, 1995.

[143] J. Jiménez, A. A. Wray, P. G. Saffman, and R. S. Rogallo, "The structure of intense vorticity in isotropic turbulence," *Journal of Fluid Mechanics*, vol. 255, pp. 65–90, 1993.

[144] D. Turney, "Coherent motions and time scales that control heat and mass transfer at wind-swept water surfaces," *Journal of Geophysical Research: Oceans*, vol. 121, no. 12, pp. 8731–8748, 2016.

[145] J. Magnaudet and I. Calmet, "Turbulent mass transfer through a flat shear-free surface," *Journal of Fluid Mechanics*, vol. 553, pp. 155–185, 2006.

[146] A. Kermani, H. R. Khakpour, L. Shen, and T. Igusa, "Statistics of surface renewal of passive scalars in free-surface turbulence," *Journal of Fluid Mechanics*, vol. 678, pp. 379–416, 2011.

[147] C. Law and B. Khoo, "Transport across a turbulent air-water interface," *AIChE Journal*, vol. 48, no. 9, pp. 1856–1868, 2002.

[148] J. Davies, "Turbulence phenomena at free surfaces," *AIChE Journal*, vol. 18, no. 1, pp. 169–173, 1972.

[149] J. Wissink, H. Herlina, Y. Akar, and M. Uhlmann, "Effect of surface contamination on interfacial mass transfer rate," *Journal of Fluid Mechanics*, vol. 830, pp. 5–34, 2017.

[150] J. R. Philip, "Flows satisfying mixed no-slip and no-shear conditions," *Zeitschrift für angewandte Mathematik und Physik ZAMP*, vol. 23, no. 3, pp. 353–372, 1972.

[151] J. R. Philip, "Integral properties of flows satisfying mixed no-slip and no-shear conditions," *Zeitschrift für angewandte Mathematik und Physik ZAMP*, vol. 23, no. 6, pp. 960–968, 1972.

[152] E. Lauga and H. A. Stone, "Effective slip in pressure-driven stokes flow," *Journal of Fluid Mechanics*, vol. 489, pp. 55–77, 2003.

[153] C. Ybert, C. Barentin, C. Cottin-Bizonne, P. Joseph, and L. Bocquet, "Achieving large slip with superhydrophobic surfaces: Scaling laws for generic geometries," *Physics of Fluids*, vol. 19, no. 12, p. 123601, 2007.

[154] A. M. Davis and E. Lauga, "Hydrodynamic friction of fakir-like superhydrophobic surfaces," *Journal of Fluid Mechanics*, vol. 661, pp. 402–411, 2010.

[155] C.-H. Choi and C.-J. Kim, "Large slip of aqueous liquid flow over a nanoengineered superhydrophobic surface," *Physical Review Letters*, vol. 96, no. 6, p. 066001, 2006.

[156] L. Bocquet, P. Tabeling, and S. Manneville, "Comment on" large slip of aqueous liquid flow over a nanoengineered superhydrophobic surface"," *Physical Review Letters*, vol. 97, no. 10, p. 109601, 2006.

[157] N. V. Priezjev, "Rate-dependent slip boundary conditions for simple fluids," *Physical Review E*, vol. 75, no. 5, p. 051605, 2007.

Appendix A

```
================================================
 KCFlo Definition file
================================================

 JOB_NAME=LES_Bottom
 JOB_CLASS=SURF

 JOB_NR=U0

 SOURCE_VERSION=SURF
 SOURCE_USER_PART=usr9_3NEW

------------------------------------------------
 DESCRIPTION='Bottom turbulence, Re=600'
------------------------------------------------

 KC_BottomTurbulence=.TRUE.
 KC_BottomDecay=.TRUE.
 KC_BufferSc=0.5
 KC_SurfaceSlip=.TRUE.
 KC_SolveScalar=.TRUE.
 KC_Surfactant=.FALSE.
 KC_Ma/Ca=0.0
 KC_Refine=2
 KC_RefineSurf=1
 KC_IsoboxLES=.TRUE.
 KC_GridDelta=4.8
 KC_SmagorinskyConstant=0.22
 KC_DiffTimeScalar=7.0
 KC_ReynoldsNumber=600.0
 KC_ThermalExpansion=0.0 # nonzero for buoyant calculation
 KC_TurbulenceLevel=0.40 # only effective for isotropic box
 KC_timestep=0.0001
 KC_NumTimeSteps=3000005
  KC_NumTimeSteps=10
 KC_ScalarCoarse=2
 KC_Schmidt1=2  # This is the Prandtl number if thermal expansion is nonzero
 KC_Schmidt2=4
 KC_Schmidt3=8
 KC_Schmidt4=16
 KC_Schmidt5=32

 Schmidt number for surfactants

 KC_SchmidtSf1=2
```

```
================================================
RESTART / RUN OPTIONS
(default: RESTART=.FALSE./reinitmean=.FALSE./NRUNS=1000)
------------------------------------------------

KC_SYNC=.TRUE.
KC_RESTART=.FALSE.                  # use old resultfile for restart
KC_walltime=14400; #[seconds] limit=24h
KC_StartAveragingTime=40; #non dimensional time-units
KC_DelTimeOut=0.25
JOBCLASS=production; USE_LOADLEVELER=yes; Runtime=1800;#[min] limit=18h
 JOBCLASS=development; USE_LOADLEVELER=yes; Runtime=50;#[min] limit=18h
export NRUNS=80                       # nr of runs in job_chain

================================================
GRID and DOMAIN DECOMPOSITION
------------------------------------------------

gridsize      decomposition  periodic  homogeneous
grid_ni=128;     i_nr=4;      i_cyc=1; i_aver=1
grid_nj=128;     j_nr=4;      j_cyc=1; j_aver=1
grid_nk=212;     k_nr=4;      k_cyc=0; k_aver=0

KC_XLEN=5.0
KC_YLEN=5.0
KC_ZLEN=3.0

================================================
GRID and DOMAIN DECOMPOSITION CONCURRENT CALCULATION
only taken into account if KC_BottomTurbulence=.TRUE.
------------------------------------------------

gridsize      decomposition  periodic  homogeneous
grid_ni2=64;     i_nr2=2;     i_cyc2=1; i_aver2=1
grid_nj2=64;     j_nr2=2;     j_cyc2=1; j_aver2=1
grid_nk2=64;     k_nr2=1;     k_cyc2=1; k_aver2=1

KC_XLEN2=5.0
KC_YLEN2=5.0
KC_ZLEN2=5.0

================================================
DOMAIN DECOMPOSITION SECOND CONCURRENT CALCULATION
only taken into account if KC_Surfactant=.TRUE.
------------------------------------------------

decomposition
  i_nr3=2
  j_nr3=2
================================================
```

Fig. 7.1. Definition file of *S*0 free-slip simulation

```
================================================
 KCFlo Definition file
================================================

 JOB_NAME=LES_Bottom
 JOB_CLASS=SURF

 JOB_NR=U13

 SOURCE_VERSION=SURF
 SOURCE_USER_PART=usr9_3NEW

------------------------------------------------
 DESCRIPTION='Bottom turbulence, Re=600'
------------------------------------------------

 KC_BottomTurbulence=.TRUE.
 KC_BottomDecay=.TRUE.
 KC_BufferSc=0.5
 KC_SurfaceSlip=.TRUE.
 KC_SolveScalar=.TRUE.
 KC_Surfactant=.TRUE.
 KC_Ma/Ca=0.12
 KC_Refine=2
 KC_RefineSurf=1
 KC_IsoboxLES=.TRUE.
 KC_GridDelta=4.8
 KC_SmagorinskyConstant=0.22
 KC_DiffTimeScalar=7.0
 KC_ReynoldsNumber=600.0
 KC_ThermalExpansion=0.0 # nonzero for buoyant calculation
 KC_TurbulenceLevel=0.40 # only effective for isotropic box
 KC_timestep=0.0001
 KC_NumTimeSteps=3000005
  KC_NumTimeSteps=10
 KC_ScalarCoarse=2
 KC_Schmidt1=2  # This is the Prandtl number if thermal expansion is nonzero
 KC_Schmidt2=4
 KC_Schmidt3=8
 KC_Schmidt4=16
 KC_Schmidt5=32

 Schmidt number for surfactants

 KC_SchmidtSf1=2
```

```
================================================
RESTART / RUN OPTIONS
(default: RESTART=.FALSE./reinitmean=.FALSE./NRUNS=1000)
------------------------------------------------

KC_SYNC=.TRUE.
KC_RESTART=.FALSE.                  # use old resultfile for restart
KC_walltime=14400; #[seconds] limit=24h
KC_StartAveragingTime=40; #non dimensional time-units
KC_DelTimeOut=0.25
JOBCLASS=production; USE_LOADLEVELER=yes; Runtime=1800;#[min] limit=18h
 JOBCLASS=development; USE_LOADLEVELER=yes; Runtime=50;#[min] limit=18h
export NRUNS=80                      # nr of runs in job_chain

================================================
GRID and DOMAIN DECOMPOSITION
------------------------------------------------

gridsize      decomposition  periodic  homogeneous
grid_ni=128;     i_nr=4;      i_cyc=1; i_aver=1
grid_nj=128;     j_nr=4;      j_cyc=1; j_aver=1
grid_nk=212;     k_nr=4;      k_cyc=0; k_aver=0

KC_XLEN=5.0
KC_YLEN=5.0
KC_ZLEN=3.0

================================================
GRID and DOMAIN DECOMPOSITION CONCURRENT CALCULATION
only taken into account if KC_BottomTurbulence=.TRUE.
------------------------------------------------

gridsize      decomposition  periodic  homogeneous
grid_ni2=64;     i_nr2=2;     i_cyc2=1; i_aver2=1
grid_nj2=64;     j_nr2=2;     j_cyc2=1; j_aver2=1
grid_nk2=64;     k_nr2=1;     k_cyc2=1; k_aver2=1

KC_XLEN2=5.0
KC_YLEN2=5.0
KC_ZLEN2=5.0

================================================
DOMAIN DECOMPOSITION SECOND CONCURRENT CALCULATION
only taken into account if KC_Surfactant=.TRUE.
------------------------------------------------

decomposition
  i_nr3=2
  j_nr3=2
================================================
```

Fig. 7.2. Typical definition file used in the surfactant simulations. The parameter KC_Ma/Ca (corresponding to Ma/Ca) is varied from $Ma/Ca = 0.12$ for $S1$ to $Ma/Ca = 30$ for $S5$

```
================================================
 KCFlo Definition file
================================================

 JOB_NAME=LES_Bottom
 JOB_CLASS=SURF

 JOB_NR=UN

 SOURCE_VERSION=SURF
 SOURCE_USER_PART=usr9_3NEW

------------------------------------------------
 DESCRIPTION='Bottom turbulence, Re=600'
------------------------------------------------

 KC_BottomTurbulence=.TRUE.
 KC_BottomDecay=.TRUE.
 KC_BufferSc=0.5
 KC_SurfaceSlip=.FALSE.
 KC_SlipLength=0
 KC_SolveScalar=.TRUE.
 KC_Surfactant=.FALSE.
 KC_Ma/Ca=1000.0
 KC_Refine=2
 KC_RefineSurf=1
 KC_IsoboxLES=.TRUE.
 KC_GridDelta=4.8
 KC_SmagorinskyConstant=0.22
 KC_DiffTimeScalar=7.0
 KC_ReynoldsNumber=600.0
 KC_ThermalExpansion=0.0 # nonzero for buoyant calculation
 KC_TurbulenceLevel=0.40 # only effective for isotropic box
 KC_timestep=0.0001
 KC_NumTimeSteps=3000005
  KC_NumTimeSteps=10
 KC_ScalarCoarse=2
 KC_Schmidt1=2  # This is the Prandtl number if thermal expansion is nonzero
 KC_Schmidt2=4
 KC_Schmidt3=8
 KC_Schmidt4=16
 KC_Schmidt5=32

 Schmidt number for surfactants

 KC_SchmidtSf1=2
```

```
================================================
RESTART / RUN OPTIONS
(default: RESTART=.FALSE./reinitmean=.FALSE./NRUNS=1000)
------------------------------------------------

KC_SYNC=.TRUE.
KC_RESTART=.FALSE.                # use old resultfile for restart
KC_walltime=14400; #[seconds] limit=24h
KC_StartAveragingTime=40; #non dimensional time-units
KC_DelTimeOut=0.25
JOBCLASS=production; USE_LOADLEVELER=yes; Runtime=1800;#[min] limit=18h
 JOBCLASS=development; USE_LOADLEVELER=yes; Runtime=50;#[min] limit=18h
export NRUNS=100                      # nr of runs in job_chain

================================================
GRID and DOMAIN DECOMPOSITION
------------------------------------------------

gridsize      decomposition  periodic  homogeneous
grid_ni=128;     i_nr=4;      i_cyc=1; i_aver=1
grid_nj=128;     j_nr=4;      j_cyc=1; j_aver=1
grid_nk=212;     k_nr=4;      k_cyc=0; k_aver=0

KC_XLEN=5.0
KC_YLEN=5.0
KC_ZLEN=3.0

================================================
GRID and DOMAIN DECOMPOSITION CONCURRENT CALCULATION
only taken into account if KC_BottomTurbulence=.TRUE.
------------------------------------------------

gridsize      decomposition  periodic  homogeneous
grid_ni2=64;     i_nr2=2;     i_cyc2=1; i_aver2=1
grid_nj2=64;     j_nr2=2;     j_cyc2=1; j_aver2=1
grid_nk2=64;     k_nr2=1;     k_cyc2=1; k_aver2=1

KC_XLEN2=5.0
KC_YLEN2=5.0
KC_ZLEN2=5.0

================================================
DOMAIN DECOMPOSITION SECOND CONCURRENT CALCULATION
only taken into account if KC_Surfactant=.TRUE.
------------------------------------------------

decomposition
  i_nr3=2
  j_nr3=2
================================================
```

Fig. 7.3. Definition file of SN, no-slip simulation

Appendix B

```
================================================
 KCFlo Definition file
================================================

 JOB_NAME=LES_Bottom
 JOB_CLASS=SLIP

 JOB_NR=L0001

 SOURCE_VERSION=SHEAR
 SOURCE_USER_PART=usr9_2NEW

------------------------------------------------
 DESCRIPTION='Bottom turbulence, Re=600'
------------------------------------------------

 KC_BottomTurbulence=.TRUE.
 KC_BottomDecay=.TRUE.
 KC_BufferSc=0.5
 KC_SurfaceSlip=.FALSE.
 KC_SurfaceShear=.FALSE.
  KC_TopShear=1.0
 KC_SlipLength=0.001
 KC_SolveScalar=.TRUE.
 KC_Surfactant=.FALSE.
 KC_MaoverWe=0.0
 KC_Refine=2
 KC_RefineSurf=1
 KC_VelocitySurf=0.0
 KC_IsoboxLES=.TRUE.
 KC_GridDelta=4.8
 KC_SmagorinskyConstant=0.22
 KC_DiffTimeScalar=7.0
 KC_ReynoldsNumber=600.0
 KC_ThermalExpansion=0.0 # nonzero for buoyant calculation
 KC_TurbulenceLevel=0.40 # only effective for isotropic box
 KC_timestep=0.0001
 KC_NumTimeSteps=3000005
  KC_NumTimeSteps=800000  # Done this one
 KC_ScalarCoarse=2
 KC_Schmidt1=4  # This is the Prandtl number if thermal expansion is nonzero
 KC_Schmidt2=8
 KC_Schmidt3=32
 KC_Schmidt4=0
 KC_Schmidt5=0

 Schmidt number for surfactants

 KC_SchmidtSf1=2
```

```
================================================
 RESTART / RUN OPTIONS
 (default: RESTART=.FALSE./reinitmean=.FALSE./NRUNS=1000)
------------------------------------------------

 KC_SYNC=.TRUE.
 KC_RESTART=.FALSE.                # use old resultfile for restart
 KC_walltime=14400; #[seconds] limit=24h
 KC_StartAveragingTime=40; #non dimensional time-units
 KC_DelTimeOut=0.25
 JOBCLASS=production; USE_LOADLEVELER=yes; Runtime=72000;#[sec] limit=18h
  JOBCLASS=development; USE_LOADLEVELER=yes; Runtime=1800;#[sec] limit=18h
 export NRUNS=80                     # nr of runs in job_chain

================================================
 GRID and DOMAIN DECOMPOSITION
------------------------------------------------

 gridsize      decomposition  periodic  homogeneous
 grid_ni=128;     i_nr=4;      i_cyc=1; i_aver=1
 grid_nj=128;     j_nr=4;      j_cyc=1; j_aver=1
 grid_nk=212;     k_nr=4;      k_cyc=0; k_aver=0

 KC_XLEN=5.0
 KC_YLEN=5.0
 KC_ZLEN=3.0

================================================
 GRID and DOMAIN DECOMPOSITION CONCURRENT CALCULATION
 only taken into account if KC_BottomTurbulence=.TRUE.
------------------------------------------------

 gridsize      decomposition  periodic  homogeneous
 grid_ni2=64;     i_nr2=2;     i_cyc2=1; i_aver2=1
 grid_nj2=64;     j_nr2=2;     j_cyc2=1; j_aver2=1
 grid_nk2=64;     k_nr2=1;     k_cyc2=1; k_aver2=1

 KC_XLEN2=5.0
 KC_YLEN2=5.0
 KC_ZLEN2=5.0

================================================
 DOMAIN DECOMPOSITION SECOND CONCURRENT CALCULATION
 only taken into account if KC_Surfactant=.TRUE.
------------------------------------------------

 decomposition
   i_nr3=2
   j_nr3=2
================================================
```

Fig. 7.4. Typical definition file used in the slip length simulations. The parameter KC_SlipLength is varied from $\lambda/L = 0.01$ for $S1$ to $\lambda/L = 2.0$ for $S8$.

Appendix C

```
!  PROGRAM: Surfactant WENO 1D
!************************************************************************************
    program surfactant

    implicit none

    integer::N
    real*8 eps
    parameter(N=270,eps=0.000001D0)
!
    real*8 x(-1:N+2),xc(-1:N+2)           ! xc(i)=0.5*(x(i)+x(i+1))
    real*8 u(-1:N+2)
    real*8 Ph(-1:N+2),Ph0(-1:N+2),Ph1(-1:N+2),Ph2(-1:N+2)
    real*8 L0(0:N),L1(0:N),L2(0:N)
    real*8 IS(0:N+2)
    real*8 a0plus(0:N),a1plus(0:N),a2plus(0:N),a0min(0:N),a1min(0:N),a2min(0:N)
    real*8 Rplus(0:N),Rmin(0:N+1)
    character*1 cc
!
!
    real*8 alpha,dx,dy,ct,dt,pival
    real*8 P
!

    integer:: i,it,nt
!
    open(unit=13,file='Test.4dat')
!
     pival=4.D0*DATAN(1.D0)
     ct=0.D0
     nt=4000
     dt=1.D0/nt
     dx=1.D0/N
     alpha=0.D0 ! diffusion
 !
     u=1
     u(-1)=u(N-1)
     u(0)=u(N)
     u(N+1)=u(1)
     u(N+2)=u(2)
!
!
     do  i=-1,N+2
        x(i)  = (i-0.5D0)*dx
        xc(i) =  i*dx
     end do
!
     do i=-1,N+2
        Ph(i)=0.5D0*(1.D0+SIN(2*pival*x(i)))
     end do

!    write(13,*) Ph(-1),Ph(N-1),Ph(0),Ph(N),Ph(N+1),Ph(1),Ph(N+2),Ph(2)
!
```

```
!     start time iteration
!
   do it=1,nt            ! time loop

     ct=ct+dt

     Ph(-1)=Ph(N-1)
     Ph(0)=Ph(N)
     Ph(N+1)=Ph(1)
     Ph(N+2)=Ph(2)
!     write(13,*) Ph(-1),Ph(N-1),Ph(0),Ph(N),Ph(N+1),Ph(1),Ph(N+2),Ph(2)
     Ph0=Ph


     do i=1,N
        IS(i)=0.5D0*((Ph(i-1)-Ph(i-2))**2+&
                     (Ph(i)-Ph(i-1))**2)+&
                     (Ph(i)-2*Ph(i-1)+Ph(i-2))**2
     end do

     IS(N+1)=IS(1)
     IS(N+2)=IS(2)

 !
     do i=1,N
        a0plus(i)=1.D0/(12.D0*(eps+IS(i))**3)
        a1plus(i)=1.D0/(2.D0*(eps+IS(i+1))**3)
        a2plus(i)=1.D0/(4.D0*(eps+IS(i+2))**3)
        a0min(i)=1.D0/(4.D0*(eps+IS(i))**3)
        a1min(i)=1.D0/(2.D0*(eps+IS(i+1))**3)
        a2min(i)=1.D0/(12.D0*(eps+IS(i+2))**3)

     end do
!
     do i=1,N

    Rplus(i)=P(x(i-2),x(i-1),x(i),Ph(i-2),Ph(i-1),Ph(i),xc(i))*a0plus(i)/(a0plus(i)+a1plus(i)+a2plus(i))+&
             P(x(i-1),x(i),x(i+1),Ph(i-1),Ph(i),Ph(i+1),xc(i))*a1plus(i)/(a0plus(i)+a1plus(i)+a2plus(i))+&
             P(x(i),x(i+1),x(i+2),Ph(i),Ph(i+1),Ph(i+2),xc(i))*a2plus(i)/(a0plus(i)+a1plus(i)+a2plus(i))
!
    Rmin(i)= P(x(i-2),x(i-1),x(i),Ph(i-2),Ph(i-1),Ph(i),xc(i-1))*a0min(i)/(a0min(i)+a1min(i)+a2min(i))+&
             P(x(i-1),x(i),x(i+1),Ph(i-1),Ph(i),Ph(i+1),xc(i-1))*a1min(i)/(a0min(i)+a1min(i)+a2min(i))+&
             P(x(i),x(i+1),x(i+2),Ph(i),Ph(i+1),Ph(i+2),xc(i-1))*a2min(i)/(a0min(i)+a1min(i)+a2min(i))
!
     end do
'
```

```
!
      Rplus(0)=Rplus(N)
      Rmin(N+1)=Rmin(1)
!
      do i=1,N
         L0(i)=0.D0
         if (u(i).GT. 0.0) then
            L0(i)=-(1.0/(xc(i)-xc(i-1)))*u(i)*Rplus(i)
         else
            L0(i)=-(1.0/(xc(i)-xc(i-1)))*u(i)*Rmin(i+1)
         end if

         if (u(i-1).GT. 0.0) then
            L0(i)=L0(i)+(1.0/(xc(i)-xc(i-1)))*u(i-1)*Rplus(i-1)
          else
            L0(i)=L0(i)+(1.0/(xc(i)-xc(i-1)))*u(i-1)*Rmin(i)
         end if
      end do
!


      do i=1,N
!        write(*,*) L0(i)      ! should be zero
         L0(i)=L0(i)+alpha*((-Ph(i+2)+16*Ph(i+1)-30*Ph(i)+16*Ph(i-1)-Ph(i-2))/(12*(xc(i)-xc(i-1))**2))

         Ph1(i)=Ph0(i)+dt*L0(i)
!        write(*,*) Ph1(i)     ! should be one

      end do
!
!
!     Update Boundary Conditions (periodic) for Ph1
!
      Ph1(-1) =Ph1(N-1)
      Ph1(0)  =Ph1(N)
      Ph1(N+1)=Ph1(1)
      Ph1(N+2)=Ph1(2)
!
      Ph=Ph1
!
      do i=1,N
         IS(i)=0.5D0*((Ph(i-1)-Ph(i-2))**2+&
                      (Ph(i)-Ph(i-1))**2)+&
                      (Ph(i)-2*Ph(i-1)+Ph(i-2))**2
      end do
      IS(N+1)=IS(1)
      IS(N+2)=IS(2)


      do i=1,N
         a0plus(i)=1.D0/(12.D0*(eps+IS(i))**3)
         a1plus(i)=1.D0/(2.D0*(eps+IS(i+1))**3)
         a2plus(i)=1.D0/(4.D0*(eps+IS(i+2))**3)
         a0min(i)=1.D0/(4.D0*(eps+IS(i))**3)
         a1min(i)=1.D0/(2.D0*(eps+IS(i+1))**3)
         a2min(i)=1.D0/(12.D0*(eps+IS(i+2))**3)

      end do
 !
```

```
!
    do i=1,N

    Rplus(i)=P(x(i-2),x(i-1),x(i),Ph(i-2),Ph(i-1),Ph(i),xc(i))*a0plus(i)/(a0plus(i)+a1plus(i)+a2plus(i))+&
             P(x(i-1),x(i),x(i+1),Ph(i-1),Ph(i),Ph(i+1),xc(i))*a1plus(i)/(a0plus(i)+a1plus(i)+a2plus(i))+&
             P(x(i),x(i+1),x(i+2),Ph(i),Ph(i+1),Ph(i+2),xc(i))*a2plus(i)/(a0plus(i)+a1plus(i)+a2plus(i))
  !
    Rmin(i)= P(x(i-2),x(i-1),x(i),Ph(i-2),Ph(i-1),Ph(i),xc(i-1))*a0min(i)/(a0min(i)+a1min(i)+a2min(i))+&
             P(x(i-1),x(i),x(i+1),Ph(i-1),Ph(i),Ph(i+1),xc(i-1))*a1min(i)/(a0min(i)+a1min(i)+a2min(i))+&
             P(x(i),x(i+1),x(i+2),Ph(i),Ph(i+1),Ph(i+2),xc(i-1))*a2min(i)/(a0min(i)+a1min(i)+a2min(i))

    end do
!
     Rplus(0)=Rplus(N)
     Rmin(N+1)=Rmin(1)
!
    do i=1,N
    L1(i)=0.D0
      if (u(i).GT. 0.0D0) then
         L1(i)=-(1.0D0/(xc(i)-xc(i-1)))*u(i)*Rplus(i)
      else
         L1(i)=-(1.0D0/(xc(i)-xc(i-1)))*u(i)*Rmin(i+1)
      end if

      if (u(i-1).GT. 0.0D0) then
         L1(i)=L1(i)+(1.0D0/(xc(i)-xc(i-1)))*u(i-1)*Rplus(i-1)
       else
         L1(i)=L1(i)+(1.0D0/(xc(i)-xc(i-1)))*u(i-1)*Rmin(i)

      end if
    end do

        do i=1,N
!
           L1(i)=L1(i)+alpha*((-Ph(i+2)+16*Ph(i+1)-30*Ph(i)+16*Ph(i-1)-Ph(i-2))/(12*(xc(i)-xc(i-1))**2))

           Ph2(i)=0.75D0*Ph0(i)+0.25D0*Ph1(i)+0.25D0*dt*L1(i)
!          write(*,*) Ph2(i)

       end do
!
!
!
!
!    Update Boundary Conditions (periodic) for Ph2
!
     Ph2(-1) =Ph2(N-1)
     Ph2(0)  =Ph2(N)
     Ph2(N+1)=Ph2(1)
     Ph2(N+2)=Ph2(2)

     Ph=Ph2
!
     do i=1,N
        IS(i)=0.5D0*((Ph(i-1)-Ph(i-2))**2+&
                     (Ph(i)-Ph(i-1))**2)+&
                     (Ph(i)-2*Ph(i-1)+Ph(i-2))**2
     end do
     IS(N+1)=IS(1)
     IS(N+2)=IS(2)
```

```
     do i=1,N
       a0plus(i)=1.D0/(12.D0*(eps+IS(i))**3)
       a1plus(i)=1.D0/(2.D0*(eps+IS(i+1))**3)
       a2plus(i)=1.D0/(4.D0*(eps+IS(i+2))**3)
       a0min(i)=1.D0/(4.D0*(eps+IS(i))**3)
       a1min(i)=1.D0/(2.D0*(eps+IS(i+1))**3)
       a2min(i)=1.D0/(12.D0*(eps+IS(i+2))**3)

   end do
!
    do i=1,N
    Rplus(i)=P(x(i-2),x(i-1),x(i),Ph(i-2),Ph(i-1),Ph(i),xc(i))*a0plus(i)/(a0plus(i)+a1plus(i)+a2plus(i))+&
             P(x(i-1),x(i),x(i+1),Ph(i-1),Ph(i),Ph(i+1),xc(i))*a1plus(i)/(a0plus(i)+a1plus(i)+a2plus(i))+&
             P(x(i),x(i+1),x(i+2),Ph(i),Ph(i+1),Ph(i+2),xc(i))*a2plus(i)/(a0plus(i)+a1plus(i)+a2plus(i))
 !
    Rmin(i)= P(x(i-2),x(i-1),x(i),Ph(i-2),Ph(i-1),Ph(i),xc(i-1))*a0min(i)/(a0min(i)+a1min(i)+a2min(i))+&
             P(x(i-1),x(i),x(i+1),Ph(i-1),Ph(i),Ph(i+1),xc(i-1))*a1min(i)/(a0min(i)+a1min(i)+a2min(i))+&
             P(x(i),x(i+1),x(i+2),Ph(i),Ph(i+1),Ph(i+2),xc(i-1))*a2min(i)/(a0min(i)+a1min(i)+a2min(i))

    end do
!
    Rplus(0)=Rplus(N)
    Rmin(N+1)=Rmin(1)

    do i=1,N
    L2(i)=0.D0
      if (u(i).GT. 0.0D0) then
         L2(i)=-(1.D0/(xc(i)-xc(i-1)))*u(i)*Rplus(i)
      else
         L2(i)=-(1.D0/(xc(i)-xc(i-1)))*u(i)*Rmin(i+1)
      end if

      if (u(i-1).GT. 0.0D0) then
         L2(i)=L2(i)+(1.D0/(xc(i)-xc(i-1)))*u(i-1)*Rplus(i-1)
       else
         L2(i)=L2(i)+(1.D0/(xc(i)-xc(i-1)))*u(i-1)*Rmin(i)

      end if
    end do

    do i=1,N
       L2(i)=L2(i)+alpha*((-Ph(i+2)+16*Ph(i+1)-30*Ph(i)+16*Ph(i-1)-Ph(i-2))/(12*(xc(i)-xc(i-1))**2))
!
       Ph(i)=(1.D0/3.D0)*Ph0(i)+(2.D0/3.D0)*Ph2(i)+(2.D0/3.D0)*dt*L2(i)
!
    end do

  end do                ! end time integration loop
```

```
  do i=-1,N+2
    Ph0(i)=0.5D0*(1.D0+SIN(2*pival*x(i)))
  end do
!
!
!
  open(unit=12,file='Test.dat')
  do i=1,N
     write (12,'(4E16.8)') x(i),Ph(i),Ph0(i),ABS(Ph(i)-Ph0(i))
  end do
  close(12)
  close(13)

   open(unit=14,file='Testtec.dat')
  do i=1,N
     write (14,*) x(i),Ph(i),Ph0(i)
  end do
  close(14)


 !
end program surfactant

!
!
!Pi-1(xi+0.5)

real*8 function P(xm1,x0,xp1,Phm1,Ph0,Php1,x)
!
    real*8 xm1,x0,xp1,Phm1,Ph0,Php1,x
!
!
    P = (x-x0) *(x-xp1)*Phm1/((xm1-x0)*(xm1-xp1))+&
        (x-xm1)*(x-xp1)*Ph0/((x0-xm1)*(x0-xp1))+&
        (x-xm1)*(x-x0)*Php1/((xp1-xm1)*(xp1-x0))-&
        ((x0-xm1)*Php1-(xp1-xm1)*Ph0+(xp1-x0)*Phm1)/(12.D0*(xp1-xm1))
!
    return
end function
```

Fig. 7.5. Fortran code of WENO5 (W5) scheme for one dimensional simulation

```
!  PROGRAM: Surfactant WENO_Z| 1D
!*****************************************************************************************
    program surfactant

    implicit none

    integer::N
    real*8 eps
    parameter(N=270,eps=0.000001D0)
!
    real*8 x(-1:N+2),xc(-1:N+2)      ! xc(i)=0.5*(x(i)+x(i+1))
    real*8 u(-1:N+2)
    real*8 Ph(-1:N+2),Ph0(-1:N+2),Ph1(-1:N+2),Ph2(-1:N+2)
    real*8 L0(0:N),L1(0:N),L2(0:N)
    real*8 IS0,IS1,IS2,d0,d1,d2,tau5
    real*8 a0plus(0:N),a1plus(0:N),a2plus(0:N),a0min(0:N),a1min(0:N),a2min(0:N)
    real*8 Rplus(0:N),Rmin(0:N+1)
    character*1 cc
!
!
    real*8 alpha,dx,dy,ct,dt,pival
    real*8 P
!
!
!
    integer:: i,it,nt
 !  open(unit=13,file='Test4.dat')
!
     write(*,*) eps
     d0=0.1D0
     d1=0.6D0
     d2=0.3D0
!
     pival=4.D0*DATAN(1.D0)
     ct=0.D0
     nt=4000
     dt=1.D0/nt
     dx=1.D0/N
     alpha=0.D0 ! diffusion
 !
     u=1
     u(-1)=u(N-1)
     u(0)=u(N)
     u(N+1)=u(1)
     u(N+2)=u(2)
!
!
     do  i=-1,N+2
        x(i)  = (i-0.5D0)*dx
        xc(i) =  i*dx
     end do
!
    do i=-1,N+2
       Ph(i)=0.5D0*(1.D0+SIN(2*pival*x(i)))
     end do
```

```
!  start time iteration
!
   do it=1,nt         ! time loop

     ct=ct+dt

     Ph(-1)=Ph(N-1)
     Ph(0)=Ph(N)
     Ph(N+1)=Ph(1)
     Ph(N+2)=Ph(2)
     Ph0=Ph


     do i=1,N
        IS0 = (13D0/12D0)*(Ph(i-2)-2*Ph(i-1)+Ph(i))**2+&
                    0.25D0*(Ph(i-2)-4*Ph(i-1)+3*Ph(i))**2
        IS1 = (13D0/12D0)*(Ph(i-1)-2*Ph(i)+Ph(i+1))**2+&
                    0.25D0*(Ph(i-1)-Ph(i+1))**2
        IS2 = (13D0/12D0)*(Ph(i)-2*Ph(i+1)+Ph(i+2))**2+&
                    0.25D0*(3*Ph(i)-4*Ph(i+1)+Ph(i+2))**2
!
        tau5 = ABS(IS0-IS2)

!
        a0plus(i)=d0*(1+tau5/(IS0+eps))
        a1plus(i)=d1*(1+tau5/(IS1+eps))
        a2plus(i)=d2*(1+tau5/(IS2+eps))
        a0min(i)=d2*(1+tau5/(IS0+eps))
        a1min(i)=d1*(1+tau5/(IS1+eps))
        a2min(i)=d0*(1+tau5/(IS2+eps))

     end do
!
     do i=1,N

    Rplus(i)=P(x(i-2),x(i-1),x(i),Ph(i-2),Ph(i-1),Ph(i),xc(i))*a0plus(i)/(a0plus(i)+a1plus(i)+a2plus(i))+&
             P(x(i-1),x(i),x(i+1),Ph(i-1),Ph(i),Ph(i+1),xc(i))*a1plus(i)/(a0plus(i)+a1plus(i)+a2plus(i))+&
             P(x(i),x(i+1),x(i+2),Ph(i),Ph(i+1),Ph(i+2),xc(i))*a2plus(i)/(a0plus(i)+a1plus(i)+a2plus(i))
  !
    Rmin(i)= P(x(i-2),x(i-1),x(i),Ph(i-2),Ph(i-1),Ph(i),xc(i-1))*a0min(i)/(a0min(i)+a1min(i)+a2min(i))+&
             P(x(i-1),x(i),x(i+1),Ph(i-1),Ph(i),Ph(i+1),xc(i-1))*a1min(i)/(a0min(i)+a1min(i)+a2min(i))+&
             P(x(i),x(i+1),x(i+2),Ph(i),Ph(i+1),Ph(i+2),xc(i-1))*a2min(i)/(a0min(i)+a1min(i)+a2min(i))
 !
     end do

!
     Rplus(0)=Rplus(N)
     Rmin(N+1)=Rmin(1)
   !
```

```
!
      do i=1,N
         L0(i)=0.D0
         if (u(i).GT. 0.0) then
            L0(i)=-(1.0/(xc(i)-xc(i-1)))*u(i)*Rplus(i)
         else
            L0(i)=-(1.0/(xc(i)-xc(i-1)))*u(i)*Rmin(i+1)
         end if

         if (u(i-1).GT. 0.0) then
            L0(i)=L0(i)+(1.0/(xc(i)-xc(i-1)))*u(i-1)*Rplus(i-1)
          else
            L0(i)=L0(i)+(1.0/(xc(i)-xc(i-1)))*u(i-1)*Rmin(i)
         end if
      end do
!

      do i=1,N
!        write(*,*) L0(i)  ! should be zero
         L0(i)=L0(i)+alpha*((-Ph(i+2)+16*Ph(i+1)-30*Ph(i)+16*Ph(i-1)-Ph(i-2))/(12*(xc(i)-xc(i-1))**2))

         Ph1(i)=Ph0(i)+dt*L0(i)
!        write(*,*) Ph1(i)  ! should be one

      end do
!
!     Update Boundary Conditions (periodic) for Ph1
!
      Ph1(-1) =Ph1(N-1)
      Ph1(0)  =Ph1(N)
      Ph1(N+1)=Ph1(1)
      Ph1(N+2)=Ph1(2)
!
      Ph=Ph1
!
      do i=1,N
         IS0 = (13D0/12D0)*(Ph(i-2)-2*Ph(i-1)+Ph(i))**2+&
                    0.25D0*(Ph(i-2)-4*Ph(i-1)+3*Ph(i))**2
         IS1 = (13D0/12D0)*(Ph(i-1)-2*Ph(i)+Ph(i+1))**2+&
                    0.25D0*(Ph(i-1)-Ph(i+1))**2
         IS2 = (13D0/12D0)*(Ph(i)-2*Ph(i+1)+Ph(i+2))**2+&
                    0.25D0*(3*Ph(i)-4*Ph(i+1)+Ph(i+2))**2
!
         tau5 = ABS(IS0-IS2)

!
         a0plus(i)=d0*(1+tau5/(IS0+eps))
         a1plus(i)=d1*(1+tau5/(IS1+eps))
         a2plus(i)=d2*(1+tau5/(IS2+eps))
         a0min(i)=d2*(1+tau5/(IS0+eps))
         a1min(i)=d1*(1+tau5/(IS1+eps))
         a2min(i)=d0*(1+tau5/(IS2+eps))

      end do
```

```
!
   do i=1,N

   Rplus(i)=P(x(i-2),x(i-1),x(i),Ph(i-2),Ph(i-1),Ph(i),xc(i))*a0plus(i)/(a0plus(i)+a1plus(i)+a2plus(i))+&
            P(x(i-1),x(i),x(i+1),Ph(i-1),Ph(i),Ph(i+1),xc(i))*a1plus(i)/(a0plus(i)+a1plus(i)+a2plus(i))+&
            P(x(i),x(i+1),x(i+2),Ph(i),Ph(i+1),Ph(i+2),xc(i))*a2plus(i)/(a0plus(i)+a1plus(i)+a2plus(i))
 !
   Rmin(i)= P(x(i-2),x(i-1),x(i),Ph(i-2),Ph(i-1),Ph(i),xc(i-1))*a0min(i)/(a0min(i)+a1min(i)+a2min(i))+&
            P(x(i-1),x(i),x(i+1),Ph(i-1),Ph(i),Ph(i+1),xc(i-1))*a1min(i)/(a0min(i)+a1min(i)+a2min(i))+&
            P(x(i),x(i+1),x(i+2),Ph(i),Ph(i+1),Ph(i+2),xc(i-1))*a2min(i)/(a0min(i)+a1min(i)+a2min(i))

   end do

    Rplus(0)=Rplus(N)
   Rmin(N+1)=Rmin(1)

   do i=1,N
   L1(i)=0.D0
     if (u(i).GT. 0.0D0) then
        L1(i)=-(1.0D0/(xc(i)-xc(i-1)))*u(i)*Rplus(i)
     else
        L1(i)=-(1.0D0/(xc(i)-xc(i-1)))*u(i)*Rmin(i+1)
     end if

     if (u(i-1).GT. 0.0D0) then
        L1(i)=L1(i)+(1.0D0/(xc(i)-xc(i-1)))*u(i-1)*Rplus(i-1)
      else
        L1(i)=L1(i)+(1.0D0/(xc(i)-xc(i-1)))*u(i-1)*Rmin(i)

     end if
   end do

       do i=1,N
          write(*,*) L1(i)
          L1(i)=L1(i)+alpha*((-Ph(i+2)+16*Ph(i+1)-30*Ph(i)+16*Ph(i-1)-Ph(i-2))/(12*(xc(i)-xc(i-1))**2))

          Ph2(i)=0.75D0*Ph0(i)+0.25D0*Ph1(i)+0.25D0*dt*L1(i)
          write(*,*) Ph2(i)

       end do
!


    Update Boundary Conditions (periodic) for Ph2

    Ph2(-1) =Ph2(N-1)
    Ph2(0)  =Ph2(N)
    Ph2(N+1)=Ph2(1)
    Ph2(N+2)=Ph2(2)

    Ph=Ph2
```

```
     do i=1,N
        IS0 = (13D0/12D0)*(Ph(i-2)-2*Ph(i-1)+Ph(i))**2+&
                    0.25D0*(Ph(i-2)-4*Ph(i-1)+3*Ph(i))**2
        IS1 = (13D0/12D0)*(Ph(i-1)-2*Ph(i)+Ph(i+1))**2+&
                    0.25D0*(Ph(i-1)-Ph(i+1))**2
        IS2 = (13D0/12D0)*(Ph(i)-2*Ph(i+1)+Ph(i+2))**2+&
                    0.25D0*(3*Ph(i)-4*Ph(i+1)+Ph(i+2))**2
!
        tau5 = ABS(IS0-IS2)

!
        a0plus(i)=d0*(1+tau5/(IS0+eps))
        a1plus(i)=d1*(1+tau5/(IS1+eps))
        a2plus(i)=d2*(1+tau5/(IS2+eps))
        a0min(i)=d2*(1+tau5/(IS0+eps))
        a1min(i)=d1*(1+tau5/(IS1+eps))
        a2min(i)=d0*(1+tau5/(IS2+eps))

     end do
 !
    do i=1,N
    Rplus(i)=P(x(i-2),x(i-1),x(i),Ph(i-2),Ph(i-1),Ph(i),xc(i))*a0plus(i)/(a0plus(i)+a1plus(i)+a2plus(i))+&
             P(x(i-1),x(i),x(i+1),Ph(i-1),Ph(i),Ph(i+1),xc(i))*a1plus(i)/(a0plus(i)+a1plus(i)+a2plus(i))+&
             P(x(i),x(i+1),x(i+2),Ph(i),Ph(i+1),Ph(i+2),xc(i))*a2plus(i)/(a0plus(i)+a1plus(i)+a2plus(i))
  !
    Rmin(i)= P(x(i-2),x(i-1),x(i),Ph(i-2),Ph(i-1),Ph(i),xc(i-1))*a0min(i)/(a0min(i)+a1min(i)+a2min(i))+&
             P(x(i-1),x(i),x(i+1),Ph(i-1),Ph(i),Ph(i+1),xc(i-1))*a1min(i)/(a0min(i)+a1min(i)+a2min(i))+&
             P(x(i),x(i+1),x(i+2),Ph(i),Ph(i+1),Ph(i+2),xc(i-1))*a2min(i)/(a0min(i)+a1min(i)+a2min(i))

    end do
    Rplus(0)=Rplus(N)
    Rmin(N+1)=Rmin(1)

    do i=1,N
    L2(i)=0.D0
      if (u(i).GT. 0.0D0) then
         L2(i)=-(1.D0/(xc(i)-xc(i-1)))*u(i)*Rplus(i)
      else
         L2(i)=-(1.D0/(xc(i)-xc(i-1)))*u(i)*Rmin(i+1)
      end if

      if (u(i-1).GT. 0.0D0) then
         L2(i)=L2(i)+(1.D0/(xc(i)-xc(i-1)))*u(i-1)*Rplus(i-1)
       else
         L2(i)=L2(i)+(1.D0/(xc(i)-xc(i-1)))*u(i-1)*Rmin(i)

      end if
    end do

    do i=1,N
       L2(i)=L2(i)+alpha*((-Ph(i+2)+16*Ph(i+1)-30*Ph(i)+16*Ph(i-1)-Ph(i-2))/(12*(xc(i)-xc(i-1))**2))
!
       Ph(i)=(1.D0/3.D0)*Ph0(i)+(2.D0/3.D0)*Ph2(i)+(2.D0/3.D0)*dt*L2(i)
!
    end do

  end do ! end time integration loop
!
```

```
  do i=-1,N+2
     Ph0(i)=0.5D0*(1.D0+SIN(2*pival*x(i)))
  end do
!
!
!
  open(unit=12,file='Test.dat')
  do i=1,N
     write (12,'(4E16.8)') x(i),Ph(i),Ph0(i),ABS(Ph(i)-Ph0(i))
  end do
  close(12)
  close(13)

   open(unit=14,file='Testtec.dat')
  do i=1,N
     write (14,*) x(i),Ph(i),Ph0(i)
  end do
  close(14)
   !
end program surfactant

!
!
!Pi-1(xi+0.5)



real*8 function P(xm1,x0,xp1,Phm1,Ph0,Php1,x)
!
    real*8 xm1,x0,xp1,Phm1,Ph0,Php1,x
!
!
    P = (x-x0) *(x-xp1)*Phm1/((xm1-x0)*(xm1-xp1))+&
        (x-xm1)*(x-xp1)*Ph0/((x0-xm1)*(x0-xp1))+&
        (x-xm1)*(x-x0)*Php1/((xp1-xm1)*(xp1-x0))-&
        ((x0-xm1)*Php1-(xp1-xm1)*Ph0+(xp1-x0)*Phm1)/(12.D0*(xp1-xm1))
!
    return
end function
```

Fig. 7.6. Fortran code of WENO-Z (W5-Z) scheme for one dimensional simulation